Joonas Koponen

ENERGY EFFICIENT HYDROGEN PRODUCTION BY WATER ELECTROLYSIS

ACTA UNIVERSITATIS LAPPEENRANTAENSIS 898

Joonas Koponen

ENERGY EFFICIENT HYDROGEN PRODUCTION BY WATER ELECTROLYSIS

Dissertation for the degree of Doctor of Science (Technology) to be presented with due permission for public examination and criticism in the Auditorium 1316 at Lappeenranta–Lahti University of Technology LUT, Lappeenranta, Finland on the 28th of February, 2020, at noon.

Acta Universitatis
Lappeenrantaensis 898

Supervisors Professor Jero Ahola
LUT School of Energy Systems
Lappeenranta–Lahti University of Technology LUT
Finland

Dr. Antti Kosonen
LUT School of Energy Systems
Lappeenranta–Lahti University of Technology LUT
Finland

Dr. Markku Niemelä
LUT School of Energy Systems
Lappeenranta–Lahti University of Technology LUT
Finland

Reviewers Professor Jens Oluf Jensen
Department of Energy Conversion and Storage
Technical University of Denmark
Denmark

Dr. Marcelo Carmo
Institute for Energy and Climate Research
Electrochemical Process Engineering (IEK-3)
Forschungszentrum Jülich
Germany

Opponent Professor Jens Oluf Jensen
Department of Energy Conversion and Storage
Technical University of Denmark
Denmark

ISBN 978-952-335-490-6
ISBN 978-952-335-491-3 (PDF)
ISSN-L 1456-4491
ISSN 1456-4491

Lappeenranta–Lahti University of Technology LUT
LUT University Press 2020

Abstract

Joonas Koponen
Energy efficient hydrogen production by water electrolysis
Lappeenranta 2020
55 pages
Acta Universitatis Lappeenrantaensis 898
Diss. Lappeenranta–Lahti University of Technology LUT
ISBN 978-952-335-490-6, ISBN 978-952-335-491-3 (PDF), ISSN-L 1456-4491,
ISSN 1456-4491

Hydrogen is the most abundant element in the universe. On Earth, it not only forms water molecules, but also commonly combines with carbon into hydrocarbons that power the current world economy. The use of these natural hydrocarbons for energy depletes the resources of our planet, increases the concentration of carbon dioxide in the atmosphere, and accelerates the acidification of oceans. Globally, the whole energy system must be driven towards a net zero-emission level and beyond through re- and decarbonization and emission-free power generation. Hydrogen would remain a key element in the world economy and electricity could become the main form of energy through this global energy transition.

Water electrolyzers decompose water into hydrogen and oxygen gas with the aid of electric current. Part of the electrical energy supplied to the water electrolysis process is carried as the chemical energy of hydrogen. Water electrolysis is feasible for large-scale production and can transfer emission-free electrical energy to the production of carbon-neutral fuels, raw materials, and chemicals in the hydrogen required to form the constituent synthetic compounds.

AC to DC power conversion, rectification, is required to execute controlled and energy efficient power consumption in electrolyzer systems connected to the main AC electricity grid. Firstly, water electrolyzers are current-controlled DC loads whose optimal and safe operating conditions depend especially on temperature, pressure, and current density. Secondly, the rectification is responsible for the quality of the DC power supplied to the water electrolyzer. Industrial water electrolyzers are characterized by high DC currents and low DC voltages, and therefore, the rectifiers employed have typically been based on thyristors and diodes. The natural commutation of the thyristors introduces notable harmonics to the supplied DC current and DC voltage causing additional heat losses and imposing a constant dynamic operation on the electrolytic cells.

This work focuses on the factors affecting the specific energy consumption of commercial water electrolysis technologies from the viewpoint of power electronics and power supply. The aim is to improve understanding of how the commercial water electrolysis processes can be optimized, integrated into renewable power production systems, and operated in Power-to-X systems. The results highlight the water electrolyzer as the main

energy consumer in Power-to-X systems. The dynamic operation capabilities of a water electrolyzer may have to be artificially limited under fluctuating renewable power to ensure energy efficient operation over time. Operation at elevated pressures, which may be required by other processes in a Power-to-X system, may further limit the safe control range and energy efficiency of a water electrolyzer by decreasing the Faraday efficiency.

The improvement in DC power quality, controllability, and connectivity to the main AC electricity grid can be achieved by using transistor-based rectifiers. The results imply that improving the power quality can have a significant impact on the specific energy consumption and controllability of water electrolyzer systems. With improved power quality, the specific energy consumption of a conventional industrial alkaline water electrolyzer stack may be improved by up to 14%. Understanding of the energy efficient operation and control of water electrolyzers, together with the impact that power quality can have, can notably decrease the end price of hydrogen and carbon-neutral end products required in the global energy transition.

Keywords: water electrolysis, power quality, efficiency, rectifier, Power-to-X, renewable energy systems, hydrogen

Acknowledgments

The research presented in this dissertation was carried out in the LUT School of Energy Systems at Lappeenranta–Lahti University of Technology LUT, Finland, between 2015 and 2019. I want to thank my supervisors Professor Jero Ahola, Dr. Antti Kosonen, and Dr. Markku Niemelä for their assistance in the venture into a new scientific field, electrochemistry. The eagerness of Dr. Vesa Ruuskanen to provide accurate descriptions of what the natural world is like has been influential, and his joint efforts for this research are greatly appreciated. The process to acquire, store, and access measurement data has been notably improved and affected by the work of Mr. Kimmo Huoman. I'm also grateful to Dr. Hanna Niemelä for revising the language of this doctoral dissertation.

I want to thank Walter Ahlström Foundation, Finnish Foundation for Technology Promotion (TES), the Finnish Science Foundation for Technology and Economics (KAUTE), and Research Foundation of LUT for their financial support.

I'm honored to have had Professor Jens Oluf Jensen and Dr. Marcelo Carmo, two distinguished experts in the field, evaluate this doctoral dissertation. A warm thank you to Professor Jensen for agreeing to act as my opponent at the public defence.

Finally, I want to thank my family for their support and understanding on the route that has led me up to this point—through freedom to fail, through curiosity to learn, and, ultimately, to the best of your capabilities to perform. And thank you, Samantha, for not letting me fall.

Joonas Koponen
December 2019
Lappeenranta, Finland

"There's nothing quite as frightening as someone who knows they are right."

—Michael Faraday, allegedly

Contents

List of publications

Publication I
Koponen, J., Ruuskanen, V., Kosonen, A., Niemelä, M., and Ahola, J. (2019). Effect of converter topology on the specific energy consumption of alkaline water electrolyzers. *IEEE Transactions on Power Electronics*, 34(7), pp. 6171–6182.

Publication II
Koponen, J., Ruuskanen, V., Kosonen, A., Niemelä, M., and Ahola, J. (2018). Considering power quality in energy efficiency of alkaline water electrolyzers. In: *20th European Conference on Power Electronics and Applications (EPE '18–ECCE Europe)*, pp. 1–8, Riga, Latvia.

Publication III
Koponen, J., Kosonen, A., Ruuskanen, V., Huoman, K., Niemelä, M., and Ahola, J. (2017). Control and energy efficiency of PEM water electrolyzers in renewable energy systems. *International Journal of Hydrogen Energy*, 42(50), pp. 29648–29660.

Publication IV
Vázquez, F.V., Koponen, J., Ruuskanen, V., Bajamundi, C., Kosonen, A., Simell, P., Ahola, J., Frilund, C., Elfving, J., Reinikainen, M., Heikkinen, N., Kauppinen, J., and Piermartini, P. (2018). Power-to-X technology using renewable electricity and carbon dioxide from ambient air: SOLETAIR proof-of-concept and improved process concept. *Journal of CO_2 Utilization*, 28, pp. 235–246.

Publication V
Ruuskanen, V., Koponen, J., Huoman, K., Kosonen, A., Niemelä, M., and Ahola, J. (2017). PEM water electrolyzer model for a power-hardware-in-loop simulator. *International Journal of Hydrogen Energy*, 42(16), pp. 10775–10784.

The author has been the main author in **Publications I–III** and the corresponding author in **Publication IV**. The simulation work for **Publication I** and the design and construction of the experimental setup for **Publication II** were done in close co-operation with Dr. Vesa Ruuskanen. In **Publication III**, the author was the principal investigator in extending and reanalysing the work initially done in (Koponen et al., 2016) and (Kosonen et al., 2016). The experimental work and the Power-to-X process concept work for **Publication IV** were done in close collaboration with Dr. Fransisco Vidal Vázquez, Dr. Vesa Ruuskanen, Dr. Bajamundi, and Dr. Kosonen. For **Publication IV**, Dr. Fransisco Vidal Vázquez carried out the process simulations for the improved process concept. The literature review for proton exchange membrane water electrolyzer modelling and experiments with the laboratory proton exchange membrane water electrolyzer were conducted by the

author for **Publication V**. The proton exchange membrane water electrolyzer model for **Publication V** was developed in collaboration with Dr. Vesa Ruuskanen, who conducted the practical experimental work with the power-hardware-in-loop electrolysis emulator.

The author has also participated in the following papers closely related to the subject of this dissertation:

- Ruuskanen, V., Koponen, J., Kosonen, A., Hehemann, M., Keller, R., Niemelä, M., and Ahola, J. (2020). Power quality estimation of water electrolyzers based on current and voltage measurements. *Journal of Power Sources*, 450.

- Bajamundi, C., Koponen, J., Ruuskanen, V., Elfving, J., Kosonen, A., Kauppinen, J., and Ahola, J. (2019). Capturing CO_2 from air: technical performance and process control improvement. *Journal of CO_2 Utilization*, 30, pp. 232–239.

- Kosonen, A., Koponen, J., and Peltoniemi, P. (2015). On- and off-grid laboratory test setup for hydrogen production with solar energy in Nordic conditions. In: *17th European Conference on Power Electronics and Applications (EPE '15–ECCE Europe)*, pp. 1–10, Geneva, Switzerland.

- Koponen, J., Kosonen, A., Huoman, K., Ahola, J., Ahonen, T., and Ruuskanen, V. (2016). Specific energy consumption PEM water electrolyzers in atmospheric and pressurised conditions. In: *18th European Conference on Power Electronics and Applications (EPE '16–ECCE Europe)*, pp. 1–10, Karlsruhe, Germany.

- Kosonen, A., Koponen, J., Huoman, K., Ahola, J., Ruuskanen, V., Ahonen, T., and Graf, T. (2016). Optimization strategies of PEM electrolysers as part of solar PV system. In: *18th European Conference on Power Electronics and Applications (EPE '16–ECCE Europe)*, pp. 1–10, Karlsruhe, Germany.

- Ruuskanen, V., Koponen, J., Huoman, K., Kosonen, A., Niemelä, M., Ahola, J., Tiainen, R. (2016). Hardware-in-loop emulator for water electrolysers. In: *42nd Annual Conference of the IEEE Industrial Electronics Society (IECON' 16)*, pp. 4133–4138, Florence, Italy.

- Ruuskanen, V., Koponen, J., Sillanpää, T., Kosonen, A., Niemelä, M., and Ahola, J. (2017). Considering the power quality in the power-hardware-in-loop simulation of water electrolyzers. In: *19th European Conference on Power Electronics and Applications (EPE '17–ECCE Europe)*, pp. 1–9, Warsaw, Poland.

- Ruuskanen, V., Koponen, J., Sillanpää, T., Huoman, K., Kosonen, A., Niemelä, M., and Ahola, J. (2018). Design and implementation of a power-hardware-in-loop simulator for water electrolysis emulation. *International Journal of Renewable Energy*, 119(4), pp. 106–115.

- Kosonen, A., Koponen, J., Ruuskanen, V., Niemelä, M., Ahola, J., Geisbüsch, J., and Kreideweis, P. (2018). Dynamic behavior emulation of alkaline water electrolyzer by power-hardware-in-the-loop. In: *20th European Conference on Power Electronics and Applications (EPE '18–ECCE Europe)*, pp. 1–9, Riga, Latvia.

- Järvinen, L., Ruuskanen, V., Koponen, J., Kosonen, A., and Ahola, J. (2019). Effect of power quality on PEM fuel cells and water electrolyzers: a literature review with Watson Discovery. In: *21st European Conference on Power Electronics and Applications (EPE '19–ECCE Europe)*, pp. 1–8, Genova, Italy.

- Järvinen, L., Ruuskanen, V., Koponen, J., Kosonen, A., Hehemann, M., and Ahola, J. (2019). Implementing a power source to study the effect of power quality on the PEM water electrolyzer stack. In: *21st European Conference on Power Electronics and Applications (EPE '19–ECCE Europe)*, pp. 1–8, Genova, Italy.

Nomenclature

Roman letters

A_{cell}	effective cell area, cm^2
E_{s}	specific energy consumption, $\mathrm{kWh/kg}$
F	Faraday constant, $\mathrm{C/mol}$
G	Gibbs free energy, J
H	enthalpy, J
I_{cell}	cell current, A
I_{stack}	stack current, A
i_{cell}	current density in an electrolytic cell, $\mathrm{A/cm}^2$
$\dot{m}_{\text{H}_2}$	hydrogen gas mass flow rate, $\mathrm{kg/s}$
$\dot{n}_{\text{H}_2}$	hydrogen gas molar flow rate, $\mathrm{mol/s}$
Q	amount of heat, J
S	entropy, $\mathrm{J/K}$
T	temperature, K
t	time, s
U_{act}	activation overvoltage, V
U_{con}	concentration overvoltage, V
U_{ohm}	overvoltage caused by Ohmic losses, V
U_{rev}	open-circuit voltage, V
Z_{imag}	imaginary part of complex impedance, Ω
Z_{real}	real part of complex impedance, Ω
z	number of moles of electrons transferred in a reaction

Greek letters

α	firing angle, $^\circ$
η_{F}	Faraday efficiency
η_{v}	voltage efficiency
ω	angular frequency, $\mathrm{rad/s}$

Acronyms

AC	alternating current
CAPEX	capital expense
CPO	catalytic partial oxidation
DAC	direct air capture
DSTATCOM	distribution static compensator
DC	direct current
EIS	electrochemical impedance spectroscopy
FT	Fischer–Tropsch
HHV	higher heating value
IGBT	insulated gate bipolar transistor
LHV	lower heating value
OPEX	operating expense
PEM	proton exchange membrane
PGM	platinum-group metal
PTFE	polytetrafluoroethylene
PTL	porous transport layer
PV	photovoltaic
RMS	root mean square
RWGS	reverse water-gas shift

1 Introduction

Carbon dioxide emissions of the whole energy sector should be net zero by the year 2050 to limit the global temperature rise to $1.5\,^{\circ}\mathrm{C}$ above pre-industrial levels (Allen et al., 2018). The quicker the global response is to reach the targets set in the Paris agreement, the greater the likelihood is to stay below or return to the $1.5\,^{\circ}\mathrm{C}$ temperature rise. However, the global annual CO_2 emissions grew by 1.6% in 2017 (to $36.2\,\mathrm{Gt}$) and were expected to continue to grow as a result of an increase in oil and natural gas use and growth projected for the global economy (Jackson et al., 2018). Further, a more recent report validated this expected growth: energy-related CO_2 emissions grew by 1.7% (IEA, 2019). The annual global primary energy use was $157\,\mathrm{PWh}$ in 2017, showing an increase of 2.2% compared with 2016 (BP plc, 2018). The share of non-renewables (oil, natural gas, coal) of the world primary energy in 2017 was 85%. In 2018, global energy consumption grew by 2.3% as a result of economic growth and higher heating and cooling needs in certain areas of the world (IEA, 2019). The annual renewables-based electricity generation increase of 7% (increase of $450\,\mathrm{TWh}$) in 2018 was not enough to turn around the trend for CO_2 emissions (IEA, 2019).

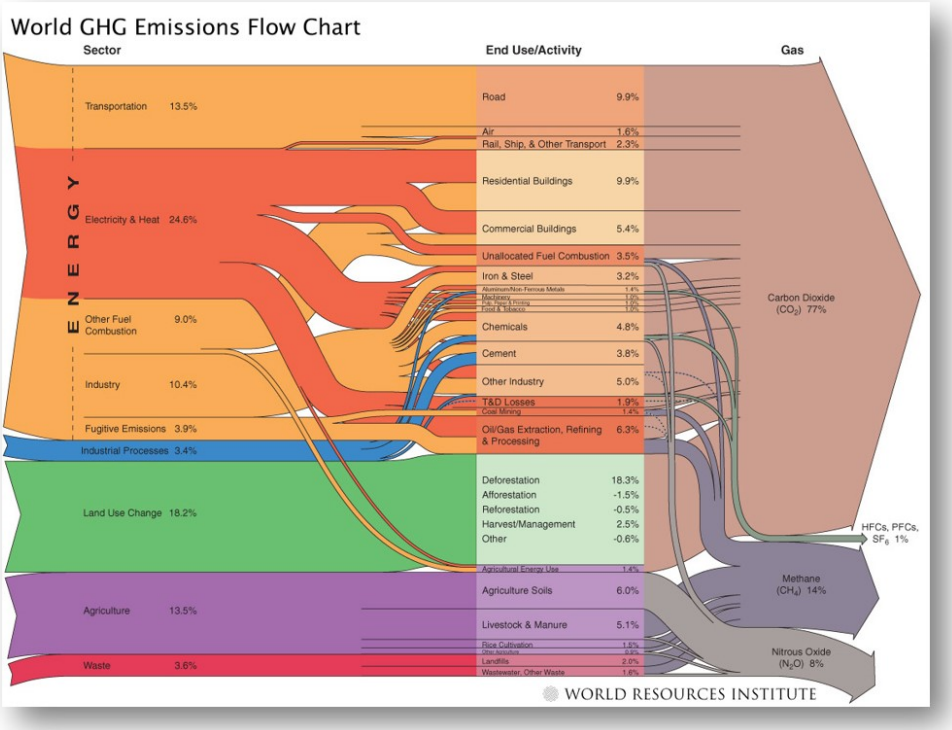

Figure 1.1: Distribution of the world greenhouse gas emissions (Herzog, 2005).

The global greenhouse gas emissions by sector and end use are illustrated in Fig. 1.1. The main CO_2 emitters in the energy sector are the electricity and heat sector (24.6%), the transportation sector (13.5%), and the industrial sector (9.0%). Cement, chemical, and iron & steel are the single largest industrial contributors to the CO_2 emissions, which increase the concentration of CO_2 in Earth's atmosphere and subsequently increase the acidity of Earth's oceans. Thus, transforming (decarbonizing) only the electricity production into renewable power sources is not enough. Therefore, bridges between energy use sectors are needed. Power-to-X concepts can be considered a solution for storing energy from intermittent renewable electrical energy sources and producing carbon-neutral fuels and chemicals from CO_2 emissions. Carbon capture technologies, especially direct air capture (DAC) for collecting and concentrating previously emitted CO_2 from ambient air (Minx et al., 2018), can provide a neutral carbon balance for the production of hydrocarbons. Yet the production of renewable hydrocarbons requires renewable hydrogen.

Hydrogen is a carbon-free fuel and can be used as an energy carrier for CO_2-free power sources, seasonal energy storage to support intermittent power production, chemical production, replacement of coal in steelmaking, and synthesized with recycled CO_2 to form renewable hydrocarbons for both the transportation sector and the chemical industry (Plessmann et al., 2014; Fasihi et al., 2016). For instance the fertilizer industry also needs hydrogen (NH_3). Hydrogen is the most common element in existence, but on Earth, hydrogen mostly exists in compound forms. Hydrogen is a key element in the world economy as it is commonly present on Earth as water and in the main energy resources of the world economy: petroleum, natural gas, and coal. Petroleum is used, for example, in the production of gasoline, kerosene, asphalt, plastics, and pharmaceuticals. Hydrogen will be a key element in the recarbonized world economy where the production of essential compounds is indirectly electrified, in other words, recarbonized.

1.1 Role of water electrolysis

Water electrolyzers split water into hydrogen and oxygen using electricity. In water electrolysis, electrical energy is converted into chemical energy carried by hydrogen and thermal energy. The production of hydrogen is directly proportional to the current passing through the electrodes. As renewable hydrogen production is required and water electrolysis provides a way to convert electricity and water into hydrogen on an industrial scale, electrolytic hydrogen production may play a vital role in the global energy transformation (Fig. 1.2).

Nevertheless, the current fossil-based hydrogen production must first be transformed to be based on non-fossil resources. The current global hydrogen production is around 60×10^6 t, and steam methane reforming is the most popular (48% in Fig.1.3) production method (Gandía et al., 2013). Gandía et al. (2013) report that 96% of global hydrogen is produced from non-renewable sources, and 4% is produced by various electrolysis technologies; only approximately a quarter of the share of electrolysis is specifically from water electrolysis, the majority being due to the chloralkali process. To turn the current global

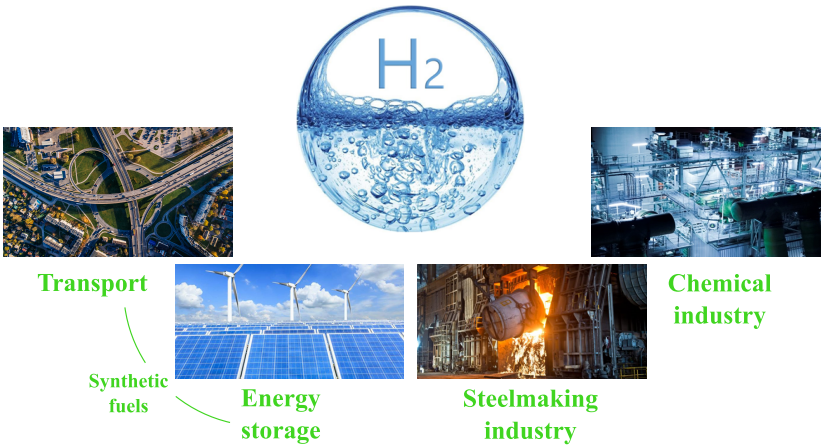

Figure 1.2: Renewable hydrogen is a key element in net zero-emission societies in compound forms with carbon and nitrogen.

hydrogen production to be based on renewables—assuming that for instance biomass- and water-based renewable hydrogen production pathways will not contribute significantly—the global installed water electrolysis capacity would have to be multiplied by 100. To produce $60\,\mathrm{Mt}$ of hydrogen gas by water electrolysis, assuming a state-of-the-art higher heating value efficiency of 80%, $3\,\mathrm{PWh}$ of electrical energy is required, which is 2% of the current global annual primary energy consumption or 13% of the global electricity demand in 2018 (IEA, 2019).

Once all the global hydrogen production is based on renewable sources, the requirement of installed hydrogen production will have to increase dramatically owing to the global energy transformation. Power-to-X technologies, referring to the conversion of electricity into other forms of energy, will increase the need for hydrogen as the transportation and industrial sectors have to be recarbonized. For example, Royal Dutch Shell (2018) calculates that if all the current liquid transport were replaced by synthetic fuels, an additional electricity demand of $83\,\mathrm{PWh}$ ($300\,\mathrm{EJ}$) would be needed. Considering that not all the liquid fuels would be converted into synthetic fuels, an additional annual energy consumption of 10–$41\,\mathrm{PWh}$ per year for Power-to-X technologies has been estimated for 2050 (Frontier Economics, 2018). For optimized Power-to-X systems, where Fischer–Tropsch (FT) synthesis is the second-stage process, the water electrolysis may consume up to 90% of the total energy consumption as discussed in **Publication IV**. Frontier Economics (2018) estimates that the water electrolyzer capacity would represent 75% of the total installed Power-to-X capacity, where the second-stage process is either methanization, FT, or methanol synthesis. Assuming that the future production of synthetic fuels would require an annual electrical energy consumption of $30\,\mathrm{PWh}$ from water electrolyzers, the additional installed electrolytic hydrogen production capacity requirement would be ten times the current total annual hydrogen production ($10\times\ 60\,\mathrm{Mt}$). Meanwhile, if other sectors such as steelmaking were transformed to run on renewable hydrogen instead

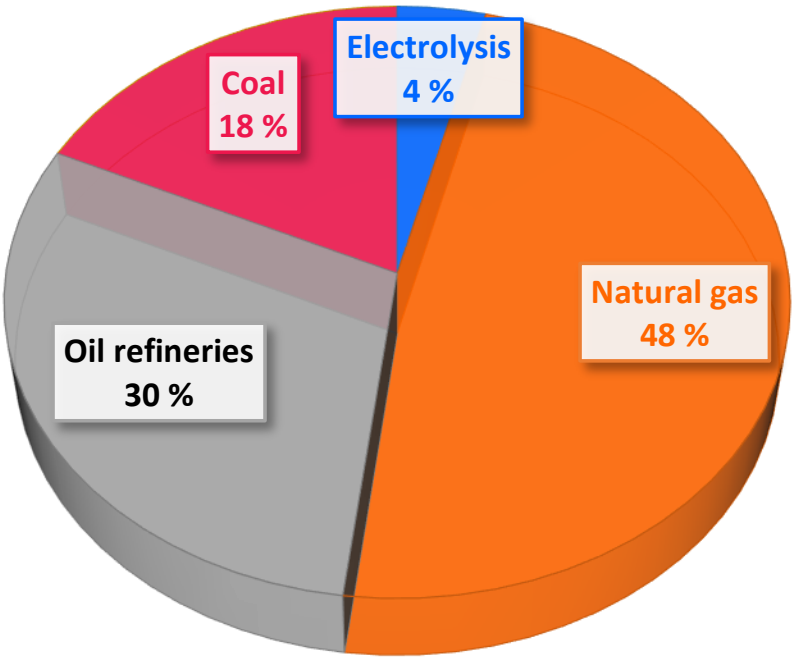

Figure 1.3: Sources of global hydrogen production in 2013 (Gandía et al., 2013). The total annual hydrogen production was $60\,\mathrm{Mt}$ in 2013.

of coal, $52\,\mathrm{Mt}$ more hydrogen would be required annually. Fossil-free steelmaking would then need an additional electical energy consumption of $2.6\,\mathrm{PWh}$ from water electrolyzers. Therefore, the global energy transformation into net zero-emission societies may require thousands of gigawatts of installed water electrolyzer capacity—as envisaged for instance in (Frontier Economics, 2018; Ram et al., 2019). Optimizing the specific energy consumption of the water electrolysis will have a substantial impact on the future world economy.

1.2 State-of-the-art in water electrolysis

There are three main water electrolysis technologies: 1) alkaline, 2) proton exchange membrane (PEM), and 3) solid oxide electrolysis (SOE) (Ursúa et al., 2012; Carmo et al., 2013). PEM water electrolyzers can be further categorized into acidic PEMs and alkaline PEMs, but only the acidic PEM variant is widely commercially available (Schalenbach et al., 2016). Henceforth, the designation 'PEM water electrolysis' refers to the commercial, traditional acidic PEM variant, and the alkaline PEM is referred to as anion exchange membrane (AEM) water electrolysis. Alkaline and PEM water electrolyzers are readily available, commercialized technologies, while SOE is the least developed and not widely commercially available (Schmidt et al., 2017). Alkaline and PEM water electrolyzers typically operate at low temperatures $< 100\,^{\circ}\mathrm{C}$, while SOE is actually steam electrolysis

with operating temperatures typically in the range of 700–1000 °C.

Alkaline water electrolysis is the oldest and most mature technology to produce electrolytic hydrogen. In the alkaline water electrolysis, the anode and cathode electrodes are submerged in a liquid electrolyte, which is typically either an aqueous KOH or NaOH solution (Fig. 1.4). The alkaline water electrolyzer stack structure uses relatively low-cost materials, such as nickel and stainless steel, and the technology has been the standard for industrial-scale electrolytic hydrogen production (Lehner et al., 2014). Zirfon is typically used as a porous separator (diaphragm) material between the anode and cathode compartments, around 500 µm in thickness. Alkaline water electrolyzers typically have a nominal current density $\leq 0.4\,\mathrm{A/cm^2}$ and a system efficiency of 60–80% (based on the higher heating value of hydrogen) in nominal operating conditions. The operating temperature is generally in the range of 70–90 °C. The operating pressure is balanced to levels usually below 30 bar.

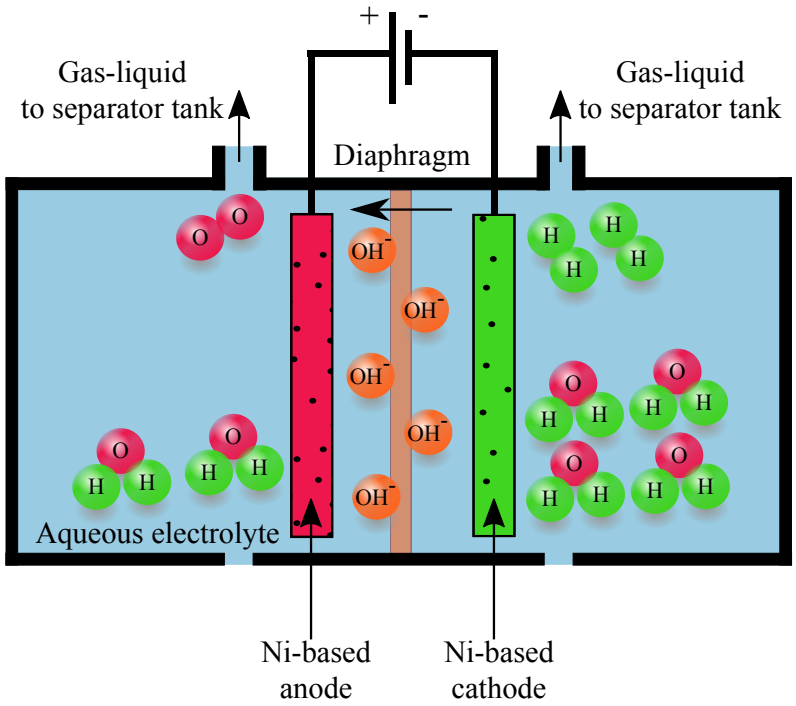

Figure 1.4: Operating principle of an alkaline water electrolysis cell. Water is reduced at the cathode forming hydrogen gas and hydroxide ions OH^-. Hydroxide ions are then decomposed at the anode to form oxygen gas and water.

In the PEM water electrolysis (Fig. 1.5), a thin ($< 250\,\mu m$) proton-conducting membrane is used as a solid polymer electrolyte. Typically, sulphonated fluoropolymers, such as Nafion, are used as the polymer electrolyte. Such a polymer electrolyte is formed by

processing a basic polymer, polyethylene, through perfluorination, creating polytetrafluoroethylene (PTFE), Teflon. Crucially for the operation of PEM water electrolyzers, PTFE is sulphonated by adding a sulphonic acid side chain HSO_3 to the PTFE structure (Larminie and Dicks, 2003). The sulphonic acid attracts water and enables the operating principle of PEM water electrolyzers: Water is supplied to the anode, where water is first decomposed with a sufficient electric potential to oxygen gas. H^+ protons pass through the polymer membrane, and at the cathode combine with electrons to form hydrogen gas.

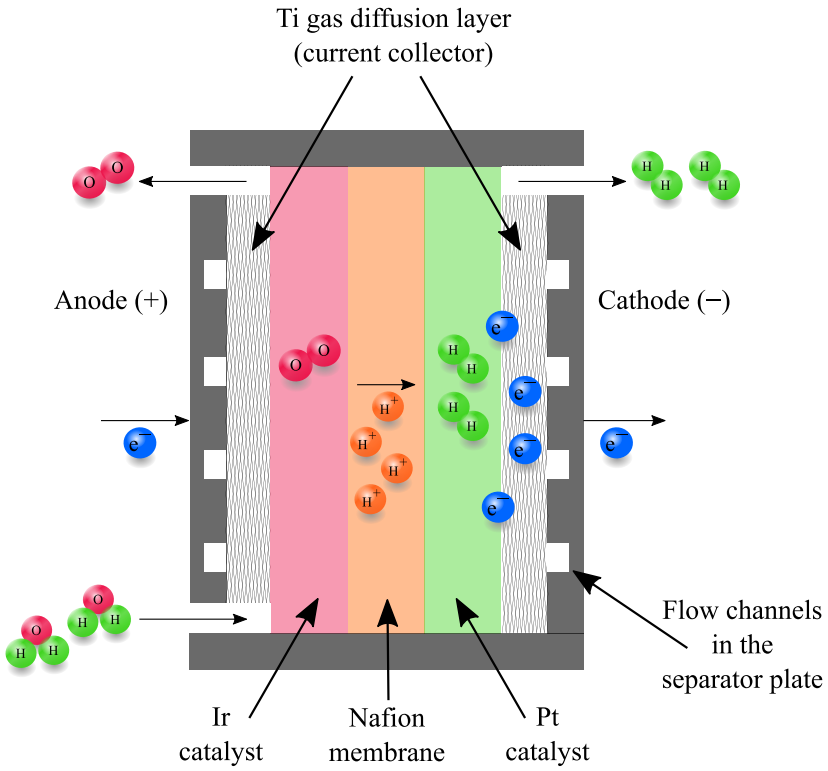

Figure 1.5: Operating principle and cell structure of a PEM water electrolysis cell.

To enable long-term operation and to withstand the corrosive polymer electrolyte, the catalyst materials for PEM water electrolyzers are selected from the platinum-group metals (PGM): typically iridium for the anode catalyst and platinum for the cathode catalyst material (Carmo et al., 2013). Furthermore, iridium may be required as a coating material for porous transport layers (PTL) to increase the cell lifetime. Titanium is usually used in the current collectors and separator plates (Carmo et al., 2013). As alkaline water electrolyzers typically use nickel catalysts and avoid the use of scarce PGM materials, the investment cost (EUR/W) is generally lower for the alkaline water electrolysis technology. In an expert elicitation study by Schmidt et al. (2017), the capital costs for the two established water electrolysis technologies in 2020 in the 10 MW system size have been estimated to be 0.7–1.4 EUR/W for alkaline and 0.8–2.2 EUR/W for PEM. The

two commercial water electrolysis technologies are compared in Table 1.1.

Table 1.1: Comparison of established commercial water electrolysis technologies. Values collected from (Bertuccioli et al., 2014) except (1) from (Lehner et al., 2014) and (2) from (Carmo et al., 2013).

	Alkaline	PEM
Nominal current density	0.2–$0.4\,\mathrm{A/cm^2}$	1.0–$2.0\,\mathrm{A/cm^2}$
Operating temperature	60–$80\,^\circ\mathrm{C}$	50–$80\,^\circ\mathrm{C}$
Cell pressure	$< 30\,\mathrm{bar}$	$< 200\,\mathrm{bar}$ (1)
Min. load of nominal	20–40%	5–10%
H_2 purity	99.5–99.9998%	99.9–99.9999%
Voltage efficiency (HHV) (2)	62–82%	67–82%
Stack E_s (2)	47–$66\,\mathrm{kWh/kg}$	47–$62\,\mathrm{kWh/kg}$
System E_s (2)	50–$78\,\mathrm{kWh/kg}$	50–$83\,\mathrm{kWh/kg}$
Stack lifetime	$60\,000$–$90\,000\,\mathrm{h}$	$20\,000$–$90\,000\,\mathrm{h}$

Alkaline water electrolysis has long been the only technology available on the MW scale (Carmo et al., 2013). Today, however, both alkaline and PEM water electrolyzer cell stacks are commercially available in similar sizes. For example, Hydrogenics (2017) offers $3\,\mathrm{MW}$ PEM stacks, with a physical size of $0.56\,\mathrm{m^3}$, capable of producing $56\,\mathrm{kg/h}$ of hydrogen gas. For reference, a $2.9\,\mathrm{MW}$ alkaline water electrolyzer stack ($54\,\mathrm{kg/h}$ nominal hydrogen gas production rate) provided by Tianjin Mainland Hydrogen Equipment (2019) has a physical size of $28.3\,\mathrm{m^3}$. Power density is the single major difference between the alkaline and PEM water electrolysis technologies; in the aforementioned examples it is $0.10\,\mathrm{MW/m^3}$ against $5.36\,\mathrm{MW/m^3}$, and therefore, the overall material use is lower for PEM water electrolyzers.

1.3 Scientific contributions

The scientific contributions of the publications comprising this doctoral dissertation are summarized as follows:

- Simulated effect of power quality on the specific energy consumption of an MW-scale alkaline water electrolyzer supplied by practical rectifier topologies.
- Simulated effect of the selection of the AC voltage level on the specific energy consumption of industrial alkaline water electrolyzers.
- Analysis of the effect of power converter topology on the controllability of water electrolyzers.
- Initial measurements on the effect of power quality on the specific energy consumption of a small-scale commercial alkaline water electrolyzer.

- Investigation of the impacts of the selection of the hydrogen outlet pressure on the specific energy consumption and control of PEM water electrolyzers.
- Analysis of the limitations on the integration of renewable power production and PEM water electrolysis.
- Demonstration of hydrocarbon production from water, solar energy, and air.
- Conceptual integration of direct air capture of CO_2, electrolytic hydrogen production, and two-step synthesis to optimize the carbon and energy efficiencies in carbon-neutral hydrocarbon production.

The main highlights of the five original papers are discussed in the five following paragraphs.

Publication I presents the simulation results for current and voltage waveforms of a $1\,\mathrm{MW}$ industrial alkaline water electrolyzer with three different practical rectifier topologies: 1) 6-pulse thyristor rectifier, 2) 12-pulse thyristor rectifier, and 3) diode rectifier followed by a voltage-reducing transistor-based circuit. The resulting specific energy consumptions of the electrolyzer stack are compared with a case with an ideal DC power supply as a function of load current. The simulation results of the effect of power quality on the specific energy consumption of water electrolyzers are summarized in Fig. 1.6. It was found that the more modern, transistor-based topology can offer up to a 14% lower specific energy consumption of the alkaline water electrolyzer stack than the 6-pulse thyristor rectifier and up to a 9% lower stack specific energy consumption than the 12-pulse thyristor rectifier. Furthermore, the effect of the AC voltage level selection has a more significant impact on the energy efficient operation with thyristor-based topologies than with the transistor-based topology.

Publication II presents the initial experimental specific energy consumption measurement results of a commercial $2.8\,\mathrm{kW}$ alkaline water electrolyzer with two different power supply configurations. The initial measurement results show that an ideal power supply can offer up to a 24% lower stack specific energy consumption compared with the integrated power supply of the studied commercial alkaline electrolyzer. The experimental work also highlights the improvements required for the experimental setup, mainly the temperature and pressure control, in order to accurately and in a reproducible manner quantify the effects of power quality on the specific energy consumption of alkaline water electrolyzers.

Publication III studies the operational limitations of a commercial $4.5\,\mathrm{kW}$ differential pressure PEM water electrolyzer from the viewpoint of renewable power production. The specific energy consumption of the commercial electrolyzer is calculated according to measurements from two different measurement systems at hydrogen outlet pressures ranging from $2\,\mathrm{MPa}$ to $4\,\mathrm{MPa}$. According to the experimental work, the electrical energy consumption of the electrolyzer did not show any notable increase as a function of

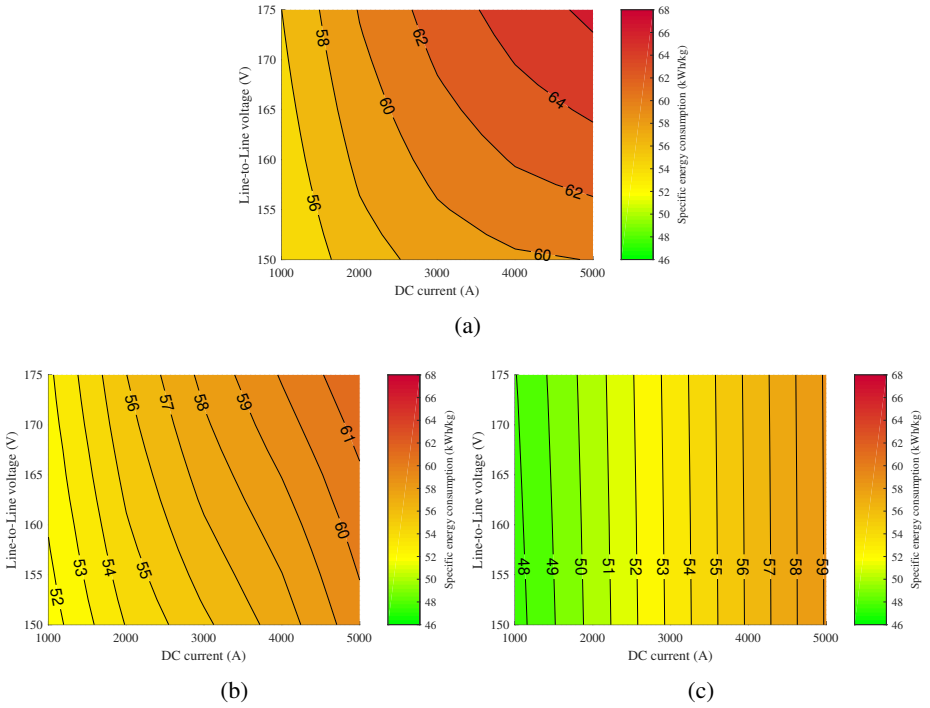

Figure 1.6: Simulated specific energy consumption ($\mathrm{kWh/kg_{H_2}}$) of a $1\,\mathrm{MW}$ alkaline water electrolyzer stack as a function of DC current level and line-to-line voltage. (a) 6-pulse thyristor rectifier. (b) 12-pulse thyristor rectifier. (c) Transistor-based converter.

hydrogen outlet pressure, but the specific energy consumption increased as the Faraday efficiency decreased at higher outlet pressures. The results provide a guideline for the selection of the hydrogen outlet pressure, which is an important decision point especially in Power-to-X systems, system integration, and energy efficient operation. Dynamic operation capabilities of the studied electrolyzer are assessed by virtually connecting the electrolyzer to an actual $5\,\mathrm{kW_p}$ solar photovoltaic (PV) power plant. The power reference provided by this small-scale solar PV power plant then sets the strictest possible dynamic operation requirements for the electrolyzer system, which the commercial electrolyzer could not meet in this case. The commercial water electrolyzer in question limits the DC current slew rates to preserve the lifetime of the electrolytic cells.

Publication IV reports the results of experimental hydrocarbon production from carbon captured from ambient air and hydrogen supplied from a proton exchange water electrolysis. This SOLETAIR Power-to-X process and the transportable pilot plant to demonstrate it comprise DAC of the carbon dioxide unit, a PEM water electrolyzer, and a mobile two-step synthesis unit. The first and second steps of the mobile synthesis unit are reverse water-gas shift (RWGS) and FT. This study analyses the mass and energy balance of the pilot plant. Based on the experimental work and process simulation, an improved Power-to-X process design is proposed. The improved process concept could achieve an energy

efficiency of 47% and a carbon efficiency of 94% by the following means. The two-step synthesis can be improved by gas recirculation and catalytic partial oxidation of light hydrocarbons generated in the second step of the synthesis process. The heat requirement of the direct air capture of CO_2 can be covered by the excess heat from the synthesis and the water electrolysis units. The water requirement of the water electrolyzer can be partly met by the water condensed after the first synthesis step. The water electrolyzer stack is highlighted as the main energy consumer of the whole Power-to-X system.

Publication V presents the design of a power-electronics-based power-hardware-in-loop emulator and studies the implementation of a proton exchange membrane water electrolyzer model, which is based on a commercial $4.5\,\mathrm{kW}$ water electrolyzer, on the emulator. The designed $405\,\mathrm{A}$ electrolysis emulator has a much higher power rating than other emulators presented in the literature and enables the emulation of any water electrolysis technology or DC load without any hardware changes. Ultimately, the power-hardware-in-loop emulator is presented with the task of emulating a PEM water electrolyzer following the power reference from a solar PV power plant.

1.4 Outline of the doctoral dissertation

This doctoral dissertation focuses on studying the factors affecting the specific energy consumption of commercial water electrolysis technologies: alkaline and proton exchange membrane water electrolysis. The identified factors are evaluated from the viewpoint of power electronics, which control the water-splitting reaction, in order to optimize water electrolysis processes and improve the understanding of how water electrolysis processes should be integrated into Power-to-X processes and renewable power production systems.

The motivation for this doctoral dissertation described in Sections 1.1 and 1.2 is succeeded by the following chapters: Chapter 2 introduces the fundamentals of water electrolysis, thermodynamics, and electrochemistry, and describes the definitions to quantify the energy efficiency of water electrolysis. Chapter 3 places the water electrolysis in the framework of Power-to-X processes, focusing on the carbon-neutral hydrocarbon production described in **Publication III**, and discusses the factors identified to affect the design and control of water electrolysis systems. Chapter 4 provides an introduction to the power supply systems used in industrial water electrolyzer systems and discusses the effects that the power supply may have on the electrolyzer. Chapter 5 summarizes the topics discussed in the introductory part of the dissertation and proposes suggestions for future work. Finally, five original papers are provided on the topic of energy efficient hydrogen production by water electrolysis.

2 Fundamentals of water electrolysis

The hydrogen production rate ($\mathrm{mol/s}$) of a single electrolytic cell is linearly proportional to the current

$$\dot{n}_{\mathrm{H_2}} = \eta_{\mathrm{F}} \frac{i_{\mathrm{cell}} A_{\mathrm{cell}}}{zF} = \eta_{\mathrm{F}} \frac{I_{\mathrm{cell}}}{zF}, \tag{2.1}$$

where $\dot{n}_{\mathrm{H_2}}$ is the hydrogen production rate ($\mathrm{mol/s}$), η_{F} is the Faraday efficiency, also known as the current efficiency, i_{cell} is the current density ($\mathrm{A/cm^2}$), A_{cell} is the effective cell area ($\mathrm{cm^2}$), z is the number of moles of electrons transferred in the reaction (for hydrogen, z = 2), F is the Faraday constant ($9.6485 \times 10^4\,\mathrm{C/mol}$), and I_{cell} is the stack current (A).

2.1 Thermodynamics

The energy required for the water decomposition is the enthalpy change of the process, the enthalpy of formation of water, ΔH. The water electrolysis process is endothermic ($\Delta H > 0$). The free energy of the water splitting reaction, called Gibbs free energy change ΔG, must be supplied to the electrodes as electrical energy. The remainder is the thermal energy Q, which is the product of the process temperature T and the entropy change ΔS. These thermodynamic quantities can be written as

$$\Delta H = \Delta G + Q = \Delta G + T\Delta S. \tag{2.2}$$

In constant standard ambient conditions ($298.15\,\mathrm{K}$, one atmosphere pressure), the required electrical work ΔG is equal to $237.2\,\mathrm{kJ/mol}$ (non-spontaneous reaction), and the amount of heat required Q is equal to $48.6\,\mathrm{kJ/mol}$. Thus, the chemical reaction for water electrolysis can be expressed as (Carmo et al., 2013)

$$\begin{aligned} \mathrm{H_2O\,(l)} + 237.2\,\mathrm{kJ_{el.}/mol} + 48.6\,\mathrm{kJ_{heat}/mol} &\longrightarrow \mathrm{H_2(g)} + \frac{1}{2}\,\mathrm{O_2(g)} \\ \Delta H^0 &= 285.8\,\mathrm{kJ/mol}. \end{aligned} \tag{2.3}$$

The lowest voltage for the water splitting to occur is called the reversible voltage U_{rev}, which is directly proportional to the Gibbs free energy change

$$U_{\mathrm{rev}} = \frac{\Delta G}{zF}. \tag{2.4}$$

Without the input of thermal energy, the minimum voltage required becomes the thermoneutral voltage U_{tn}

$$U_{\mathrm{tn}} = \frac{\Delta H}{zF}. \tag{2.5}$$

The reversible voltage and the thermoneutral voltage in standard ambient conditions are $1.23\,\mathrm{V}$ and $1.48\,\mathrm{V}$, respectively. For commercial water electrolyzers, all energy for the

water electrolysis process is provided as electrical energy. Both the reversible voltage and the thermoneutral voltage are thermodynamic state functions dependent on the cell temperature and pressure, albeit the thermoneutral voltage changes only slightly as a function of temperature and pressure (Ulleberg, 2003). The reversible voltage and the thermoneutral voltage are illustrated in Fig. 2.1a as a function of cell temperature. The effect of pressure on reversible voltage is exemplified in Fig. 2.1b.

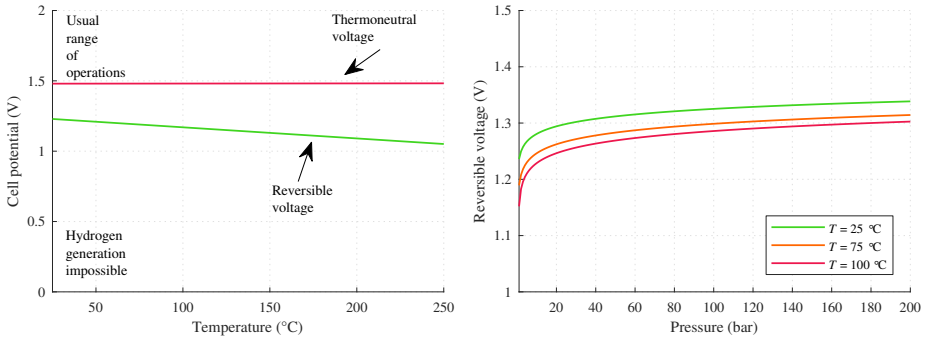

(a) (b)

Figure 2.1: (a) Reversible voltage and thermoneutral voltage in atmospheric pressure water electrolysis as a function of cell temperature. (b) Reversible voltage as a function of pressure for alkaline water electrolysis (30 wt% KOH solution).

An increase in temperature will slightly reduce the overall energy demand ΔH of an ideal liquid water electrolysis process as the demand for electrical energy ΔG is more notably reduced than the demand for thermal energy $T\Delta S$ is increased (Ursúa et al., 2012). Operation at higher temperatures is favourable as heat losses caused by overvoltages can be used to reduce the reversible voltage of water splitting (Ursúa et al., 2012). Thus, the utilization of thermal energy is an essential aspect in energy efficient water electrolysis processes.

The overall energy requirement ΔH will stay practically constant as a function of pressure in an ideal liquid water electrolysis process (Ursúa et al., 2012). However, a change in pressure will increase the demand for electrical energy ΔG; for instance an increase from $0.1\,\mathrm{MPa}$ to $10\,\mathrm{MPa}$ at a cell temperature of $75\,^{\circ}\mathrm{C}$ will increase the reversible voltage by 9%, but the demand for thermal energy $T\Delta S$ is correspondingly reduced.

2.2 Electrochemistry

The electrolytic cell voltage is the sum of the reversible voltage and the additional overvoltages appearing in the cell (Ursúa et al., 2012)

$$U_{\mathrm{cell}} = U_{\mathrm{rev}} + U_{\mathrm{ohm}} + U_{\mathrm{act}} + U_{\mathrm{con}}, \tag{2.6}$$

where U_{cell} is the cell voltage, U_{rev} is the open-circuit, the reversible voltage as a function of temperature and pressure, U_{ohm} is the overvoltage caused by Ohmic losses in the cell elements, U_{act} is the activation overvoltage, and U_{con} is the concentration overvoltage. The current–voltage characteristics of an electrolytic cell can be described by a polarization curve. An example of a polarization curve for an alkaline and a PEM water electrolyzer cell is illustrated in Fig. 2.2.

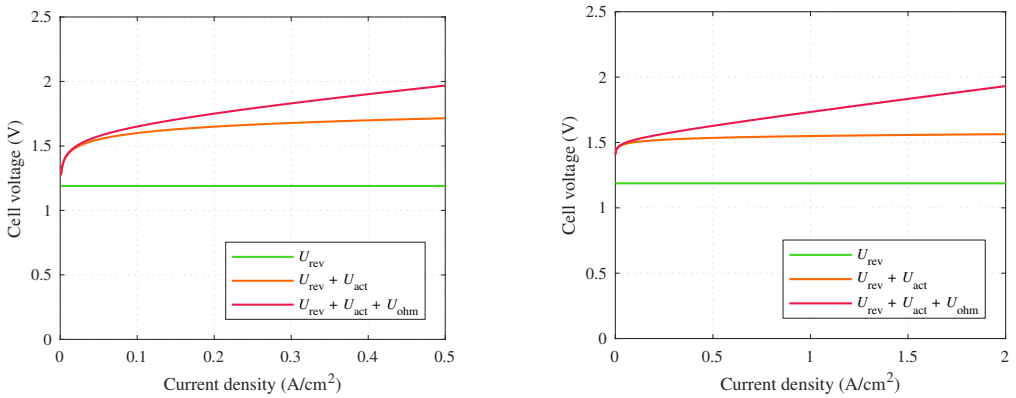

Figure 2.2: Overvoltages in water electrolysis cells. The resulting cell voltage, i.e., the polarization curve, comprises the open-circuit voltage, the activation overvoltage, and the Ohmic overvoltage. (a) Alkaline water electrolyzer cell at an operating temperature of $75\,^{\circ}\text{C}$ and a pressure of $1\,\text{bar}$. (b) PEM water electrolyzer cell at an operating temperature of $75\,^{\circ}\text{C}$ and a pressure of $1\,\text{bar}$.

In the alkaline water electrolysis, the Ohmic losses are mainly affected by the ionic conductivity of the liquid electrolyte, the thickness of the electrolyte layer, and the thickness and conductivity of the electrodes (Milewski et al., 2014). In the PEM water electrolysis, the ionic resistance of the polymeric membrane and the electrical resistance of the separator plates and current collectors are the main contributors to the Ohmic losses (García-Valverde et al., 2012; Carmo et al., 2013). The activation overvoltage is caused by the anode and cathode reaction kinetics (Ursúa and Sanchis, 2012; García-Valverde et al., 2012). The concentration overvoltage is caused by mass transfer limitations at high current densities, where the supply of the reactant (water) is not sufficient to support the reaction rate of the production of hydrogen and oxygen gases at the electrode surfaces (van der Merwe et al., 2014; Milewski et al., 2014). The concentration losses are typically negligible for commercial water electrolyzers—especially for alkaline electrolyzers—because of the relatively low current densities in the cells (Ursúa and Sanchis, 2012; García-Valverde et al., 2012; Milewski et al., 2014). Another non-linear region will appear in the cell polarization curve above the limiting (high) current density, if mass transport losses occur.

An electrolytic cell can be described as an equivalent electric circuit with the following categorization. The cell impedance consists of the Ohmic resistance R_{ohm}, the charge-transfer resistance R_{ct}, and the double-layer capacitance C_{dl}. To take into account the mass transfer losses, the Warburg impedance Z_{wbg} should be included in the equivalent circuit (van der Merwe et al., 2014). The equivalent circuit for an electrolytic cell is illustrated in Fig. 2.3.

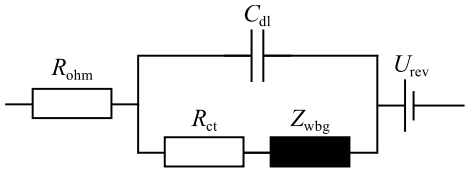

Figure 2.3: Equivalent circuit of an electrolytic cell. The Warburg impedance Z_{wbg} can be excluded from the model if the DC current density is not high.

Categorization of the electrolytic cell losses into Ohmic, activation, and possible mass transfer losses can be achieved by characterization tools such as electrochemical impedance spectroscopy (EIS) (van der Merwe et al., 2014). The EIS characterization produces a Nyquist plot at a selected DC current level with a range of sinusoidal AC current components superimposed. Examples of Nyquist plots are illustrated in Fig. 2.4.

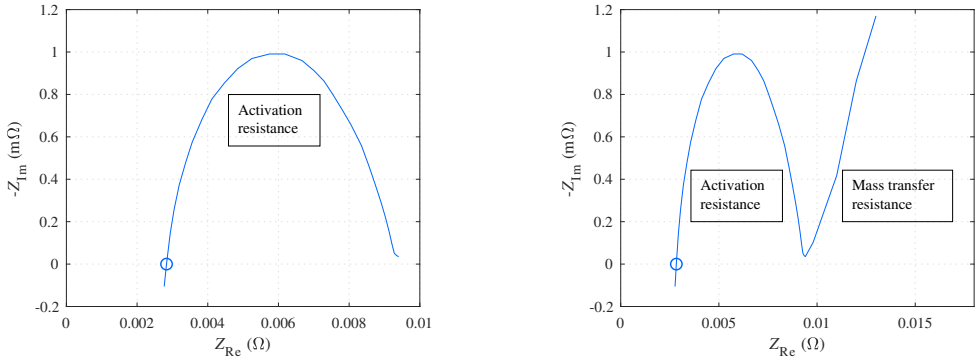

Figure 2.4: Examples of Nyquist plots of an electrolytic cell. ($\circ$) denotes the x-axis intercept, i.e., the value of the cell Ohmic resistance R_{ohm}. (a) Impedance plot without the mass transfer effect at a single DC current level. (b) Impedance plot at a high DC current density where the mass transfer effect is present at a single DC current.

In Fig. 2.4, the Ohmic resistance R_{ohm} is the cell impedance at a high frequency when $Z_{\text{Im}} = 0$. In Fig. 2.4a, the activation resistance corresponds to the area under the half-

circle seen on the capacitive side of Z_{Im}. At high current densities, a start of a second half-circle will appear in the Nyquist plot if mass transfer losses occur (Fig. 2.4b).

2.3 Definitions for the efficiency of water electrolysis

The ideal electrolytic cell operation presented in Fig. 2.1a is further explicated for an example commercial water electrolyzer cell in Fig. 2.5.

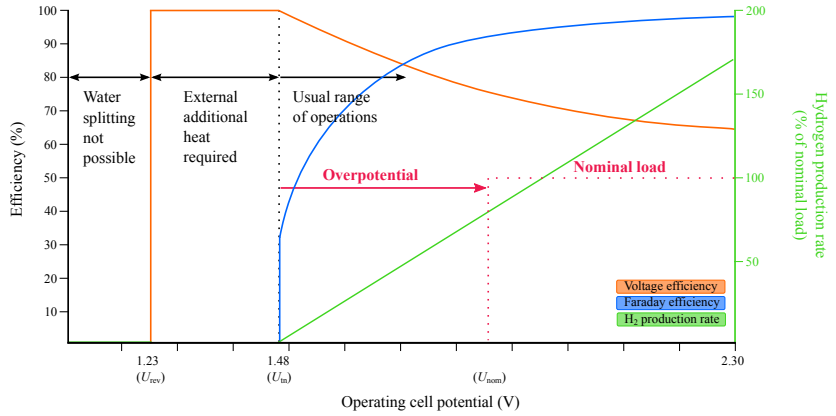

Figure 2.5: Illustrative cell voltage efficiency, Faraday efficiency, and hydrogen production rate as a function of cell potential, where all energy for the electrolysis process is provided as electrical energy.

In standard ambient temperature and pressure (Fig. 2.5), the electrolytic cell starts to decompose water at and above the thermoneutral voltage $U_{\mathrm{tn}} = 1.48\,\mathrm{V}$. As the DC current is increased, the hydrogen production increases linearly to the DC current. However, the effective hydrogen production output from the cell cathode compartment is non-ideal and non-linear; the Faraday efficiency typically approaches unity as current density is increased towards the nominal current density of the electrolyzer, but at low current densities the Faraday efficiency may drop considerably.

The voltage efficiency η_{v} of a water electrolyzer cell can be defined as

$$\eta_{\mathrm{v}} = \frac{U_{\mathrm{tn}}}{U_{\mathrm{cell}}}. \tag{2.7}$$

The voltage efficiency is often used as an indicator of the energy efficiency of water electrolyzers. However, while the voltage efficiency (2.7) represents the electrical losses in the cell or cell stack, it does not consider the possible stray current flow or gas crossovers over the anode and cathode compartments. The Faraday efficiency, or current efficiency, η_{F} is experimentally quantified as the ratio of the ideal hydrogen production rate to the actual hydrogen output from the electrolytic cell (or stack). For the calculation of η_{F}, the ideal hydrogen gas production rate is calculated according to (2.1), where the Faraday efficiency is assumed unity. To include both the voltage and Faraday efficiencies in a single

quantity, the definition-specific energy consumption should be used to assess the energy efficiency of a water electrolysis process

$$E_{\mathrm{s}} = \frac{\int_0^{t_1} I_{\mathrm{stack}} U_{\mathrm{stack}} \mathrm{d}t}{\int_0^{t_1} \dot{m}_{\mathrm{H_2}} \mathrm{d}t} \tag{2.8}$$

where E_{s} is the specific energy consumption, I_{stack} is the stack current, U_{stack} is the stack voltage, $\dot{m}_{\mathrm{H_2}}$ is the hydrogen gas mass flow rate, and t_1 is the inspected time span. Hence, the specific energy consumption describes the amount of energy consumed to produce a mass unit of hydrogen gas. The specific energy consumption is typically expressed either in $(\mathrm{kWh/kg})$ or $(\mathrm{kWh/Nm^3})$, and can be expressed for the electrolyzer stack or for the total electrolytic hydrogen production system. $\mathrm{Nm^3}$ is a volume of one cubic meter at $273.15\,\mathrm{K}$ and one atmosphere pressure—a normal cubic meter.

The energy efficiency of a water electrolysis process can be calculated from

$$\eta_{\mathrm{e}} = \frac{\mathrm{HHV_{H_2}}}{E_{\mathrm{s}}} \tag{2.9}$$

where $\mathrm{HHV_{H_2}}$ is the higher heating value of hydrogen ($39.4\,\mathrm{kWh/kg}$ or $3.54\,\mathrm{kWh/Nm^3}$). Alternatively, the lower heating value of hydrogen (LHV) can be used as a reference ($33.3\,\mathrm{kWh/kg}$ or $3.00\,\mathrm{kWh/Nm^3}$). The difference between the LHV and HHV is the latent heat of condensation. Typically, the HHV value is used as the reference in (2.9) for water electrolysis processes, because liquid water is, in the case of alkaline and PEM water electrolyzers, usually supplied to the process, and the energy required for evaporation of water must be considered (Ursúa et al., 2012; Carmo et al., 2013; Lehner et al., 2014). To enable a comparison between different water electrolyzers, it is crucial that the presented energy efficiency is clearly explained.

2.3.1 Faraday efficiency

As previously mentioned, the Faraday efficiency is the ratio of the ideal hydrogen production rate to the actual hydrogen output from the water electrolyzer. According to (Ulleberg, 2003) and (Decourt et al., 2014), the decrease in Faraday efficiency is caused by stray currents. In other words, not all the electrons contribute to the water splitting reaction, which indicates that either a path of lower resistance exists for the electric current to pass through or side reactions are taking place. It would be beneficial to update the cell and stack level Faraday efficiency to originate from three main sources:

1. Faraday efficiency decrease caused by a gas crossover in the electrolytic cells.
2. Faraday efficiency decrease caused by stray currents.
3. Faraday efficiency decrease caused by possible side reactions taking place.

The gas crossover of hydrogen gas to the anode compartment (oxygen gas outlet), or oxygen gas crossover to the cathode compartment, can be caused by diffusive or convec-

tive mass transfer mechanisms (Schalenbach et al., 2013; Trinke et al., 2018). The convective mass transfer mechanisms can be further categorized into differential pressure, electro-osmotic drag, and electrolyte mixing (not valid for PEM) gas crossover (Trinke et al., 2018). The diffusive gas crossover has been identified to be one order of magnitude smaller in the alkaline water electrolysis compared with the PEM water electrolysis (Schalenbach et al., 2016; Trinke et al., 2018). Trinke et al. (2018) state that for the PEM water electrolysis, diffusion is the single largest contributor to the hydrogen gas crossover, while in the alkaline water electrolysis, the electrolyte mixing—as anodic and cathodic electrolyte cycles are typically mixed together—has the greatest impact (Trinke et al., 2018). Generally, an increase in the operating pressure and a decrease in the current density will degrade the Faraday efficiency of the water electrolyzer as more hydrogen is effectively lost in the oxygen gas outlet. Therefore, the designed operating conditions and control range of the electrolyzer electric current should consider the hydrogen gas crossover effects to preserve the energy efficiency and system safety as discussed in **Publication III**.

3 Control of water electrolysis in Power-to-X systems

The polarization curve, in other words, the current–voltage characteristics (Fig. 2.2), of an electrolytic cell is affected by the cell temperature and pressure. The supplied DC current, which ideally contains no AC components, determines the operating point on the polarization curve. The specific energy consumption of the water electrolysis process is further affected by the Faraday efficiency, which is non-linear with respect to the current density. However, the aforementioned factors consider the water electrolysis as an independent process from the viewpoint of energy efficiency.

3.1 System considerations

Optimization of the operation of a water electrolysis process can be assessed from multiple viewpoints as is illustrated in Fig. 3.1.

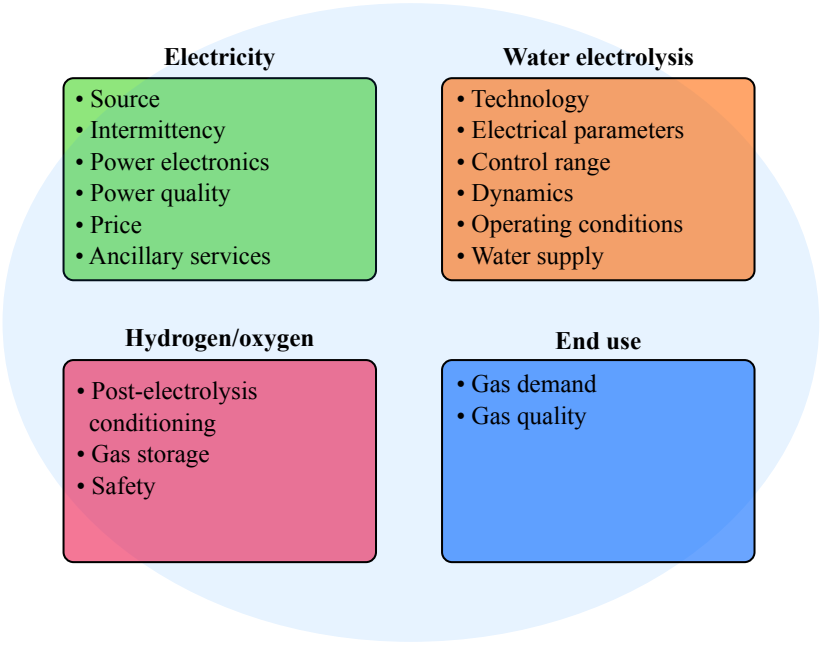

Figure 3.1: Parameters affecting the design and optimization strategy of electrolytic hydrogen production.

The operation of water electrolysis is here considered as part of an integrated Power-to-X system illustrated in Fig. 3.2. The example Power-to-X system, which is discussed in detail in **Publication IV**, consists of three main processes: 1) water electrolysis, 2) DAC of CO_2, and 3) two-step synthesis comprising RWGS and FT synthesis. In this Power-to-X system, the carbon conversion efficiency is further improved by including a catalytic partial oxidation reaction to recirculate unreacted gases from the FT back to the RWGS

step. The intertwined system design and control factors (Fig. 3.1) are further discussed in the following subsections.

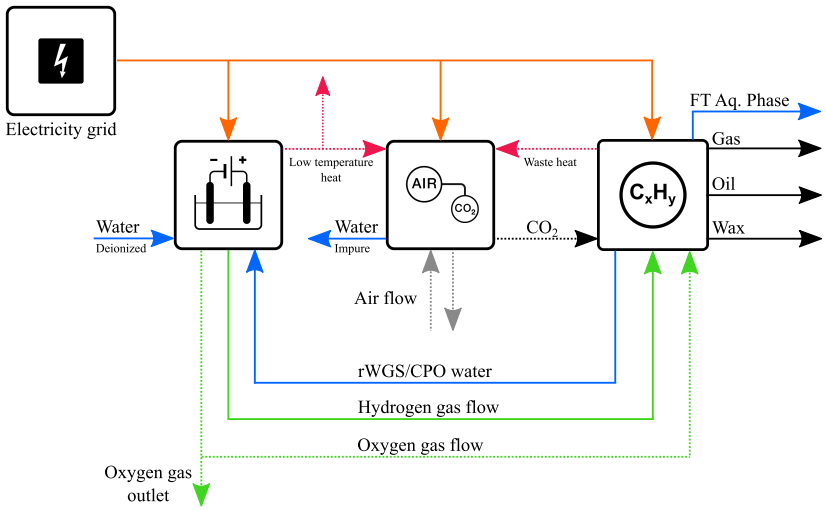

Figure 3.2: Concept of an integrated Power-to-X plant comprising water electrolysis, DAC, and two-step synthesis (RWGS and FT) to produce synthetic hydrocarbons.

3.1.1 Electricity

Source ultimately determines whether the electrolytic product gases from the water electrolysis are fossil-free or not. Increasing the share of fluctuating renewable power generation, wind and solar PV, will impose design requirements on the power supply system. *Intermittency* and availability of electricity may require a certain level of dynamic operation capability of the water electrolysis system and inclusion of an electrical energy storage in the overall system. An electrolyzer manufacturer can present a maximum number of start-stop-cycles for the stack to estimate its lifetime (Ursúa et al., 2016).

Power electronics is essential in controlling the power supply of a water electrolysis system and affecting the energy efficiency of the water electrolysis process. Water electrolyzers require DC power and their operation depends on electric conditioning. Industrial-scale water electrolysis systems are typically connected to the electricity grid, and thus AC-DC conversion, that is, rectification, is required. Overall, the design of power electronic converters for water electrolyzers is characterized by the requirement of relatively high DC currents and relatively low DC voltages. Owing to the high current amplitude requirement in industrial applications, thyristors are commonly used (Rodriguez et al., 2005). However, the use of thyristors (a semiconductor whose conduction is based on the line frequency, 50 Hz or 60 Hz) generates harmonics to the supplied current and voltage causing additional heat losses in the water electrolysis process. Therefore, *power quality* is an important factor for optimizing the specific energy consumption of water elec-

trolyzers as further discussed in Chapter 4 and **Publication I**. Furthermore, additional AC components in the DC power supply to the water electrolyzer may impose a constant dynamic operation on the millisecond time scale, which may have adverse effects on the electrolytic cells. Ursúa et al. (2016) state that cathode degradation in alkaline water electrolysis cells occurs when the cell voltage drops below a certain protective value upon a cell current decrease towards zero. In that case, a poor enough power quality, where the instantaneous DC current value may reach $0\,\mathrm{A}$ as a result of the AC current ripple amplitude being equal or greater than the DC current value, could accelerate the cell degradation rate and decrease the lifetime of the electrolyzer.

Price of electricity has a significant impact on the operational costs of Power-to-X systems. The price of electrolytic hydrogen is dominated by the operational expenditures (OPEX), which are mainly electricity costs. Optimization of the price of electrolytic hydrogen may seek to control the water electrolysis process according to the prevailing and future electricity price. Grid-connected water electrolyzers can also be controlled as part of *ancillary services*; electricity grid stability must be preserved as the supply and demand of electricity must be in balance. Water electrolyzers are controllable DC loads that may contribute to ancillary services such as grid frequency control. Participation in ancillary services may financially benefit the water electrolyzer operator, but require dynamic operation capabilities from the water electrolysis system.

3.1.2 Water electrolysis

Technology selection, viz. alkaline, PEM, AEM, SOE, will have a major impact on the system configuration. The SOE technology could, if it becomes widely commercially available, provide operation in co-electrolysis mode, where H_2O and CO_2 are reduced to synthesis gas, a mixture of H_2 and CO (Ebbesen et al., 2012). But even the selection between the currently commercially widely available alkaline and PEM technologies will set requirements for the required system components; alkaline technology needs a supply of liquid electrolyte, its controlled circulation, and separation from product gases. Furthermore, alkaline electrolyzer stacks are typically limited in their construction because of the liquid electrolyte supply and gas-liquid transport, which has made 200–$300\,\mathrm{V}$ the typical stack voltage for industrial electrolyzers. The PEM technology avoids the construction limitations of the alkaline stacks, but the requirement for high electric currents (to produce more gases) and the exclusively bipolar construction of PEM stacks still sets the stack DC currents relatively high compared with the stack DC voltage. Increasing the stack (assembly) voltage higher, for instance higher than $566\,\mathrm{V}$ ($\sqrt{2} \times \sqrt{3} \times 230\,\mathrm{V}$) and above, may be beneficial to the system energy efficiency and to better interface with the low voltage AC level when using more modern power semiconductors, such as industrial insulated gate bipolar transistor (IGBT) supply units.

Electrical parameters are affected by the selection of the water electrolysis technology. PEM water electrolyzers achieve comparable voltage efficiencies at higher current densities, in other words, they have lower cell impedances. Therefore, smaller variations in the

instantaneous supply voltage cause greater fluctuations in the supplied current for PEM cells. As instantaneous, high variations in current density may have an adverse impact on cell degradation, actions may have to be taken to limit the current slew rate. Cell degradation increases the cell voltage over time, and the increased electrolyzer voltage resulting from degradation should be considered in the system design and operation.

Control range of the electrolyzer is typically expressed in percentage of nominal load. The alkaline technology is associated with greater limitations on the control range (Table 1.1), but the distinction is not clear. Two main causes can be considered to limit the control range of a water electrolyzer: 1) gas crossover rate and 2) power quality. First, the higher the operating pressure, balanced or differential, and the lower the current density are, the greater the gas crossover rate is as dissolved gas concentration is increased at elevated pressures in both the alkaline and PEM water electrolysis. However, the gas crossover mechanisms differ between the alkaline and PEM technologies (Trinke et al., 2018), and therefore, the electrolyzer control range is determined by operating conditions, system/process design (especially to prevent excessive electrolyte mixing in the alkaline water electrolysis), and the MEA design (especially to prevent diffusive gas crossover in PEMs). Second, the power quality can be a limiting factor for the control range. The power supply to industrial electrolyzers is not an ideal DC supply, but typically based on thyristors and diodes, and the AC components in the supplied current may be even greater than the DC component itself. Thus, the instantaneous cell current density is at times far greater than the set DC current density and at times far lower, even close to zero in partial load operation.

Dynamic operation capabilities are often more positively associated with the PEM technology (Babic et al., 2017). According to (Bertuccioli et al., 2014), PEM water electrolyzers are typically capable of ramping up from the minimum load to the full (100%) load at a rate of $10\text{–}100\,\%/\mathrm{s}$, while the alkaline technology is typically limited to $0.13\text{–}10\,\%/\mathrm{s}$. Alkaline water electrolyzer systems are more bulky as liquid electrolyte must be supplied to and from the electrolyzer stack, and the alkaline electrolyzer stacks have more mass to be heated to the designated operating temperature. The selection to operate at elevated pressures sets further limitations to the dynamic operation of both technologies as the stacks must be pressurized at the start-up and the desired pressure maintained in operation. However, if only the electrolytic cell stacks are considered, both alkaline and PEM electrolyzers can respond to changes in the supplied electric current on the ms time scale as electrolytic cells are mostly resistive DC loads. In fact, most industrial electrolyzers are in constant dynamic operating conditions as the power electronics cause rapid fluctuations in input power. Thus, the question should be how much the current slew rate should be limited to preserve cell lifetime, efficiency, safety, and balance in system operation.

Operating conditions, mainly cell temperature and pressure, affect the reversible voltage and impedance of the electrolytic cell, and have an impact on the system efficiency. Increasing the cell temperature is generally beneficial to the cell voltage efficiency, but selected materials will limit the temperature. The cell reversible voltage is also affected

by anode and cathode compartment pressures. The resulting change in voltage efficiency from an increase in pressure is comparable with the ideal isothermal compression of hydrogen gas. However, if the surrounding system, such as post-electrolysis synthesis processes or gaseous storage of hydrogen gas, requires elevated pressures, PEM electrolyzers may opt to operate at a differential pressure and output only hydrogen gas at an elevated pressure, while alkaline electrolyzers are limited to balanced pressure operation. In the PEM water electrolysis, the change in hydrogen outlet pressure from $20\,\mathrm{bar}$ to $40\,\mathrm{bar}$ may result in unchanged electrical energy consumption as discussed in **Publication III**. However, an increase in pressure may compromise the control range of the electrolyzer and its specific energy consumption as the gas crossover rate is increased. Furthermore, operating the water electrolyzer in non-optimal conditions may risk the lifetime of the electrolytic cells.

Water supply and water purification are required to guarantee the normal operation of the water electrolysis process and to preserve the lifetime of the electrolytic cells. In the alkaline water electrolysis, water is consumed from the liquid electrolyte solution, whose concentration must be maintained by an inlet of deionized water. Meanwhile, the PEM water electrolysis is electrolysis of deionized water. The conductivity of the inlet water affects the operation of the electrolytic cell, its energy efficiency and ageing, and the presence of alkaline electrolyte decreases the gas solubility, which has an impact on the gas crossover. In regard to larger Power-to-X systems (Fig. 3.2), the water supply can also be considered from the system integration point. If DAC is included in the system, water is captured from air humidity in addition to CO_2. The water captured from air can then be used, after sufficient purification, as an input to the water electrolysis. Furthermore, if a two-step synthesis, RWGS and FT, is included, most of the hydrogen supplied to the synthesis forms water. The water from the RWGS can be supplied to water electrolysis processes, but the water in the FT products requires more extensive processing, because the FT aqueous phase also includes a range of alcohols. Finally, water recirculation is crucial for the efficient operation of Power-to-X systems.

3.1.3 Hydrogen/oxygen

Post-electrolysis conditioning covers the preparation processes required for the electrolytic product gases. The conditioning may include gas purification; for hydrogen, for example deoxidation and gas drying, and/or pressurization for subsequent processes or *gas storage*. The surrounding system and the need for product gases set the gas conditioning and storage requirements.

In regard to Power-to-X systems (e.g. Fig. 3.2), the hydrocarbon synthesis process may operate at elevated pressures (typically below $50\,\mathrm{bar}$), and the system design may therefore choose to incorporate pressurized electrolysis to match the pressure levels within the system, which, in turn, may limit the partial load operation of the water electrolysis process. Interestingly, a need for oxygen can be found from such Power-to-X systems: the carbon conversion efficiency of a system illustrated in Fig. 3.2 can be improved by recir-

culating unreacted gases back to the first synthesis step, RWGS, and enhancing this stage by catalytic partial oxidation (CPO). Thus, the Power-to-X system energy and carbon efficiency can be improved by system integration.

Safety covers the hydrogen, oxygen, and electrical safety of water electrolysis systems, and the system design and use must follow the applicable directives (ATEX Directive 94/9/EC, ATEX Directive 1992/92/EC, ATEX Directive 2014/34/EU, Seveso III, Pressure Equipment Directive 97/23/EC, Machinery Directive 2006/42/EC, Low Voltage Directive 2006/95/EC, and Electromagnetic Compatibility Directive 2004/108/EC). As to the control of the electrolysis process, the selected current density should consider the prevailing anode and cathode compartment pressures to minimize the gas crossover rates. A limiting cell voltage level can be selected to protect the electrolytic cells against corrosion.

3.1.4 End use

The end use sets the required mass flow rate and dynamics as well as the condition of the electrolytic gases. The varying need for electrolytic gases must always consider all factors affecting the safe, long-lasting, and energy efficient operation of the water electrolyzer discussed in the subsections above.

4 Effect of converter topology on the energy efficiency of water electrolysis

Water electrolyzers require DC power; therefore, their operation depends on electric conditioning. Power electronics play a key role for the water electrolyzers to execute controlled power consumption as well as both energy efficient and safe electrolytic gas production. AC-DC conversion is required for water electrolyzers connected to the main electricity grid. Off-grid system configurations with solar photovoltaic (PV) power generation may opt to interface the water electrolysis and electric power supply using DC-DC conversion (Guilbert et al., 2017). For commercial water electrolyzers, a main AC electricity grid connection is typical (Ursúa et al., 2013).

In high-power applications, in the kiloampere range, rectifiers based on thyristors are by far the most common choice (Rodriguez et al., 2005). Thyristors, first commercialized already in the 1950s (Ueda, 2017), are phase-controlled power electronic switches that switch their conduction based on the electricity grid frequency; a current pulse, at a firing angle α, is fired at the gate of the thyristor to start its conduction in the forward biased mode and the conduction ends when the anode current is about to turn negative (Mohan et al., 1995). As thyristors are only turn-on controlled, they are often called semi-controlled switches. The high efficiency of the thyristor rectifier bridge, high reliability, and capability to withstand high currents have ensured thyristors their dominating role also in water electrolysis applications, where electric currents are relatively high; the hydrogen production rate is directly proportional to the electric charge transferred at the electrodes. Typical MW-scale water electrolyzer stacks have been constructed as low voltage systems with a nominal DC current in the range of thousands of amperes.

4.1 Converter topologies

The most basic topology for a (semi-)controllable DC voltage and DC current supply in industrial water electrolysis applications, the 6-pulse thyristor bridge, is illustrated in Fig. 4.1a. In the 6-pulse topology, six different thyristor pairs (T_1 and T_2, T_1 and T_6, T_5 and T_6, T_5 and T_4, T_3 and T_4, T_3 and T_2) are conducting in turn, each pair for $\frac{\pi}{3}$, following the AC phase voltages $u_{\mathrm{a}}(t)$, $u_{\mathrm{b}}(t)$, and $u_{\mathrm{c}}(t)$. The DC-side voltage $u_{\mathrm{load}}(t)$ and current will have harmonic components multiple of the electricity grid frequency ($300\,\mathrm{Hz}$, $600\,\mathrm{Hz}$, $900\,\mathrm{Hz}$ etc.) owing to the natural commutation of the thyristors.

A 12-pulse thyristor bridge, presented in Fig. 4.1b, is the conventional upgrade over the 6-pulse bridge in high-power, high-current applications. To form the 12-pulse thyristor bridge, two 6-pulse thyristor bridges are separated by a phase angle of 30° by a star-delta configuration in the transformer secondary. The 12-pulse bridge will still introduce harmonic components to the DC voltage and DC current waveforms, but the amplitudes of the harmonics will be lower in amplitude and, corresponding to the doubled number of switches in the topology, higher in frequency; $600\,\mathrm{Hz}$, $1200\,\mathrm{Hz}$, $1800\,\mathrm{Hz}$, and so on.

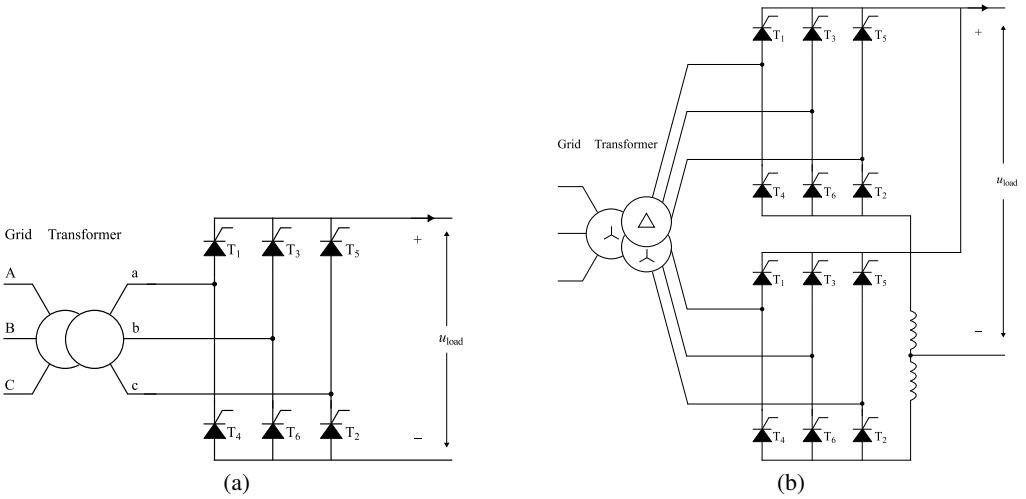

Figure 4.1: Typical thyristor bridge rectifier topologies. (a) A three-phase, 6-pulse thyristor rectifier bridge. (b) A three-phase, 12-pulse thyristor rectifier bridge.

The 6- and 12-pulse thyristor bridge rectifiers represent traditional rectifier solutions for industrial water electrolysis systems. A more modern alternative using fully controlled, forced commutating, power electronic switches is presented in Fig. 4.2.

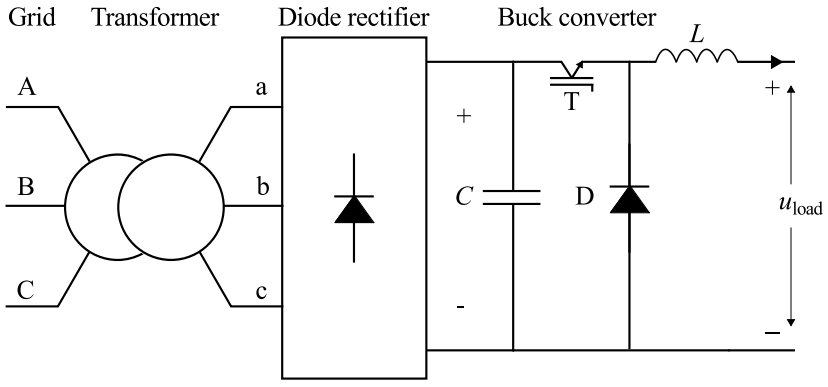

Figure 4.2: Diode bridge followed by a transistor-based buck converter.

In Fig. 4.2, the diode rectifier is typically either a 6- or 12-pulse bridge where individual switches are uncontrollable diodes instead of semi-controllable thyristors. The passive front end is then followed by a buck converter, in other words, a step-down converter, to control the DC voltage waveform at the switching frequency in the kHz range. By using for instance parallel IGBTs, the current can be shared among individual transistors in order not to exceed their current handling capabilities. The size and cost of LC filters are thus more reasonable because of the increased switching frequency.

4.2 Effect on specific energy consumption

Application of transistor-based rectifier topologies may provide a notable reduction in the DC current ripple supplied to a water electrolyzer. To minimize the electrical energy consumption of a water electrolysis process, the current ripple should be minimized. The power dissipated from an electrical conductor is directly proportional to the square of the electric current multiplied by the resistance. Therefore, an instantaneous increase in electric current strongly contributes to the heat loss resulting from the quadratic relationship of current in Ohmic heating. The greater the current ripple, the greater difference between the root mean square (RMS) value and the mean value of the electric current, which is illustrated in Fig. 4.3. As the ideal hydrogen production rate in water electrolysis is directly proportional to the electric charge transferred at the electrodes, that is, the mean value of the electric current, the specific energy consumption increases according to (2.8) when current ripple is increased.

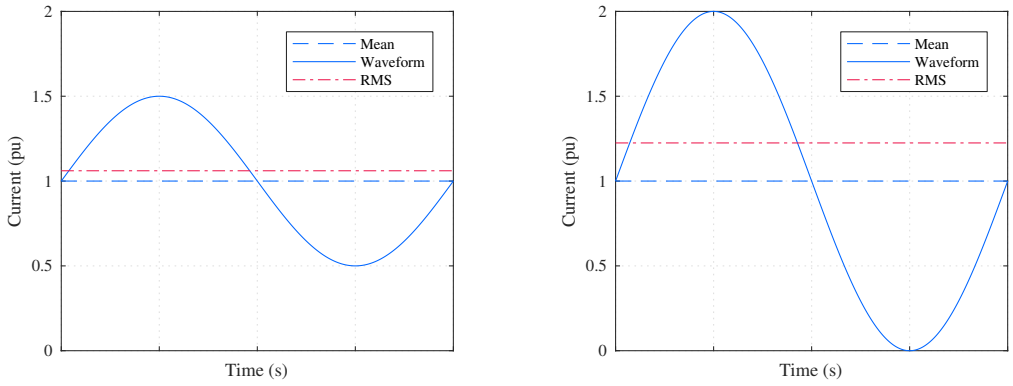

(a) (b)

Figure 4.3: Example of an increase in the RMS value of the electric current as the AC current ripple amplitude is increased. (a) AC current ripple amplitude is 50% of the DC current value, and the RMS value is 6% higher than the mean value of the current. (b) AC current ripple amplitude is 100% of the DC current value, and the RMS value is 22% higher than the mean value of the current.

Unlike the analysis based on the measured DC current waveform, comparing the measured cell or stack voltage RMS value with DC voltage (point-by-point) cannot give direct indication of decreased energy efficiency caused by current ripple. The low current density region in the polarization curve of an electrolytic cell shows a non-linear, inverse hyperbolic sine function behaviour for voltage (Fig. 2.2). Thus, the effect of the non-linear activation overpotential generally prevents inferring of the effect of power quality on the specific energy consumption of water electrolyzers directly from the measured DC voltage waveform. It should be noted that accurate waveform measurement is more practical for DC voltage than for DC current in industrial electrolyzers.

In **Publication I**, the specific energy consumption of a $1\,\mathrm{MW}$ (nominal stack voltage $200\,\mathrm{V}$, nominal stack current $5000\,\mathrm{A}$) alkaline water electrolyzer stack is simulated when supplied by the three practical, industrial rectifier topologies presented in Figs. 4.1, 4.2. The key conclusion in **Publication I** is the stack specific energy consumption difference between the two thyristor topologies and the transistor-based topology: the transistor-based topology could offer up to 14% lower specific energy consumption than with the 6-pulse thyristor bridge, and up to 9% lower specific energy consumption than with the 12-pulse thyristor bridge, depending on the AC voltage level selection (Fig. 1.6). The losses in the power rectifier itself are less significant than the resulting energy efficiency of the water electrolyzer stack: at the nominal load of the $1\,\mathrm{MW}$ alkaline water electrolyzer stack, the specific energy consumption of the stack is roughly $60\,\mathrm{kWh/kg_{H_2}}$, while the losses in the power converter vary between the topologies from $0.8\,\mathrm{kWh/kg_{H_2}}$ (6-pulse thyristor bridge) to $1.5\,\mathrm{kWh/kg_{H_2}}$ (12-pulse thyristor bridge).

The current ripple amplitude has been shown to reach very high values, $> 100\%$ of the DC current value, in **Publication I**. The simulations in **Publication I** simplify the electrolytic cells to have linear current–voltage characteristics (purely resistive with a reversible voltage component), which does not accurately describe the cell behaviour at low current densities. Practical cell polarization curves have a non-linear part at low current densities, in the region characterized by electrode kinetics and activation losses. Furthermore, at very high current densities, especially if the instantaneous current density deviates from the desired DC current density value as a result of high current ripple caused by power electronics, another non-linear part may appear in the cell polarization curve owing to mass transport limitations. Therefore, the possible non-linear part at high current densities could increase the cell voltage and cell losses more than expected.

In the simulations of **Publication I**, the Faraday efficiency is assumed to stay at 100% at all DC current waveforms. However, further investigations should be carried out to study the effective Faraday efficiency under the influence of current ripple at different amplitudes and frequencies. In principle, if the Faraday efficiency is notably decreased at low current densities, the harmonic content in electric current supplied to the electrolyzer could decrease the effective Faraday efficiency from the Faraday efficiency corresponding to the mean value of the electric current supplied, as a result of the non-linear behaviour of Faraday efficiency in regard to current density as illustrated in Fig. 4.4.

In Fig. 4.4, in a point-by-point analytical approach, the harmonic content in the supplied DC current causes the mean Faraday efficiency to drop from the value corresponding to the mean current density, from 96.8% to 95%. In turn, the decreased Faraday efficiency would further increase the specific energy consumption of the water electrolyzer. Furthermore, if the continuous variation of the instantaneous current density caused by current ripple accelerated the ageing of the electrolytic cells, the motivation for minimizing current ripple would be manifold.

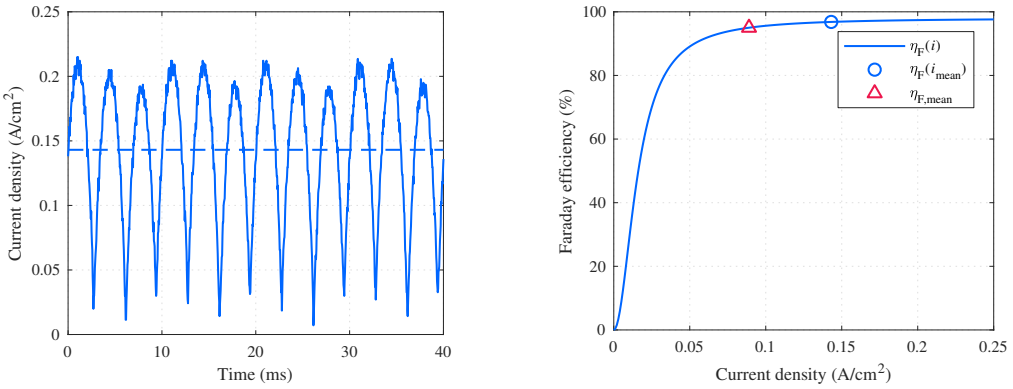

(a) (b)

Figure 4.4: Example of the effect of current ripple on the effective Faraday efficiency of an alkaline water electrolyzer when supplied by a 6-pulse thyristor rectifier and operated at DC current at 40% of nominal. (a) Current density waveform and the mean value of the current density. (b) Faraday efficiency of the alkaline water electrolyzer as a function of current density, the Faraday efficiency corresponding to the mean value of current density (i_{DC}), and the effective Faraday efficiency resulting from the presence of current harmonics ($\eta_{F,mean}$).

4.3 System design considerations

The thyristor bridges produce relatively low-frequency and high-amplitude current ripple to the DC load. The conventional thyristor technology has been popular in high-power, high-current applications because of its cost, reliability, and tradition (Rodriguez et al., 2005). However, as previously discussed, the current harmonics caused by thyristor bridges, which may be costly to filter, impacts the specific energy consumption of the water electrolysis. According to (Thounthong et al., 2009), for fuel cells, the switching frequency in power electronics should be $> 1.25\,\mathrm{kHz}$ and the current ripple $< 5\%$, which the thyristor technology cannot meet. Increasing the switching frequency in the power rectifiers of water electrolysis systems should be considered to minimize the system specific energy consumption by reducing, or enabling the reduction of, electric current ripple. Furthermore, if current and voltage harmonics supplied to electrolytic cells contribute to cell degradation (cell voltage increase over time), minimum specifications for the current ripple amplitude and frequency must be considered in further detail; in other words, how power quality impacts the deterioration of the membrane, the electrodes and the catalysts, and the porous transport layer (PTL). Such specifications for the acceptable current harmonics could then be set by the PEM water electrolysis technology as the lower cell impedance of the PEM cells would inherently also cover the dynamics of alkaline electrolysis cells. However, the possibility to recover from reversible cell degradation using certain current waveforms should be considered as discussed by Rakousky et al. (2016), whose investigations considered load cycles on the scale of minutes rather than the milli-

or microsecond scale relevant to power electronics.

The power quality can affect the material use in water electrolyzer stacks: An electrolyzer system with improved power quality could, in principle, operate at a higher current density, and produce more electrolytic gases, yet maintaining the previous specific energy consumption of the system. In other words, the power density of the electrolyzer could be increased by improving the power quality, and, in turn, the material use could be lowered without increasing the specific energy consumption of the electrolyzer. Thus, both the CAPEX and OPEX of the water electolyzer system are affected by the power quality supplied to the electrolyzer stack.

The thyristor-based rectifiers are further impacted by any cell degradation over time as the specific energy consumption of the water electrolyzer stack is more notably a function of AC voltage level with the typical 6- and 12-pulse topologies than with the transistor-based topology inspected in **Publication I**. For the more established alkaline technology, the cell degradation rate has been reported to be 0.4–$5\,\mu\mathrm{V/h}$ and the stack lifetime $60\,000$–$90\,000\,\mathrm{h}$ (Bertuccioli et al., 2014). For example, a 90-cell bipolar alkaline stack with a beginning-of-life nominal operation stack voltage of $200\,\mathrm{V}$ would undergo a nominal stack voltage increase to $227\,\mathrm{V}$ in $60\,000\,\mathrm{h}$ at a cell voltage degradation rate of $5\,\mu\mathrm{V}$. The power electronics supplying the ageing electrolyzer should be able to optimally control the electrolysis process even after the increased impedance of the electrolyzer stack (assembly).

The rectifier selection in water electrolysis applications should not be the only focus on the DC side of the power conversion. Concerning the main electricity grid side, the thyristor operation consumes reactive power, which may have to be compensated for by using additional equipment such as a distribution static compensator (DSTATCOM) and/or passive filters on the AC side (Solanki et al., 2012). The DSTATCOM is an active bridge followed by a capacitor, and therefore, the DSTATCOM typically has very little active power compensation capacity, but can be used for variable reactive power compensation using the control of the transistors of the active bridge. Reactive power compensation equipment may be excluded from the system if forced-commutating power electronic switches are used in the rectifier itself.

5 Conclusion

Renewable hydrogen is essential to produce carbon-neutral fuels for transportation, raw materials for the chemical and steel industry, and seasonal energy storages. The current fossil-based hydrogen production must be transformed to be based on fossil-free resources. Water electrolyzers split water into hydrogen and oxygen using electricity, and the supplied electrical energy is converted into chemical energy carried by hydrogen. Water electrolysis, which is feasible for large-scale and fossil-free hydrogen production, can play a vital role in restructuring the whole energy system. The estimates for globally installed water electrolyzer capacities range up to terawatts. Power electronics, which are required in the DC power supply to water electrolysis processes, can play a major role in achieving savings in electrical energy consumption and the price of electrolytic hydrogen and oxygen.

5.1 Main results

This doctoral dissertation focuses on factors affecting the energy efficient operation of commercial water electrolyzers. The identified factors are evaluated from the viewpoint of power electronics that control the water-splitting reaction in order to optimize water electrolysis processes and improve the understanding of how water electrolysis processes should be integrated into Power-to-X processes and renewable power production systems.

The main outcome of this work is the notable effect of power quality on the specific energy consumption of water electrolyzers. With the typical power supply configurations used in industrial water electrolyzer systems, the specific energy consumption of the water electrolyzer stack could be decreased even up to 14% with enhanced power quality. The use of more modern power electronic devices could improve the energy efficiency of water electrolyzer stacks by minimizing the Ohmic losses. The controllability of the water electrolyzer may also be compromised by poor power quality if the instantaneous current densities approach $0\,\mathrm{A/cm^2}$. The effect of current ripple on the Faraday efficiency and lifetime of electrolytic cells is a key topic of future work.

Water electrolyzers are the main energy consumers in Power-to-X systems described in **Publication IV**. Therefore, minimizing the electrical energy consumption of the water electrolysis process plays an essential role in making Power-to-X processes more energy efficient. The energy and carbon efficiencies of Power-to-X systems can be further improved by system integration. Synthesis processes may require hydrogen at elevated pressures, and then, the selection of the operating pressures for the water electrolyzer should be considered in relation to the surrounding overall system. Increasing the hydrogen outlet pressure of the water electrolyzer sets limitations for the control range of the electrolyzer as the Faraday efficiency is decreased. If an intermediate hydrogen storage is included in the Power-to-X system, the stack hydrogen outlet pressure should be controlled as close to the storage pressure as possible to maximize the control range and the Faraday efficiency.

5.2 Suggestions for future work

Experimental work must be targeted to more comprehensively verify the effect of power quality on the specific energy consumption of water electrolysis technologies. Development of a test environment to study the effects of current ripple on electrolytic cells, together with accurately quantifying the impacts on both the energy and Faraday efficiency, has been a continuous learning process in the course of this work.

Voltage degradation under dynamic operation conditions has been a suggested research topic (Bertuccioli et al., 2014). Instead of focusing on the electrolytic cell ageing under fluctuating power, typically meaning intermittent renewable power production systems, the time scale should be extended to the subsecond scale to take account of the possible effects that power electronics may have on cell degradation. The effect of power quality on cell degradation should study the ageing of the membrane, the electrodes and the catalyst, and the PTL of the cell structure. Furthermore, the option to use the rectifier system itself to recover from reversible degradation should be further studied. Overall, investigations on the effects of power quality on electrolytic cell degradation and specific energy consumption should provide guidelines for the acceptable power quality supplied to a water electrolyzer.

The use of modern power electronics could also enable the implementation of sophisticated, non-invasive automatic identification algorithms to the rectifier of the water electrolyzer system. The forced commutation and higher switching frequency (or interleaved, effective switching frequency) of transistor-based power electronics have the potential for enabling a reduction in the harmonic content in the DC voltage and DC current supplied to an electrolyzer, in automatic system identification, and reactive power compensation to the main electricity grid. Topologies enabling the reliable use of more modern power electronics in high-power, high-current water electrolysis applications should be further investigated.

Finally, the proposed scale for installed water electrolyzers is colossal—terawatts of installed global capacity—and even if the conventional water electrolyzers did not ultimately account for all of the renewable hydrogen needed for the global energy transformation, the required materials for electrolyzers, the much greater volume in electrolyzer stack production, and recycling of materials should be taken into account. The use of iridium may limit the large-scale commercialization and CAPEX cost decrease of the PEM technology, especially if 100% renewable global energy systems for 2050 are considered: if the estimated $17\,\mathrm{TW}$ (Ram et al., 2019) of installed water electrolyzer capacity were PEM electrolyzers, the required iridium would accumulate to roughly $6800\,\mathrm{t}$ (with an assumed anode catalyst loading of $2\,\mathrm{mg/cm^2}$ and a power density of $5\,\mathrm{W/cm^2}$). Iridium is one of the rarest elements in the earth's crust and its current annual production by separation from ores containing platinum or nickel (Stwertka, 2018) is limited to $3\,\mathrm{t}$ (Minor Metals Trade Association, 2016). The large-scale envisaged requirement for water electrolyzers must consider the limited stack lifetime and the use and recycling of materials as

the reported stack lifetimes have thus far been less than ten years. Similar considerations concern the production and recycling of solar PV and wind power systems of the future recarbonized world economy.

References

Allen, M., et al. (2018). Technical Summary. In: Masson-Delmotte, V., Zhai, P., Pörtner, H.O., Roberts, D., Skea, J., Shukla, P., Pirani, A., Moufouma-Okia, W., Péan, C., Pidcock, R., Connors, S., Matthews, J., Chen, Y., Zhou, X., Gomis, M., Lonnoy, E., Tignor, T.M.M., and Waterfield, T., eds, *Global Warming of 1.5 °C. An IPCC Special Report on the impacts of global warming of 1.5 °C above pre-industrial levels and related global greenhouse gas emission pathways, in the context of strengthening the global response to the threat of climate change, sustainable development, and efforts to eradicate poverty*. In Press.

Babic, U., Suermann, M., Büchi, F.N., Gubler, L., and Schmidt, T.J. (2017). Critical Review — Identifying Critical Gaps for Polymer Electrolyte Water Electrolysis Development. *Journal of The Electrochemical Society*, 164(4), pp. F387–F399. doi: 10.1149/2.1441704jes.

Bertuccioli, L., Chan, A., Hart, D., Lehner, F., Madden, B., and Standen, E. (2014). *Study on development of water electrolysis in the EU*. Final report in fuel cells and hydrogen joint undertaking.

BP plc (2018). *BP statistical review of world energy*. URL `https://www.bp.com/content/dam/bp/business-sites/en/global/corporate/pdfs/energy-economics/statistical-review/bp-stats-review-2018-full-report.pdf`. [Accessed: 23-Aug-2019].

Carmo, M., Fritz, D., Mergel, J., and Stolten, D. (2013). A comprehensive review on PEM water electrolysis. *International Journal of Hydrogen Energy*, 38(12), pp. 4901–4934. doi: 10.1016/j.ijhydene.2013.01.151.

Decourt, B., Lajoie, B., Debarre, R., and Soupa, O. (2014). *The hydrogen-based energy conversion FactBook*. The SBC Energy Institute.

Ebbesen, S.D., Knibbe, R., and Mogensen, M. (2012). Co-Electrolysis of Steam and Carbon Dioxide in Solid Oxide Cells. *Journal of The Electrochemical Society*, 159(8), pp. F482–F489. doi: 10.1149/2.076208jes.

Fasihi, M., Bogdanov, D., and Breyer, C. (2016). Techno-Economic Assessment of Power-to-Liquids (PtL) Fuels Production and Global Trading Based on Hybrid PV-Wind Power Plants. *Energy Procedia*, 99, pp. 243–268. doi: 10.1016/j.egypro.2016.10.115.

Frontier Economics (2018). *International aspects of a Power-to-X roadmap: a report prepared for the World Energy Council Germany*. URL `https://www.frontier-economics.com/media/2646/20181018_frontier_wec_germany_ptxroadmap_full-study-english.pdf`. [Accessed: 23-Aug-2019].

Gandía, L., Arzamendi, G., and Diéguez, P. (2013). Chapter 1 - Renewable hydrogen technologies. In: Gandía, L., Arzamendi, G., and Diéguez, P., eds, *Renewable Hydrogen Technologies*, pp. 1–17. Amsterdam: Elsevier. ISBN 978-0-444-56352-1.

García-Valverde, R., Espinosa, N., and Urbina, A. (2012). Simple PEM water electrolyser model and experimental validation. *International Journal of Hydrogen Energy*, 37(2), pp. 1927–1938. doi: 10.1016/j.ijhydene.2011.09.027.

Guilbert, D., Collura, S.M., and Scipioni, A. (2017). DC/DC converter topologies for electrolyzers: State-of-the-art and remaining key issues. *International Journal of Hydrogen Energy*, 42(38), pp. 23966 – 23985. doi: 10.1016/j.ijhydene.2017.07.174.

Herzog, T. (2005). *World greenhouse gases in 2005*. World Resources Institute. URL `http://www.wri.org/sites/default/files/world\_greenhouse\_gas\_emissions\_2005.pdf`.

Hydrogenics (2017). *Hydrogenics unveils 3 megawatt PEM electrolyzer stack*. URL `https://www.hydrogenics.com/2017/04/25/hydrogenics-unveils-3-megawatt-pem-electrolyzer-stack/`. [Accessed: 23-Aug-2019].

IEA (2019). *Global energy & CO_2 status report: The latest trends in energy and emissions in 2018*. URL `https://webstore.iea.org/global-energy-co2-status-report-2018`. [Accessed: 23-Aug-2019].

Jackson, R.B., Quéré, C.L., Andrew, R.M., Canadell, J.G., Korsbakken, J.I., Liu, Z., Peters, G.P., and Zheng, B. (2018). Global energy growth is outpacing decarbonization. *Environmental Research Letters*, 13(12), p. 120401. doi: 10.1088/1748-9326/aaf303.

Koponen, J., Kosonen, A., Huoman, K., Ahola, J., Ahonen, T., and Ruuskanen, V. (2016). Specific energy consumption of PEM water electrolysers in atmospheric and pressurised conditions. In: *Proc. 18th European Conf. on Power Electron. and Applicat. (EPE '16–ECCE Europe)*. Karlsruhe, Germany.

Kosonen, A., Koponen, J., Huoman, K., Ahola, J., Ruuskanen, V., Ahonen, T., and Graf, T. (2016). Optimization strategies of PEM electrolyser as part of solar PV system. In: *2016 18th European Conference on Power Electronics and Applications, EPE 2016 ECCE Europe*. Karlsruhe, Germany. ISBN 9789075815245.

Larminie, J. and Dicks, A. (2003). *Fuel Cell Systems Explained*. England: John Wiley & Sons Ltd. ISBN 9781118878330.

Lehner, M., Tichler, R., Steinmüller, H., and Koppe, M. (2014). *Power-to-gas: technology and business models*. New York: Springer International Publishing.

van der Merwe, J., Uren, K., van Schoor, G., and Bessarabov, D. (2014). Characterisation tools development for PEM electrolysers. *International Journal of Hydrogen Energy*, 39(26), pp. 14212–14221. doi: 10.1016/j.ijhydene.2014.02.096.

Milewski, J., Guandalini, G., and Campanari, S. (2014). Modeling an alkaline electrolysis cell through reduced-order and loss-estimate approaches. *Journal of Power Sources*, 269, pp. 203–211. doi: 10.1016/j.jpowsour.2014.06.138.

Minor Metals Trade Association (2016). *Ir – Iridium*. URL `https://mmta.co.uk/metals/ir/`. [Accessed: 24-Jun-2019].

Minx, J.C., Lamb, W.F., Callaghan, M.W., Fuss, S., Hilaire, J., Creutzig, F., Amann, T., Beringer, T., de Oliveira Garcia, W., Hartmann, J., Khanna, T., Lenzi, D., Luderer, G., Nemet, G.F., Rogelj, J., Smith, P., Vicente, J.L.V., Wilcox, J., and del Mar Zamora Dominguez, M. (2018). Negative emissions—Part 1: Research landscape and synthesis. *Environmental Research Letters*, 13(6), p. 063001.

Mohan, N., Undeland, T.M., and Robbins, W.P. (1995). *Power electronics: converters, applications, and design*, 2nd edn. John Wiley & Sons, Inc. ISBN 0-471-58408-8.

Plessmann, G., Erdmann, M., Hlusiak, M., and Breyer, C. (2014). Global energy storage demand for a 100% renewable electricity supply. *Energy Procedia*, 46, pp. 22–31. doi: 10.1016/j.egypro.2014.01.154.

Rakousky, C., Reimer, U., Wippermann, K., Carmo, M., Lueke, W., and Stolten, D. (2016). An analysis of degradation phenomena in polymer electrolyte membrane water electrolysis. *J. Power Sources*, 326, pp. 120–128. doi: 10.1016/j.jpowsour.2016.06.082.

Ram, M., Bogdanov, D., Aghahosseini, A., Oyewo, S.A., Child, M., Caldera, U., Sadovskaia, K., Farfan, J., Barbosa, L.S., Fasihi, M., Khalili, S., Dalheimer, B., Gruber, G., Traber, T., Caluwe, F.D., Fell, H.J., and Breyer, C. (2019). Global Energy system based on 100% renewable energy — Power, heat, transport, and desalination sectors. In: *Study by Lappeenranta University of Technology and Energy Watch Group*. Lappeenranta, Berlin.

Rodriguez, J.R., Pontt, J., Silva, C., Wiechmann, E.P., Hammond, P.W., Santucci, F.W., Alvarez, R., Musalem, R., Kouro, S., and Lezana, P. (2005). Large current rectifiers: State of the art and future trends. *IEEE Transactions on Industrial Electronics*, 52(3), pp. 738–746.

Royal Dutch Shell (2018). *The road to sustaineable fuels for zero emissions mobility — status of and perspectives for Power-to-Liquids fuels*. 39th International Vienna Motor Symposium.

Schalenbach, M., Carmo, M., Fritz, D.L., Mergel, J., and Stolten, D. (2013). Pressurized PEM water electrolysis: Efficiency and gas crossover. *International Journal of Hydrogen Energy*, 38(35), pp. 14921–14933. doi: 10.1016/j.ijhydene.2013.09.013.

Schalenbach, M., Tjarks, G., Carmo, M., Lueke, W., Mueller, M., and Stolten, D. (2016). Acidic or Alkaline? Towards a New Perspective on the Efficiency of Water Electrolysis. *J. Electrochem. Soc.*, 163(11), pp. F3197–F3208. doi: 10.1149/2.0271611jes.

Schmidt, O., Gambhir, A., Staffell, I., Hawkes, A., Nelson, J., and Few, S. (2017). Future cost and performance of water electrolysis: An expert elicitation study. *International Journal of Hydrogen Energy*, 42(52), pp. 30470–30492. doi: 10.1016/j.ijhydene.2017.10.045.

Solanki, J., Fröhleke, N., Böcker, J., and Wallmeier, P. (2012). Analysis, Design and Control of 1 MW, High Power Factor and High Current Rectifier System. In: *Proc. IEEE Energy Conversion Congress and Exposition (ECCE ´12)*, pp. 1725–1732. Raleigh, United States. ISBN 9781467308038.

Stwertka, A. (2018). *A guide to the elements*, 4th edn. NY: Oxford University Press. ISBN 9780190682347.

Thounthong, P., Davat, B., Raël, S., and Sethakul, P. (2009). Fuel cell high-power applications. *IEEE Industrial Electronics Magazine*, 3(1), pp. 32–46. doi: 10.1109/MIE.2008.930365.

Tianjin Mainland Hydrogen Equipment (2019). *Hydrogen generator*. URL `http://www.cnthe.com/en/product-35-43-0.html`. [Accessed: 23-Aug-2019].

Trinke, P., Haug, P., Brauns, J., Bensmann, B., Hanke-Rauschenbach, R., and Turek, T. (2018). Hydrogen Crossover in PEM and Alkaline Water Electrolysis: Mechanisms, Direct Comparison and Mitigation Strategies. *Journal of Electrochemical Society*, 165(7), pp. F502–F513. doi: 10.1149/2.0541807jes.

Ueda, D. (2017). Chapter 1 — Properties and Advantages of Gallium Nitride. In: Meneghini, M., Meneghesso, G., and Zanoni, E., eds, *Power GaN devices — Materials, applications, and reliability*, pp. 1–26. Springer International Publishing Switzerland. ISBN 978-3-319-43199-4.

Ulleberg, Ø. (2003). Modeling of advanced alkaline electrolyzers: A system simulation approach. *International Journal of Hydrogen Energy*, 28(1), pp. 21–33. doi: 10.1016/S0360-3199(02)00033-2.

Ursúa, A., Gandía, L.M., and Sanchis, P. (2012). Hydrogen production from water electrolysis: Current status and future trends. *Proceedings of the IEEE*, 100(2), pp. 410–426. doi: 10.1109/JPROC.2011.2156750.

Ursúa, A. and Sanchis, P. (2012). Static-dynamic modelling of the electrical behaviour of a commercial advanced alkaline water electrolyser. *International Journal of Hydrogen Energy*, 37(24), pp. 18598–18614. doi: 10.1016/j.ijhydene.2012.09.125.

Ursúa, A., Sanchis, P., and Marroyo, L. (2013). Chapter 14 — Electric Conditioning and Efficiency of Hydrogen Production Systems and Their Integration with Renewable Energies. In: Gandía, L., Arzamendi, G., and Diéguez, P., eds, *Renewable Hydrogen Technologies*, pp. 333–360. Amsterdam: Elsevier. ISBN 978-0-444-56352-1.

Ursúa, A., Barrios, E.L., Pascual, J., Martín, I.S., and Sanchis, P. (2016). Integration of commercial alkaline water electrolysers with renewable energies: Limitations and improvements. *International Journal of Hydrogen Energy*, 41(30), pp. 12852–12861. doi: 10.1016/j.ijhydene.2016.06.071.

Publication I

Koponen, J., Ruuskanen, V., Kosonen, A., Niemelä, M., and Ahola, J.
Effect of converter topology on the specific energy consumption of alkaline water electrolyzers

IEEE Transactions on Power Electronics,
vol. 34, no. 7, Jul. 2019.

Effect of Converter Topology on the Specific Energy Consumption of Alkaline Water Electrolyzers

Joonas Koponen, Vesa Ruuskanen, Antti Kosonen, Markku Niemelä, and Jero Ahola

***Abstract*—Water electrolysis will be used to produce renewable hydrogen for energy storage and Power-to-X applications in the future renewable-energy-based energy systems. Therefore, the energy efficiency of hydrogen production will probably become a major issue. In this study, the effect of practical supply power converters on the specific energy consumption of megawatt (MW)-scale alkaline electrolyzers is studied and compared with an ideal dc power supply. The current quality and the stack specific energy consumption are studied in the case of traditional thyristor rectifiers and a transistor-based converter. The stack specific energy consumption is analyzed based on the simulated current waveforms and the electrical equivalent circuit of the electrolyzer stack. It is found that the transistor-based converter offers up to 14% lower electrolyzer stack specific energy consumption than the 6-pulse thyristor rectifier and up to 9.2% lower electrolyzer stack specific energy consumption than the 12-pulse thyristor rectifier as the current varies between 5000 and 1000 A. The simulated change in the stack specific energy consumption of the MW-scale alkaline water electrolyzer outweighs the losses occurring in the rectifiers. Further, selection of the ac voltage level may have a more adverse effect on the stack specific energy consumption with the thyristor rectifier topologies compared with the transistor-based topologies.**

***Index Terms*—Electrochemical devices, energy efficiency, hydrogen, rectifiers.**

I. Introduction

WATER electrolyzers may be the main electricity consumers in the future as the whole energy sector has to be based on renewable energy sources [1]. Renewable hydrogen is needed to produce carbon-neutral fuels for transportation and seasonal energy storages, as well as raw materials for the chemical and steel industries [2]–[6]. Therefore, optimization of the specific energy consumption of water electrolyzers is essential for future energy systems. Water electrolysis has been identified as the main cost contributor to the capital expenditure (CAPEX) of Power-to-Gas systems [2], [7], [8]. The CAPEX of the water electrolyzer supply converter is approximately 15% of the CAPEX of the electrolyzer system for both alkaline and proton exchange membrane (PEM) water electrolyzer technologies [9].

In Power-to-X systems, where electrical energy is converted into other forms of energy, the water electrolyzer stack is the main energy consumer, and hydrogen is the main energy carrier in the end product. The hydrogen production rate of a water electrolyzer is directly proportional to the mean value of the dc current supplied to the electrodes, and thus, the cost of electricity is the main contributor to the cost of electrolytic hydrogen gas. State-of-the-art commercial alkaline and PEM water electrolyzers can reach voltage efficiencies up to 82% [10], when compared with the minimum energy requirement defined by the higher heating value of hydrogen gas, 39.4 kW h kg^{-1}. However, owing to the requirement for high dc currents, the rectifiers in conventional industrial water electrolyzers are typically based on thyristors and diodes [11]. Switching according to the line frequency generates harmonics to the supplied current and voltage causing additional heat losses in the water electrolysis process [12], [13]. Application of more modern power electronic converters could be beneficial, but would require modular conversion structures to share the supplied currents among suitable levels for semiconductors using forced commutation, such as an insulated-gate bipolar transistor (IGBT). The optimization of the electrolyzer stack losses outweighs the losses in the power electronic converters as the rectifiers used in conventional water electrolysis systems can reach efficiencies exceeding 98%.

Possible effects of inverter current ripple on PEM fuel cell operation have been introduced in [14]. Low-frequency current ripple was found to have an impact on the performance, efficiency, and lifetime of a solid oxide fuel cell in [15]. However, the fuel cell inverters—typically preceded by a dc–dc boost converter if voltage level increase is required before the inverter [16]—are typically transistor-based topologies with generally lower amplitude current ripple compared to the dc current quality seen in water electrolyzers supplied by traditional thyristor rectifiers [17]. For fuel cells, the switching frequency has been recommended to be greater than 1.25 kHz and the fuel cell current ripple lower than 5% to prevent cell operation disturbance [17]. The fuel cell inverter current quality and sizing of the filter capacitor are discussed in [18]. The load transients and current ripple has been shown to have a significant effect on the area specific resistance (ASR) degradation of the planar solid oxide fuel cell [19]. However, the effect of current ripple on electrolytic cell lifetime is still a key research question for water electrolyzers [9], [20].

The effects of power conditioning on the specific energy consumption of water electrolyzers were introduced in [11] and [12], where one thyristor-based topology was compared with a transistor-based one. The comparison was conducted by analyzing the resulting specific energy consumptions for a

Manuscript received April 4, 2018; revised June 29, 2018 and August 31, 2018; accepted October 5, 2018. Date of publication October 16, 2018; date of current version May 2, 2019. Recommended for publication by Associate Editor S. K. Mazumder. *(Corresponding author: Joonas Koponen.)*

The authors are with the LUT School of Energy Systems, Lappeenranta University of Technology, 53850 Lappeenranta Finland (e-mail: joonas.k.koponen@lut.fi; vesa.ruuskanen@lut.fi; antti.kosonen@lut.fi; markku.niemela@lut.fi; jero.ahola@lut.fi).

Color versions of one or more of the figures in this paper are available online at http://ieeexplore.ieee.org.

Digital Object Identifier 10.1109/TPEL.2018.2876636

5-kW alkaline water electrolyzer. A lab-scale alkaline water electrolyzer was analyzed in [21], where steady dc current resulted in minimized cell efficiency loss.

The power quality of the ac and dc sides of a thyristor rectifier with a distribution static compensator (DSTATCOM) was analyzed for example in [22], but the effect of power quality on the load behavior was not considered. A dc chopper was introduced for electrochemical applications in [23]. The chopper rectifier was stated to have a higher efficiency than a thyristor-based rectifier in the whole operating range despite the lowest output voltages. The three-phase chopper with a diode rectifier was shown to have a higher efficiency than a thyristor bridge with a DSTATCOM [24]. Efforts have been made to apply IGBTs to specific high-current rectification applications [25], [26]. Yet, thyristor topologies are the traditional, most common solution for high-current, high-power applications [24]–[26].

In this paper, the effect of power quality on the energy consumption of an MW-scale alkaline water electrolyzer stack is analyzed using simulation tools. A simplified model for the MW-scale water electrolyzer is established based on the measured performance of a small-scale alkaline water electrolyzer. The rectifier topologies selected for analysis are 1) a 6-pulse thyristor rectifier, 2) a 12-pulse thyristor rectifier, and 3) a 6-pulse diode bridge followed by an IGBT-based chopper. The transistor-based topology is selected to represent the more modern, practical alternative to the typical thyristor rectifiers [24], [27]. The current quality of the transistor-based topology could be further improved by reselecting the switching frequency and resizing the reactive components. However, this paper concentrates on the main differences between the thyristor and transistor topologies in the alkaline water electrolyzer supply converters, and the filter design is not considered.

The following are the main contributions of this paper. 1) The current and voltage waveforms of the MW-scale alkaline electrolyzer stack are simulated in the case of thyristor rectifiers and the transistor-based chopper power supply converter. 2) The resulting water electrolyzer stack specific energy consumptions as a function of load current are compared with a pure dc supply. 3) The effect of the ac voltage level selection on the stack specific energy consumption is studied. 4) The effect of the converter topology on the water electrolyzer controllability and implications of stack degradation for the ac voltage level selection are discussed.

This paper is organized as follows. Section II introduces the basics of the electrochemistry in water electrolysis processes and describes the simplified electrical model of the MW-scale alkaline electrolyzer stack. The power quality and specific energy consumption of the alkaline electrolyzer with 6-pulse and 12-pulse thyristor rectifiers and a transistor chopper-based converter are studied in Section III. Section IV concludes the paper.

II. Method of Analysis

The hydrogen production rate (mol s^{-1}) of a single electrolytic cell is linearly proportional to the current

$$f_{H_2} = \eta_F \frac{i_{cell} A_{cell}}{zF} \tag{1}$$

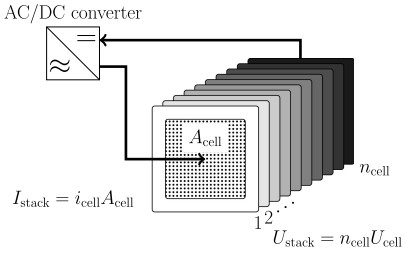

(a)

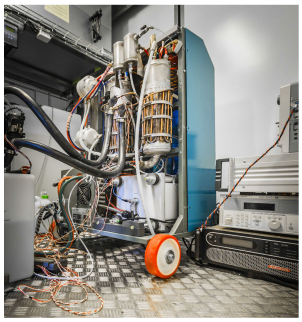

(b)

Fig. 1. Operating principle of the bipolar electrolyzer stack with series-connected cells and the actual electrolyzer stack of the Baby McPhy alkaline water electrolyzer; the nominal hydrogen production rate of the electrolyzer is 0.4 N m^3 h^{-1} with the electrical power of 2.8 kW. (a) Principle of the dc power supply of the bipolar electrolyzer stack. (b) Electrolyzer stack of the Baby McPhy alkaline water electrolyzer with 30 cells connected in series.

where f_{H_2} is the hydrogen production rate (mol s^{-1}), z is the number of moles of electrons transferred in the reaction (for hydrogen, $z = 2$), F is the Faraday constant (9.6485×10^4 C mol^{-1}), i_{cell} is the current density (A cm^{-2}), A_{cell} is the effective cell area (cm^2), and η_F is the Faraday efficiency, also known as the current efficiency.

Experimental data are required to model the selected water electrolysis processes as shown in [13], [28], and [29]. The electrolytic cell voltage is a sum of the reversible voltage and additional overvoltages appearing in the electrolytic cell

$$U_{cell} = U_{rev} + U_{ohm} + U_{act} + U_{con} \tag{2}$$

where U_{cell} is the cell voltage, U_{rev} is the reversible voltage, which is the lowest voltage required for the water decomposition to occur, U_{ohm} is the overvoltage caused by ohmic losses in the cell elements, U_{act} is the activation overvoltage produced by electrode kinetics, and U_{con} is the concentration overvoltage resulting from mass transport processes [30]. The principle of the bipolar electrolyzer stack with series-connected cells and the actual stack of the studied alkaline electrolyzer are illustrated in Fig. 1.

In this study, a simplified electrical model of the stack is used for the simulation. The stack is assumed to operate under

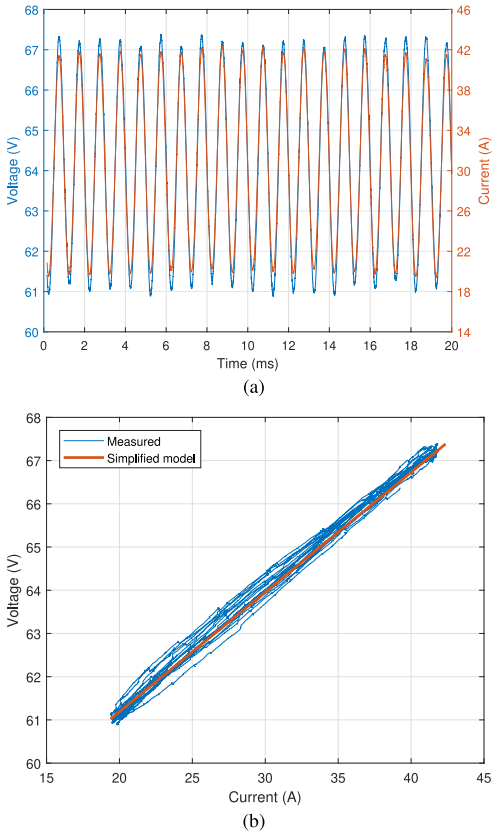

Fig. 2. Measured current and voltage waveforms of the Baby McPhy alkaline water electrolyzer. The measured voltage as a function of current is compared with a simplified model. (a) Voltage and current waveforms. (b) Voltage as a function of current.

constant temperature and pressure. Therefore, the reversible voltage is assumed to be constant and the overpotential caused by the stack current to be linearly dependent on the current amplitude

$$U_{\text{stack}} = U_{\text{rev,stack}} + RI_{\text{stack}} \tag{3}$$

where $U_{\text{rev,stack}}$ is the stack reversible voltage (V), R is the equivalent resistance of the cell (Ω), and I_{stack} is the stack current (A). The measured voltage and current waveforms of the alkaline electrolyzer in Fig. 1(b) with 30 cells connected in series are presented in Fig. 2(a). As there seems to be no phase shift between the voltage and the current despite the relatively high (1 kHz) ac ripple frequency, the stack impedance can be assumed to be purely resistive. Fig. 2(b) depicts the measured voltage as a function of current with the estimated voltage with a reversible voltage of 55.65 V and a stack equivalent resistance of 277 $\text{m}\Omega$.

Solanki *et al.* [22] used a similar kind of linear voltage equation for an MW-scale electrolyzer with $U_{\text{rev,stack}}$ values from 142 to 150 V and R values from 4.8 to 15.4 $\text{m}\Omega$. In this study, the values of the Baby McPhy alkaline electrolyzer can be scaled to the MW range by multiplying the voltage by a factor of three, as a result of which the total number of series-connected cells is 90 with the nominal voltage of $U_{\text{stack}} = 200$ V. The current, linearly proportional to the active cell area [see Fig. 1(a)], is scaled by a factor of one hundred and the nominal current is chosen to be $I_{\text{stack}} = 5000$ A. Therefore, the voltage equation parameters are selected to be $U_{\text{rev,stack}} = 150$ V and $R = 10\,\text{m}\Omega$. The key electrical parameters of the commercial small-scale alkaline water electrolyzer and the scaled water electrolyzer used in the simulations are collected in Table I.

The voltage and current waveforms of the electrolyzer stack supplied with various power supply converters are simulated using the Simscape environment in the MATLAB Simulink software. The electrical power of the stack is defined based on the stack current and voltage as a function of time. The hydrogen production is calculated based on the current with (1) neglecting the effect of the Faraday efficiency, as a result of which the average hydrogen production is only a function of current dc value. However, the Faraday efficiency has been suggested to be a function of current density in constant dc current operation in [31], where the measured Faraday efficiency varied as a nonlinear function of current density in the range of 28%–99%. Further investigations are required to explicate the instantaneous Faraday efficiency of water electrolyzers on the millisecond timescale. The specific energy consumption E_{s} of an electrolysis process can be obtained from

$$E_{\text{s}} = \frac{\int_0^t I_{\text{stack}} U_{\text{stack}}\, dt}{\int_0^t f_{\text{H}_2}\, dt}. \tag{4}$$

The higher heating value (HHV) is the minimum energy required to produce hydrogen gas with a thermoneutral process. The per mass unit HHV of hydrogen gas is 39.4 kW h kg^{-1}, which can be assumed to represent the energy consumption of the process with 100% efficiency.

III. Results

The output current and voltage quality of the 6-pulse and 12-pulse thyristor rectifiers and the transistor-based converter is studied. The specific energy consumption of the electrolyzer is analyzed as a function of dc current in the range from 1000 to 5000 A level by setting the thyristor firing angle and the transistor pulse width with a proportional-integral (PI) controller in Simulink. Further, the effect of the ac voltage level on the electrolyzer energy efficiency is considered.

A. 6-Pulse Thyristor Bridge

A 6-pulse thyristor rectifier is connected to a three-phase voltage source and no filtering is used in either side of the rectifier bridge. The minimum rms value of the main voltage of the supply grid U_{ac} is selected to be 150 V to achieve a current of 5000 A almost at the full voltage of the rectifier. The voltage

TABLE I
ELECTRICAL PARAMETERS OF THE MEASURED MCPHY BABYPIEL ALKALINE WATER ELECTROLYZER AND THE SCALED 1-MW INDUSTRIAL ALKALINE WATER ELECTROLYZER

	I_{stack} (A)	U_{stack} (V)	P_{stack} (kW)	n_{cell} (-)	R (mΩ)	$U_{\text{rev,stack}}$ (V)
BabyPIEL	35	65	2.8	30	277	55.65
Scaled electrolyzer	5000	200	1000	90	10	150

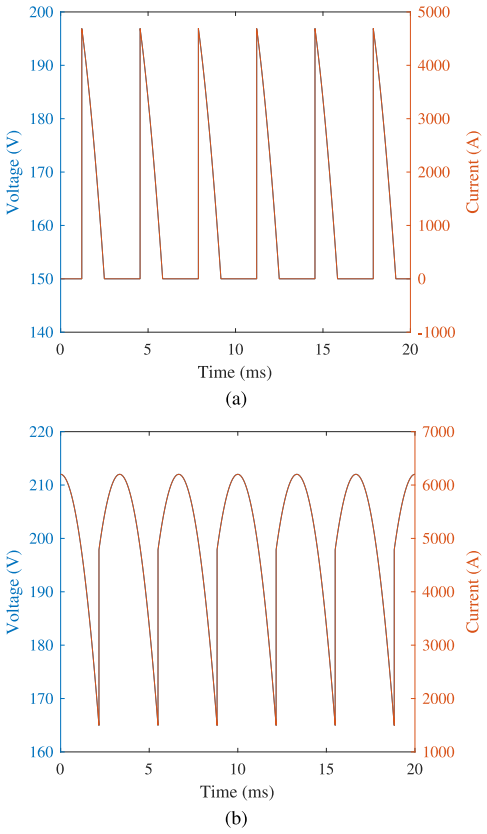

Fig. 3. Voltage and current waveforms of the 6-pulse rectifier at certain dc current levels, when $U_{\text{ac}} = 150$ V. (a) 1000 A. (b) 5000 A.

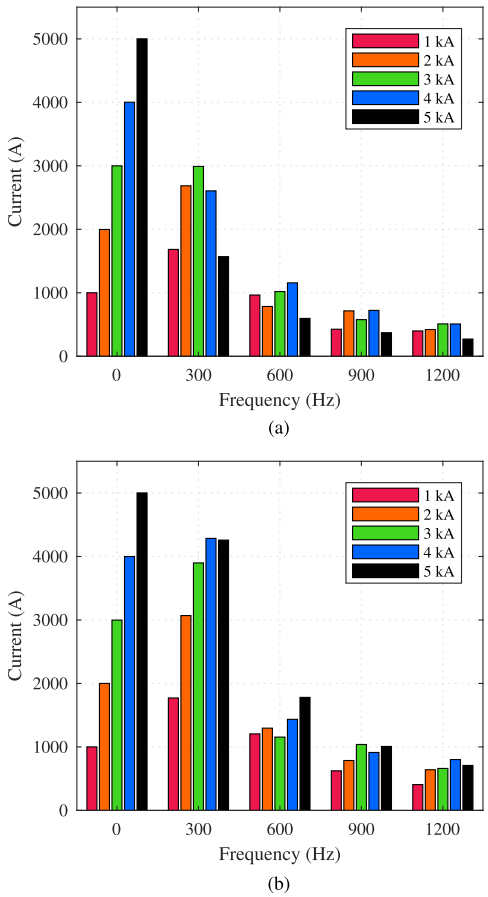

Fig. 4. Current frequency content with the 6-pulse rectifier at certain dc current levels. (a) $U_{\text{ac}} = 150$ V. (b) $U_{\text{ac}} = 175$ V.

and current waveforms with the currents of 1000 and 5000 A are given in Fig. 3.

The thyristor rectifier excites significant current ripple. At partial loads, the current momentarily reaches a zero value. The frequency components of the current are given as a function of current mean value at two different grid voltage values in Fig. 4.

It can be seen that the amplitude of the 300-Hz current ripple exceeds the current dc level at loads below 3000 A. Further, the increased grid voltage leads to a higher firing angle of the thyristors and, thereby, higher current ripple values. The specific energy consumption of the electrolyzer supplied with the 6-pulse rectifier is compared with a pure dc supply in Fig. 5.

The current ripple excited by the thyristor bridge significantly increases the energy consumption of the electrolyzer stack. The effect of the power supply is emphasized at the lowest dc current levels and the highest grid voltage levels. In the studied case, at the grid voltage of 150 V, the energy consumption with the 6-pulse rectifier is 14.4% higher than with the pure dc supply

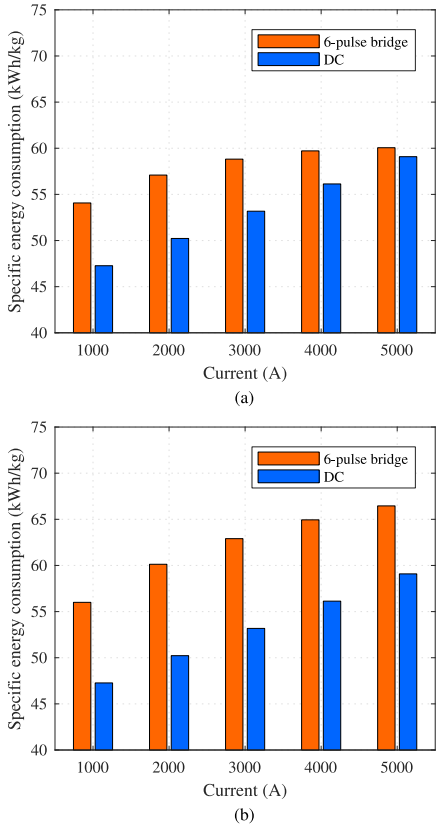

Fig. 5. Specific energy consumption of the electrolyzer supplied with the 6-pulse rectifier and pure dc at certain dc current levels. (a) $U_{\mathrm{ac}} = 150$ V. (b) $U_{\mathrm{ac}} = 175$ V.

at the partial load of 1000 A and 1.6% higher at the full load. At the grid voltage of 175 V, the energy consumption with the 6-pulse rectifier is 18.5% higher than with the pure dc supply at the partial load of 1000 A and 12.5% higher at the full load. As the grid voltage level affects the required firing angle and the current waveform, the specific energy consumption with the 6-pulse bridge is given as a function of dc current level and grid voltage in Fig. 6.

Obviously, the dc current level is the main factor affecting the specific energy consumption. However, the effect of the supply ac voltage cannot be neglected either, but the voltage level must be matched with the maximum current of the electrolyzer at the zero firing angle of the thyristor bridge.

B. 12-Pulse Thyristor Bridge

A 12-pulse thyristor rectifier is implemented by connecting two 6-pulse rectifiers in series as shown for example in [22].

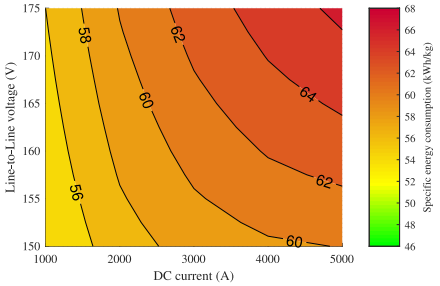

Fig. 6. Specific energy consumption of the electrolyzer as a function of dc current level and the line-to-line voltage of the 6-pulse rectifier input.

The ac supplies of the rectifiers are phase shifted by 30° from each other. Further, the voltage amplitude of the ac supplies is scaled by a factor of $\frac{\sqrt{2}}{\sqrt{3}+1}$ to achieve the same dc voltage peak values as in the case of the 6-pulse rectifier. The voltage and current waveforms with the currents of 1000 and 5000 A are shown in Fig. 7.

The voltage and current ripple are significantly lower with the 12-pulse rectifier than with the 6-pulse rectifier. The frequency components of the current are given as a function of current mean value at two different grid voltage values in Fig. 8.

The dominating harmonic component at 600 Hz has significantly lower amplitudes than the 300 Hz component in the case of the 6-pulse rectifier. The specific energy consumption of the electrolyzer supplied with the 12-pulse rectifier is compared with a pure dc supply in Fig. 9.

The 12-pulse rectifier offers a better efficiency than the 6-pulse rectifier especially at partial loads around 50% of the nominal current. In the studied case, at the grid voltage of 150 V, the energy consumption with the 12-pulse rectifier is 9.0% higher than with the pure dc supply at the partial load of 1000 A and 0.9% higher at the full load. At the grid voltage of 175 V, the energy consumption with the 12-pulse rectifier is 11.7% higher than with the pure dc supply at the partial load of 1000 A and 4.6% higher at the full load. As the grid voltage level highly affects the energy consumption also in the case of the 12-pulse rectifier, the specific energy consumption with the 12-pulse bridge is presented as a function of dc current level and grid voltage in Fig. 10.

The 12-pulse rectifier offers a better efficiency than the 6-pulse rectifier over the whole operating range. However, it is pointed out that the losses of the rectifier itself are higher in the case of the 12-pulse rectifier as the current must flow through two 6-pulse rectifiers connected in series.

C. Transistor-Based Topology

A simple single leg step-down dc/dc converter is selected to study the characteristics of transistor-based forced commutation power supply topologies. A three-legged transistor topology is depicted in [24]. In this study, the dc/dc converter is supplied by a 6-pulse rectifier instead of the 12-pulse rectifier common

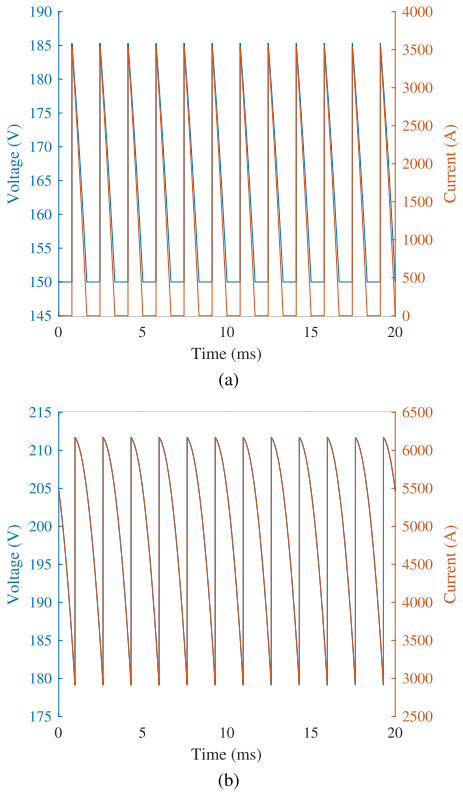

Fig. 7. Voltage and current waveforms of the 12-pulse rectifier at certain dc current levels, when $U_{ac} = 150$ V. (a) 1000 A. (b) 5000 A.

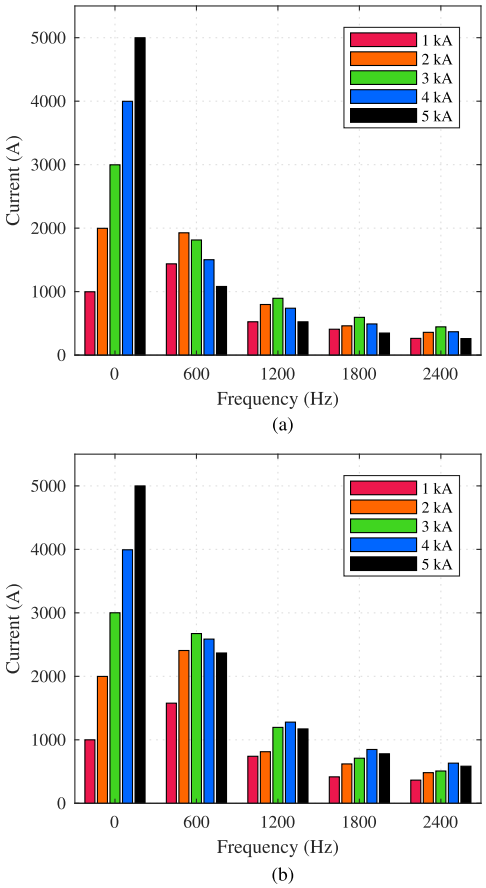

Fig. 8. Current frequency content with the 12-pulse rectifier at certain dc current levels. (a) $U_{ac} = 150$ V. (b) $U_{ac} = 175$ V.

in the literature. A capacitor of 1 mF is used to stabilize the dc link voltage. In [24], there are 96-μH inductors in each of the three output legs of the converter together with an output filtering capacitor. In this study, no capacitor is applied and a single 32-μH inductor is used as an output filter. Further, the switching frequency of the transistor is selected to be 1 kHz. The voltage and current waveforms with the currents of 1000 and 5000 A are shown in Fig. 11.

The effect of switching frequency is clearly seen at the partial load as the grid-excited pulsation of the dc link voltage is emphasized at the full load. The frequency components of the current are given as a function current mean value at two different grid voltage values in Fig. 12. The ripple amplitudes are far lower in the case of the transistor-based converter than with the thyristor rectifiers. The specific energy consumption of the electrolyzer supplied with the forced commutation rectifier is compared with the pure dc supply in Fig. 13.

The efficiency of the transistor converter-fed electrolyzer stack is only slightly higher than with the pure dc supply at all loads. Further, also the effect of the grid voltage on the electrolyzer stack efficiency is small. At the grid voltage of 150 V, the energy consumption with the transistor converter is only 0.6% higher than with the pure dc supply at the partial load of 1000 A and 0.02% higher at the full load. At the grid voltage of 175 V, the energy consumption with the transistor converter is 1.5% higher than with the pure dc supply at the partial load of 1000 A and 0.9% higher at the full load. Obviously, the current quality and the output filter cost must be optimized for each case. The specific energy consumption with the transistor converter is presented as a function of dc current level and grid voltage in Fig. 14.

As the effect of ac voltage on the specific energy consumption of the elecrolyzer stack is almost insignificant, the specific energy consumption is practically only dependent on the dc

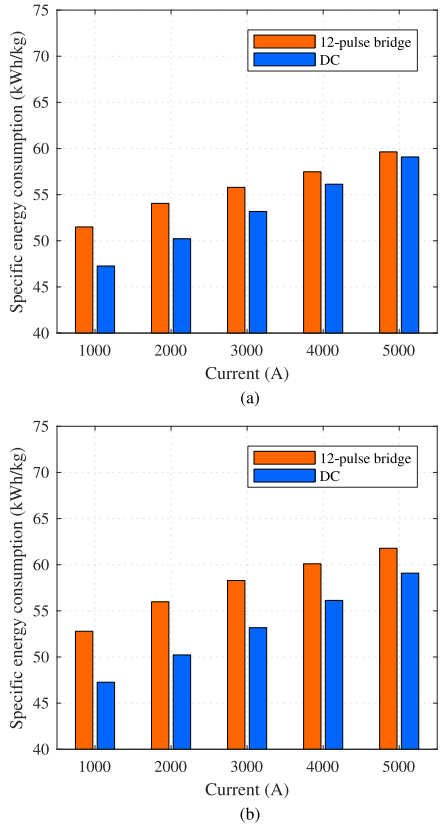

Fig. 9. Specific energy consumption of the electrolyzer supplied with the 12-pulse rectifier and pure dc at certain dc current levels. (a) $U_{ac} = 150$ V. (b) $U_{ac} = 175$ V.

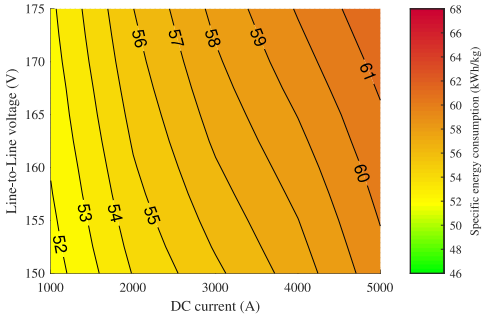

Fig. 10. Specific energy consumption of the electrolyzer as a function of dc current level and the line-to-line voltage of the 12-pulse rectifier input.

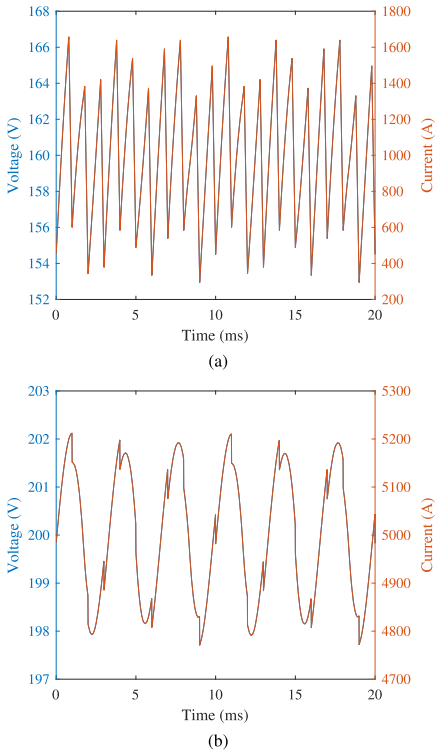

Fig. 11. Voltage and current waveforms of the buck rectifier at certain dc current levels, when $U_{ac} = 150$ V. (a) 1000 A. (b) 5000 A.

current level. Eventually, the current quality and the stack efficiency are determined by the design of the rectifier output filter. However, a transistor-based converter has been shown to be able to achieve a high current quality with an output filter consisting of only an inductor with an inductance in the range of tens of microhenrys.

D. Comparison of the Topologies

1) Current Quality: The amplitudes and frequencies of the dominating current harmonic components, found for 6-pulse and 12-pulse thyristor bridges and a buck converter in the previous section, are collected to Table II. It can be seen that the harmonic amplitude exceeds the dc current level at partial loads with both studied thyristor bridge topologies. Further, 12-pulse bridge excites slightly lower harmonic amplitudes with higher frequency compared with the 6-pulse bride. However, only buck rectifier is able to offer current harmonics in the amplitude and frequency range allowed for fuel cells according to the literature [17]. The current quality of the buck rectifier could be further improved by selecting higher inductance output filter or applying parallel converter legs.

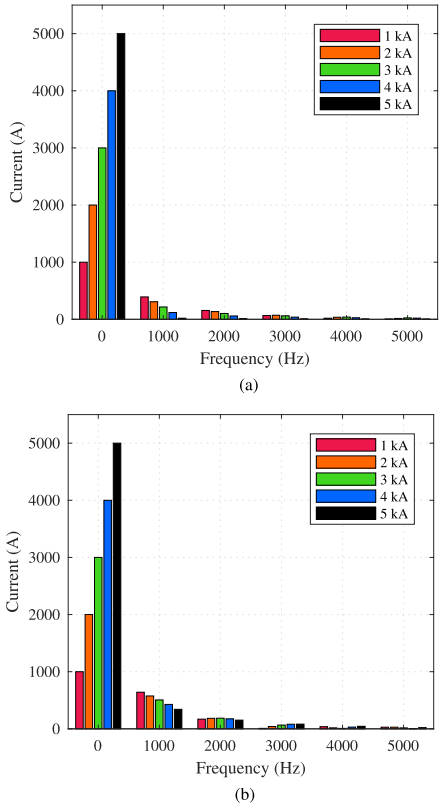

Fig. 12. Current frequency content with the buck rectifier at certain dc current levels. (a) $U_{\text{ac}} = 150$ V. (b) $U_{\text{ac}} = 175$ V.

2) Specific Energy Consumption: The differences in the resulting mean specific energy consumptions between the rectifier topologies originate from the dc current waveforms. An increase in current strongly contributes to the dissipated power because of the quadratic relationship of current in Ohmic heating. Therefore, the closer the stack dc current waveform is to pure dc current, the lower the specific energy consumption of a water electrolyzer stack is. The resulting stack specific energy consumptions with the analyzed converter topologies are presented in Table III. With the 6-pulse thyristor rectifier, at the 150-V grid ac voltage, the mean stack specific energy consumption is 60.1 kW h kg^{-1} at the full load of 5000 A and 54.1 kW h kg^{-1} at the minimum load of 1000 A. However, the stack specific energy consumption varies from 48.7 to 62.6 kW h kg^{-1} and from 44.3 to 58.2 kW h kg^{-1} at the full and minimum loads, respectively, when the specific energy is calculated point-by-point according to the stack voltage and stack current waveforms shown in Fig. 15. Additionally, as a result of the considerable 300-Hz accurrent ripple, the instantaneous stack current reaches 0 A at dc current operating points $\leq$4000 A. The minimum stack

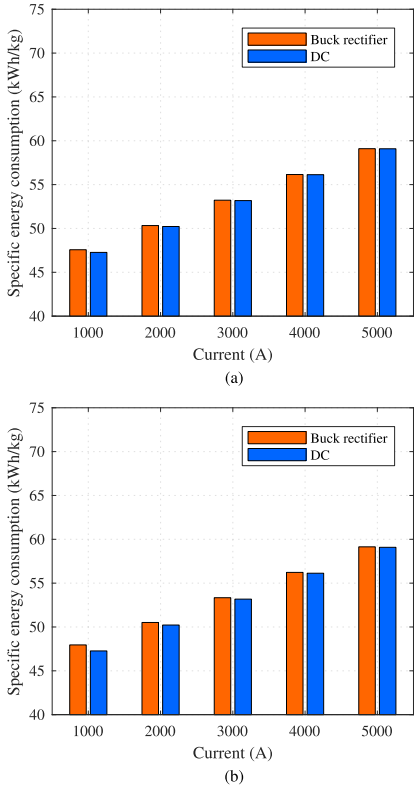

Fig. 13. Specific energy consumption of the electrolyzer supplied with the buck rectifier and pure dc at certain dc current levels. (a) $U_{\text{ac}} = 150$ V. (b) $U_{\text{ac}} = 175$ V.

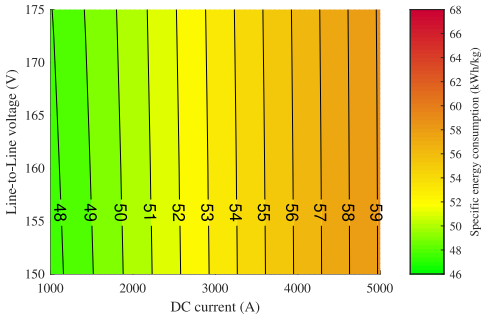

Fig. 14. Specific energy consumption of the electrolyzer as a function of dc current level and the line-to-line voltage of the transistor converter input.

TABLE II
DOMINATING CURRENT HARMONIC COMPONENTS OF THE STUDIED CONVERTER TOPOLOGIES COMPARED WITH THE CURRENT RIPPLE ALLOWED FOR FUEL CELLS IN THE LITERATURE [17]

		$U_{AC} = 150\,V$					
	Fuel cell reference	6-pulse bridge		12-pulse bridge		Buck rectifier	
		1000 A	5000 A	1000 A	5000 A	1000 A	5000 A
Frequency (Hz)	1250	300	300	600	600	1000	1000
Amplitude (%)	5	168	31	144	22	39	0.4
		$U_{AC} = 175\,V$					
	Fuel cell reference	6-pulse bridge		12-pulse bridge		Buck rectifier	
		1000 A	5000 A	1000 A	5000 A	1000 A	5000 A
Frequency (Hz)	1250	300	300	600	600	1000	1000
Amplitude (%)	5	177	85	158	47	64	7

For the buck rectifier, a constant dc link voltage is assumed.

TABLE III
SPECIFIC ENERGY CONSUMPTION (SEC) WITH THE STUDIED CONVERTER TOPOLOGIES COMPARED WITH PURE DC SUPPLY

			$U_{AC} = 150\,V$					
	DC		6-pulse bridge		12-pulse bridge		Buck rectifier	
	1000 A	5000 A	1000 A	5000 A	1000 A	5000 A	1000 A	5000 A
SEC (kW h kg^{-1})	47.27	59.09	54.07	60.06	51.5	59.64	47.57	59.10
SEC (% of DC)	100	100	114.4	101.6	108.9	100.9	100.6	100.0
			$U_{AC} = 175\,V$					
	DC		6-pulse bridge		12-pulse bridge		Buck rectifier	
	1000 A	5000 A	1000 A	5000 A	1000 A	5000 A	1000 A	5000 A
SEC (kW h kg^{-1})	47.27	59.09	56.00	66.45	52.79	61.78	47.95	59.14
SEC (% of DC)	100	100	118.5	112.5	111.7	104.5	101.4	100.1

current as a function of electrolyzer load is illustrated for the three different topologies in Fig. 16.

In Fig. 15, the stack specific energy consumption with the 12-pulse rectifier varies from 52.9 to 62.5 kW h kg^{-1} and from 44.3 to 54.8 kW h kg^{-1} at the full and minimum loads, respectively. Because of the 600-Hz ac current ripple, the instantaneous stack current reaches 0 A at dc current operating points $\leq$3000 A. With the transistor-based converter, the point-by-point stack specific energy consumption varies only slightly, and the instantaneous stack current remains above the 0 A level at all analyzed loads (1000 to 5000 A). If the current is not allowed to reach a zero value during operation, the buck rectifier can offer a significantly wider operating area than the thyristor rectifiers. This may be essential in the renewable energy applications, where electrolyzers are a key component in the electricity grid frequency control system.

3) Converter Losses: The internal losses of the converters are roughly estimated by the threshold voltage and on-state resistance of the semiconductor components. The component types are selected based on [24]. In the 6-pulse rectifier there are two thyristors connected in parallel to limit the current of the individual thyristor. The 12-pulse rectifier consists of two series-connected 6-pulse bridges. Therefore, the internal losses of the 12-pulse rectifier are approximately twice as high as the 6-pulse rectifier losses. In the buck rectifier, there are two diodes in parallel in the 6-pulse diode rectifier bridge. On the dc side, there are 12 transistors and six free-wheeling diodes in parallel. The switching ON and OFF energies of the IGBT at the full load are 5 and 16.5 mJ, respectively. At the switching frequency of 1 kHz, the switching loss of a single transistor would be only 21.5 W, which is insignificant in this study. Further, the losses of the inductive and capacitive filters are neglected in the study. The equivalent circuit parameters of the components are given in Table IV.

The loss power of each component is calculated separately based on the simulated current waveforms. The converter losses of the studied topologies are compared with each other at the stack current of 5000 A in Table V.

The converter losses, even at the full load, are less than 3% of the energy consumption of the electrolyzer stack, as the stack specific energy consumption is roughly 60 kW h kg^{-1} at the dc current level of 5000 A. Therefore, the effect of current quality on the energy consumption of the stack is much more significant than the converter losses. Further, improving the power quality does not only affect the energy consumption of the stack, but the enhanced power quality may also have a positive effect on the lifetime of the electrolyzer stack.

4) AC Voltage Selection: Finally, selection of the ac voltage level should be considered. In Section III, the simulated stack specific energy consumption remained invariable to the ac voltage only with the transistor-based converter topology. With both the 6-pulse and 12-pulse thyristor rectifiers, the ac voltage

TABLE IV
EQUIVALENT CIRCUIT PARAMETERS OF THE SEMICONDUCTORS FOR CONVERTER LOSS ESTIMATION

	Threshold voltage (V)	Resistance (mΩ)
Diodes and thyristors (TZ800N12KOF)	0.82	0.17
IGBT transistors (FD600R06ME3)	0.80	0.80

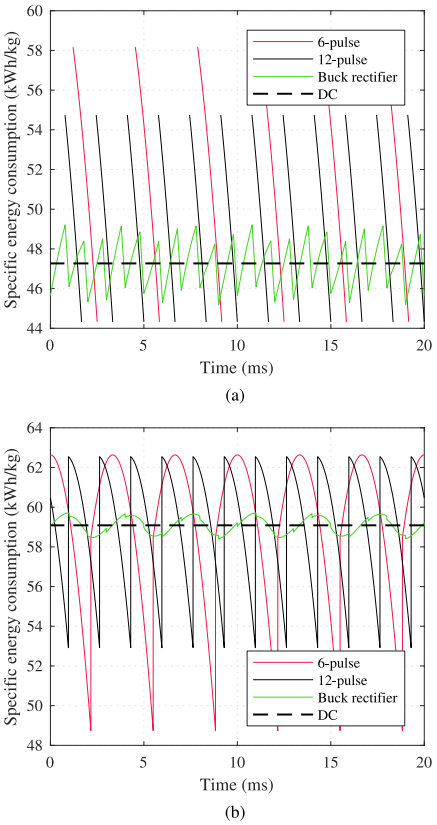

Fig. 15. Electrolyzer stack specific energy comparison for the three rectifier topologies and an ideal dc power supply when $U_{ac} = 150$ V. (a) 1000 A. (b) 5000 A.

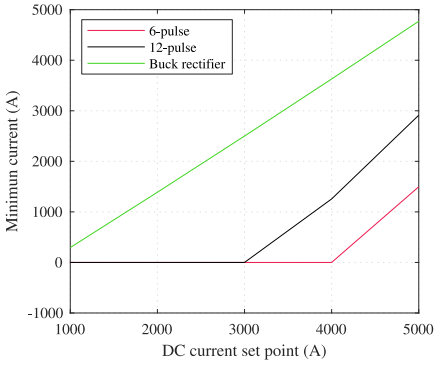

Fig. 16. Minimum current of a rectified waveform as a function of electrolyzer stack current set point when $U_{ac} = 150$ V.

has an impact on the resulting stack specific energy consumption (see Table III). Therefore, a dependence on the ac voltage level hinders the specific energy consumption optimization task. Furthermore, selection of the ac voltage level may have to take into account the voltage degradation of individual electrolytic cells, especially if the ac voltage level cannot be controlled by the supply transformer with on-load tap changer. As the cells age, their voltage increases at a rate typically described in μV h [9]. For alkaline water electrolyzers, stack lifetime values have been suggested to be in the range of 60 000–90 000 h and cell voltage degradation rates 0.4–5.0 μV h^{-1} [9]. If the degradation rate of 5 μV h^{-1} is assumed to behave linearly for over 60 000 h for the studied 1-MW alkaline water electrolyzer (90 cells in series, $U_{stack} = 200$ V), the increase in the stack voltage would be 27 V (+13.5%). The voltage degradation rate then determines a system design criterion for the water electrolysis plant. The selection of the ac voltage level should consider the stack voltage and its increase over the stack lifetime, and the capability of the water electrolysis plant to later meet its technical specifications as an increased stack voltage level results in a higher specific energy consumption or a lower electrolytic gas production rate.

A 25-V increase in the ac voltage would correspond to an 11% increase in the stack specific energy consumption with the 6-pulse thyristor rectifier and a 4% increase with the 12-pulse thyristor rectifier, when nominal operation at 5000 A is considered. With the transistor-based topology, this impact of the ac voltage increase on the increase in the stack specific energy consumption would be marginal or negligible. At the 150-V ac voltage level, the alkaline electrolyzer stack specific energy consumption with the transistor-based converter topology is 1.6%–12.0% lower than with the 6-pulse thyristor rectifier depending on the stack dc current set point (5000–1000 A). Because of the increased ac voltage, especially the difference in specific energy consumption at the nominal current is emphasized (see Table III). Similar effect of the ac voltage on the stack specific energy consumption can be seen with the 12-pulse thyristor rectifier.

TABLE V
ESTIMATED CONVERTER LOSSES AND THE CONVERTER LOSS EFFECT ON THE SPECIFIC ENERGY CONSUMPTION AT THE CURRENT LEVEL OF 5000 A

	Loss power (kW)	Converter specific energy consumption ($\mathrm{kW\,h\,kg^{-1}}$)	Minimum current (A)	Maximum current (A)
6-pulse	13	0.8	1497	6201
12-pulse	26	1.5	2912	6171
Buck rectifier	17	1.0	4771	5212

The stack specific energy consumption in the full load operation is $60\ \mathrm{kW\ h\ kg^{-1}}$.

IV. CONCLUSION

Water electrolyzers require dc power, and their operation depends on electric conditioning. In this paper, the specific energy consumption of a 1-MW alkaline water electrolyzer ($U_{\mathrm{stack}} = 200$ V, $I_{\mathrm{stack}} = 5000$ A) stack is simulated with three distinct industrial rectifier topologies: 1) a 6-pulse thyristor rectifier; a 12-pulse thyristor rectifier; and 3) a transistor-based converter. The resulting stack specific energy consumptions are compared against an ideal dc power supply.

It was found that the transistor-based converter topology can offer up to 14% lower stack specific energy consumption than the 6-pulse thyristor rectifier and up to 9% lower stack specific energy consumption than the 12-pulse thyristor rectifier in the studied current and voltage range. Furthermore, the selection of the ac voltage level may have a more adverse effect on the resulting stack specific energy consumption with the thyristor rectifier topologies.

Future investigation on the specific energy analysis of water electrolyzers will focus on the Faraday efficiency—the ratio of the actual hydrogen production rate to the ideal hydrogen production rate—and how the harmonic components in the stack dc current may affect the hydrogen gas production. Furthermore, more detailed experimental work on the effect of load transients and current ripple on the electrochemical cell degradation phenomena used for water electrolysis is yet to be studied as most of the previous degradation studies have concentrated on fuel cell applications.

REFERENCES

[1] P. Schmidt, W. Zittel, W. Weindorf, and T. Raksha, "Renewables in Transport 2050 Empowering a sustainable mobility future with zero Final Report," FVV, Tech. Rep., 2016.

[2] M. Fasihi, D. Bogdanov, and C. Breyer, "Techno-economic assessment of Power-to-Liquids (PtL) fuels production and global trading based on hybrid PV-wind power plants," in *Proc. 10th Int. Renewable Energy Storage Conf.*, Düsseldorf, Germany, Mar. 2016, pp. 243–268.

[3] G. Pleßmann, M. Erdmann, M. Hlusiak, and C. Breyer, "Global energy storage demand for a 100% renewable electricity supply," *Energy Procedia*, vol. 46, pp. 22–31, 2014.

[4] J. Koponen, A. Kosonen, K. Huoman, J. Ahola, T. Ahonen, and V. Ruuskanen, "Specific energy consumption of PEM water electrolysers in atmospheric and pressurised conditions," in *Proc. 18th Eur. Conf. Power Electron. Appl.*, Karlsruhe, Germany, Sep. 2016, pp. 1–10.

[5] A. Kosonen *et al.*, "Optimization strategies of PEM electrolyser as part of solar PV system," in *Proc. 18th Eur. Conf. Power Electron. Appl.*, Karlsruhe, Germany, Sep. 2016.

[6] J. Koponen, A. Kosonen, V. Ruuskanen, K. Huoman, M. Niemelä, and J. Ahola, "Control and energy efficiency of PEM water electrolyzers in renewable energy systems," *Int. J. Hydrogen Energy*, vol. 42, no. 50, pp. 29648–29660, Dec. 2017.

[7] M. Lehner, R. Tichler, H. Steinmüller, and M. Koppe, *Power-to-Gas: Technol. Business Models*. New York, NY, USA: Springer International Publishing, 2014.

[8] M. Götz *et al.*, "Renewable power-to-gas: A technological and economic review," *Renewable Energy*, vol. 85, pp. 1371–1390, Jan. 2016.

[9] L. Bertuccioli, A. Chan, D. Hart, F. Lehner, B. Madden, and E. Standen, "Study on development of water electrolysis in the EU," Fuel Cells and Hydrogen Joint Undertaking Final Rep., Feb. 2014.

[10] M. Carmo, D. L. Fritz, J. Mergel, and D. Stolten, "A comprehensive review on PEM water electrolysis," *Int. J. Hydrogen Energy*, vol. 38, no. 12, pp. 4901–4934, Apr. 2013.

[11] A. Ursúa, P. Sanchis, and L. Marroyo, "Electric conditioning and efficiency of hydrogen production systems and their integration with renewable energies," in *Renewable Hydrogen Technologies*, L. Gandía, G. Arzamendi, and P. Diéguez, Eds., Amsterdam, The Netherlands: Elsevier, 2013, ch. 14, pp. 333–360.

[12] A. Ursúa, L. Marroyo, E. Gubía, L. M. Gandía, P. M. Diéguez, and P. Sanchis, "Influence of the power supply on the energy efficiency of an alkaline water electrolyser," *Int. J. Hydrogen Energy*, vol. 34, no. 8, pp. 3221–3233, May. 2009.

[13] A. Ursúa, I. S. Martín, and P. Sanchis, "Design of a programmable power supply to study the performance of an alkaline electrolyser under different operating conditions," in *Proc. 2nd IEEE Int. Energy Conf. Exhib.*, Florence, Italy, Sep. 2012, pp. 259–264.

[14] R. S. Gemmen, "Analysis for the effect of inverter ripple current on fuel cell operating condition," *J. Fluids Eng.*, vol. 125, no. 3, pp. 576–585, Jun. 2003.

[15] S. K. Mazumder *et al.*, "Solid-oxide-fuel-cell performance and durability: resolution of the effects of power-conditioning systems and application loads," *IEEE Trans. Power Electron.*, vol. 19, no. 5, pp. 1263–1278, Sep. 2004.

[16] E. Fontell, T. Kivisaari, N. Christiansen, J.-B. Hansen, and J. Pålsson, "Conceptual study of a 250 kW planar SOFC system for CHP application," *J. Power Sources*, vol. 131, no. 1, pp. 49–56, May 2004.

[17] P. Thounthong, B. Davat, S. Rael, and P. Sethakul, "Fuel cell high-power applications," *IEEE Ind. Electron. Mag.*, vol. 3, no. 1, pp. 32–46, Mar. 2009.

[18] T. Sarkar and S. K. Mazumder, "Analysis of input current ripple and optimum filter capacitor for fuel-cell-based single-phase inverter," *J. Fuel Cell Sci. Technol.*, vol. 12, no. 6, 2015, Art. no. 061005.

[19] S. K. Pradhan, S. K. Mazumder, J. Hartvigsen, and M. Hollist, "Effects of electrical feedbacks on planar solid oxide fuel cell," *J. Fuel Cell Sci. Technol.*, vol. 4, no. 2, pp. 154–166, 2007.

[20] C. Rakousky *et al.*, "Polymer electrolyte membrane water electrolysis: Restraining degradation in the presence of fluctuating power," *J. Power Sources*, vol. 342, pp. 38–47, 2017.

[21] Z. Dobó and Árpád Bence Palotás, "Impact of the current fluctuation on the efficiency of alkaline water electrolysis," *Int. J. Hydrogen Energy*, vol. 42, no. 9, pp. 5649–5656, Mar. 2017.

[22] J. Solanki, N. Fröhleke, J. Böcker, and P. Wallmeier, "Analysis, design and control of 1 MW, high power factor and high current rectifier system," in *Proc. IEEE Energy Convers. Congress Expo.*, Raleigh, USA, Sep. 2012, pp. 1725–1732.

[23] P. S. Maniscalco, V. Scaini, and W. E. Veerkamp, "Specifying DC chopper systems for electrochemical applications," *IEEE Trans. Ind. Appl.*, vol. 37, no. 3, pp. 941–948, May/Jun. 2001.

[24] J. Solanki, N. Frohleke, J. Bocker, and P. Wallmeier, "Comparison of thyristor-rectifier with hybrid filter and chopper-rectifier for high-power, high-current application," in *Proc. PCIM Europe Conf.*, Nuremburg, Germany, May. 2013, vol. 1, pp. 1391–1398.

[25] J. R. Rodríguez *et al.*, "Large current rectifiers: State of the art and future trends," *IEEE Trans. Ind. Electron.*, vol. 52, no. 3, pp. 738–746, Jun. 2005.

[26] Y. Suh and P. K. Steimer, "Application of IGCT in high-power rectifiers," *IEEE Trans. Ind. Appl.*, vol. 45, no. 5, pp. 1628–1636, Sep. 2009.
[27] AEG Power Solutions, Zwanenburg, The Netherlands. *Thyrobox DC-3 Industrial High-Power DC Power Supply*, 2018. [Online]. Available: https://www.aegps.com/en/products/customized-power-supply-systems/thyrobox-dc3/. Accessed on: May 23, 2018.
[28] J. van der Merwe, K. Uren, G. van Schoor, and D. Bessarabov, "A study of the loss characteristics of a single cell PEM electrolyser for pure hydrogen production," in *Proc. IEEE Int. Conf. Ind. Technol.*, Cape Town, South Africa, Feb. 2013, pp. 668–672.
[29] F. da Costa Lopes and E. H. Watanabe, "Experimental and theoretical development of a PEM electrolyzer model applied to energy storage systems," in *Proc. Brazilian Power Electron. Conf.*, Bonito-Mato Grosso do Sul, Brazil, Sep. 2009, pp. 775–782.
[30] A. Ursúa and P. Sanchis, "Static–dynamic modelling of the electrical behaviour of a commercial advanced alkaline water electrolyser," *Int. J. Hydrogen Energy*, vol. 37, no. 24, pp. 18598–18614, Dec. 2012.
[31] Ø. Ulleberg, "Modeling of advanced alkaline electrolyzers: A system simulation approach," *Int. J. Hydrogen Energy*, vol. 28, no. 1, pp. 21–33, Jan. 2003.

Joonas Koponen was born in Vantaa, Finland, in 1988. He received the B.Sc. degree in electrical power systems from the Lappeenranta University of Technology (LUT), Lappeenranta, Finland, in 2013, and the M.Sc. degree in embedded systems from LUT, and in computer science from the Swinburne University of Technology, Melbourne, Australia, in 2015. He is currently working toward the D.Sc. degree at the Laboratory of Control Engineering and Digital Systems, LUT.

His research interests include the efficiency and control of water electrolysis processes from the viewpoint of power electronics.

Vesa Ruuskanen was born in Imatra, Finland, in 1983. He received the M.Sc. and D.Sc. degrees in electrical engineering from the Lappeenranta University of Technology (LUT), Lappeenranta, Finland, in 2007 and 2011, respectively.

He is currently an Assistant Professor with LUT REFLEX research platform. His research interest includes studying the effect of power quality of water electrolyzers including the *in situ* electrolysis of electrobioreactors used in power-to-food applications.

Antti Kosonen was born in Imatra, Finland, in 1980. He received the M.Sc. and D.Sc. degrees in electrical engineering from the Lappeenranta University of Technology (LUT), Lappeenranta, Finland, in 2005 and 2008, respectively.

He is currently an Associate Professor with the Department of Electrical Engineering, LUT. His research interests include water electrolyzers, Power-to-X systems, solar power, energy efficiency, calorimetric measurement systems, and power line communication.

Markku Niemelä was born in Mäntyharju, Finland, in 1968. He received the B.Sc. degree from the Helsinki Institute of Technology, Helsinki, Finland, in 1990, and the M.Sc. and D.Sc. degrees from the Lappeenranta University of Technology (LUT), Lappeenranta, Finland, in 1995 and 1999, respectively, all in electrical engineering.

He is currently a Senior Researcher with the Carelian Drives and Motor Centre, LUT. His research interests include motion control, control of line converters, and energy efficiency of electric drives.

Jero Ahola was born in Lappeenranta, Finland, in 1974. He received the M.Sc. and D.Sc. degrees in electrical engineering from the Lappeenranta University of Technology (LUT), Lappeenranta, Finland, in 1999 and 2003, respectively.

He is currently a Professor of energy efficiency in electrical systems and proactive maintenance of electrical equipment with the Department of Electrical Engineering, LUT. His research interests include energy efficiency in electrical motor-driven systems, solar photovoltaic systems, Power-to-X, and power line communication in the motor cables of variable speed electric drives.

Publication II

Koponen, J., Ruuskanen, V., Kosonen, A., Niemelä, M., and Ahola, J.
Considering power quality in energy efficiency of alkaline water electrolyzers

20th European Conference on Power Electronics and Applications
EPE '18–ECCE Europe,
Riga, Latvia, Sep. 2018.

Considering power quality in energy efficiency of alkaline water electrolyzers

Joonas Koponen, Vesa Ruuskanen, Antti Kosonen, Markku Niemelä, and Jero Ahola
LAPPEENRANTA UNIVERSITY OF TECHNOLOGY
P.O. BOX 20, 53851
Lappeenranta, Finland
Phone: +358 (50) 563-6569
Email: joonas.k.koponen@lut.fi
URL: http://www.lut.fi

Keywords

≪Power quality≫, ≪Efficiency≫, ≪Renewable energy systems≫.

Abstract

Water electrolysis may become a major application for power electronics, since hydrogen is a key element for energy storage, renewable hydrocarbons, fuels, and chemicals. Electrolyzers require DC power and their operation depends on electric conditioning. Electrolyzers typically operate at relatively low voltages and high currents, which can be challenging for power electronics. This paper studies the efficiency of alkaline water electrolysis and improvement of electrolyzers from the viewpoint of power electronics.

Introduction

Water electrolyzers may be the main electricity consumers in the future as the whole energy sector needs to be based on renewable energy sources [1]. Renewable hydrogen is needed to produce carbon neutral fuels for transportation and seasonal energy storage in the form of chemical energy, as well as raw materials for the chemical industry [2, 3, 4, 5, 6].

The hydrogen production rate (mol/s) of a single electrolytic cell is linearly proportional to the current

$$f_{\mathrm{H_2}} = \eta_{\mathrm{F}} \frac{i_{\mathrm{cell}} A_{\mathrm{cell}}}{zF} = \eta_{\mathrm{F}} \frac{I_{\mathrm{cell}}}{zF}, \tag{1}$$

where z (for hydrogen, $z = 2$) is the number of moles of electrons transferred in the reaction, F the Faraday constant (9.6485×10^4 C/mol), i_{cell} the current density (A/cm^2), A_{cell} the effective cell area (cm^2), I_{cell} the current (A), and η_{F} the Faraday efficiency, also known as the current efficiency, the ratio of actualized hydrogen production rate to the ideal one. Therefore, commercial electrolyzers apply relatively low voltage and high current. As an example of the DC voltage and current levels in MW-scale electrolyzers, the Power-to-Gas plant by ETOGAS in Werlte, Germany, applies three 2 MW alkaline water electrolyzers, whose nominal input voltage is 250 V and current 9000 A [7].

Owing to the requirement for high DC currents, the rectifiers in conventional industrial water electrolyzers are typically based on thyristors and diodes [8]. However, switching according to the line frequency generates harmonics to the supplied current and voltage causing additional heat losses in the water electrolysis process [9, 10]. Application of more modern power electronic converters may be beneficial, but

would require modular conversion structures to share the supplied currents to suitable levels for semiconductors using forced commutation, such as an insulated-gate bipolar transistor (IGBT).

The electrochemical time constants reported in the literature for an alkaline electrolyzer, which is shown to have a longer time constant than PEM electrolyzers, vary from 10 ms to 40 ms [11, 12] to 10 min [13]. Typically, the dynamics is limited by the control to avoid premature degradation of the stack, while the actual response time of the stack is significantly shorter.

In this paper, the energy consumption and efficiency is analyzed by simulation and measurements from a small-scale commercial alkaline water electrolyzer stack. The effect of varying dynamic conditions on the specific energy consumption is assessed. Laboratory measurements are carried out using a commercial 2.8 kW alkaline water electrolyzer.

This paper is organized as follows. Section 2 introduces the basics of the electrochemistry in water electrolysis processes and describes the modelling tools employed to describe alkaline water electrolyzers as simplified electrical loads. The laboratory test setup for the measurement of specific energy consumption of small-scale water electrolyzers is also described. In Section 3, the theoretical effect of AC current ripple on the electrolyzer specific energy consumption is first analyzed. Then, the measurement results are presented. Section 4 concludes the paper.

Research methods

For example, in [14] an alkaline water electrolyzer stack is supplied with a current AC component at the frequency of 1 kHz without a significant phase shift between the voltage and current. Therefore, the current ripple in the alkaline electrolyzer stack current is assumed to cause just a change of the static operating point of the stack. With this assumption, the efficiency of the stack is only affected by the change of the current density due to the current AC ripple. Therefore, the additional losses caused by poor power quality are not dependent on the frequency, but only on the current and voltage waveforms. The effect of power quality on the Faraday efficiency and the effect of AC ripple frequency are excluded from this study. However, it should be noted that a lower current density may have an adverse effect on the Faraday efficiency, and therefore on the specific energy consumption of the hydrogen production system [6, 15].

Experimental data is required to model the selected water electrolysis processes as shown in [10, 16, 17]. The electrolytic cell voltage is a sum of the reversible voltage and additional overvoltages appearing in the electrolytic cell

$$U_{\text{cell}} = U_{\text{rev}} + U_{\text{ohm}} + U_{\text{act}} + U_{\text{con}}, \tag{2}$$

where U_{cell} is the cell voltage, U_{rev} the reversible voltage that is the lowest voltage required for the water decomposition to occur, U_{ohm} the overvoltage caused by ohmic losses in the cell elements, U_{act} the activation overvoltage caused by electrode kinetics, and U_{con} the concentration overvoltage due to mass transport processes [18].

However, in this study a simplified electrical model of the stack is needed for the point by point study of the stack input electrical power. The stack is assumed to operate under constant temperature and pressure. Therefore, the reversible voltage is assumed to be constant and the overpotential caused by the stack current to be linearly dependent on the current amplitude

$$U_{\text{cell}} = U_{\text{rev}} + R i_{\text{cell}} A_{\text{cell}}, \tag{3}$$

where R is the equivalent resistance of the stack. The electrical power of the stack is calculated based on the stack current and voltage as a function of time. The hydrogen production is assumed linearly

dependent on the stack current as shown in (1). The specific energy consumption of the stack with AC ripple is calculated based on the voltage and current waveforms and compared with the stack energy consumption in the case of pure DC supply producing same amount of hydrogen. The energy efficiency of the stack can be calculated by comparing the specific energy consumption for example with the higher heating value (HHV) of hydrogen 39.4 kWh/kg (3.54 kWh/Nm^3).

Alkaline electrolyzer system

A commercial alkaline electrolyzer is used to study the relation of the voltage and current waveforms in an actual electrolyzer stack. The hydrogen production capability of the Baby McPhy electrolyzer, shown in Fig. 1, is 0.4 Nm^3/h (36 g/h) with maximum electrical power consumption of 2.8 kW. The typical DC current and voltage values are 35 A and 65 V.

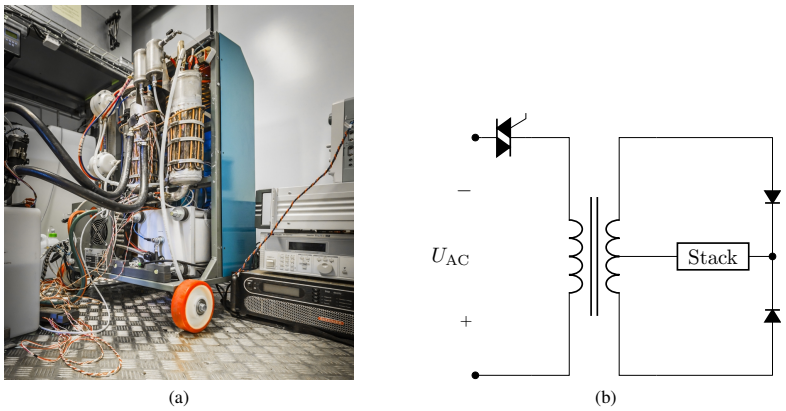

(a) (b)

Fig. 1: Commercial alkaline water electrolyzer used in the study. (a) Baby McPhy alkaline water electrolyzer. (b) Integrated power supply unit.

The commercial power supply consists of a transformer with a diode rectifier at the secondary circuit supplying the stack. The current of the stack is controlled by varying the primary voltage of the transformer with a triac based on the hydrogen pressure and operating temperature.

The voltage and current waveforms of the alkaline electrolyzer with the built-in commercial power supply unit are shown in Fig. 2a. It can be seen that the single phase diode rectification excites high amplitude harmonics with frequencies multiples of 100 Hz. The voltage never reaches zero because of the reversible voltage of the electrolyzer stack, but the current stays at zero almost half of the period. The voltage estimated with a simplified model matches the measured value well when the current differs from zero.

The average values of stack current and stack voltage are 24.8 A and 59.6 V. Nominal hydrogen production rate of the small-scale water electrolyzer is achieved at 35 A DC current level.

The laboratory setup for the specific energy consumption measurements of water electrolyzers is illustrated in Fig. 3. For stack current, stack voltage, and stack power measurements a PX8000 precision power scope (Yokogawa) is used equipped with a Zero-Flux CURACC current measurement system (Hitec). Water content in the produced hydrogen gas is minimized using a hydrogen drying unit (Hydrocell) that includes a 20 L drying column filled with drying agent. Hydrogen gas mass flow is measured after the drying unit with a SLA5860 thermal mass flow meter (Brooks). In order to ensure moisture does not affect the mass flow meter, the dew point of the hydrogen gas is measured with a DMT152 dew point transmitter (Vaisala). The hydrogen gas content in oxygen outlet (vol-%) is monitored using a K1550R thermal conductivity detector (Eaton MTL). The temperature of the alkaline water electrolyzer is measured with multiple PT100 temperature sensors. Stack temperature in Section 3 refers to the temperature of the oxygen gas exiting the stack. An SG Series 30 kW DC power supply (Sorensen) is used

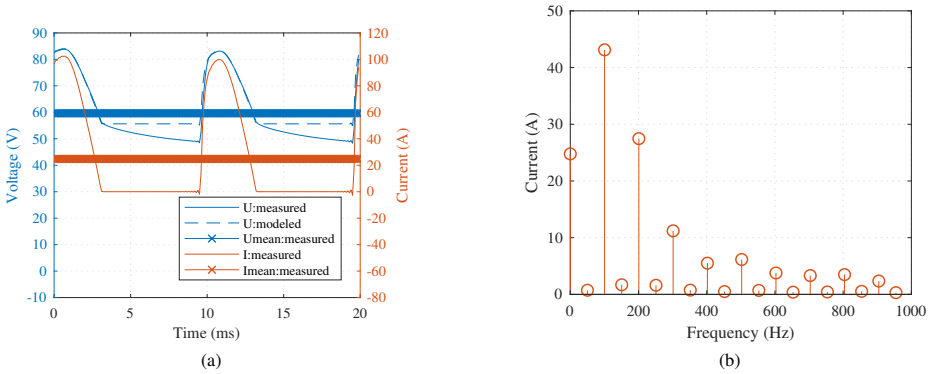

Fig. 2: (a) Voltage and current waveforms of the alkaline electrolyzer with the commercial power supply. (b) Amplitude spectrum of the measured current waveform.

as the separate DC power supply in the specific energy consumption tests to provide a reference for the integrated power supply of the Baby McPhy alkaline water electrolyzer.

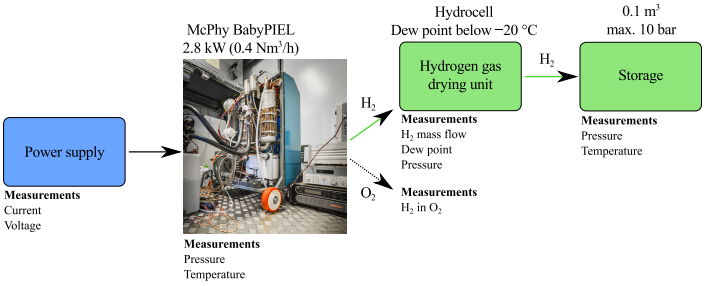

Fig. 3: Description of the laboratory setup for alkaline water electrolyzer tests.

Results

The effect of supply power ripple is studied in two cases. First, the specific energy consumption of the small-scale alkaline stack is analyzed in the case of a sinusoidal current ripple as a function of DC current and the AC ripple amplitude. Then, the alkaline system operation is experimentally verified with two different power supply configurations in the experimental setup described in Section 2. The performance of the small-scale water electrolyzer is also measured as a function of load, when powered by a DC power supply.

Sinusoidal current ripple

To study the theoretical effect of AC current ripple on the specific energy consumption of the alkaline electrolyzer, the stack efficiency is analyzed as a function of DC current and AC ripple amplitude. The AC current ripple amplitude is limited not to exceed the DC current value as seen in Fig. 4. The stack voltage behaviour is simulated according to the simplified model as shown in (3), where the equivalent resistance of the stack is 277 mΩ and the reversible voltage is 55.65 V. As the Faraday efficiency is assumed to unity, the hydrogen production rate in mol/s can be calculated according to (1). Therefore, the stack specific energy consumption in kWh/kg is defined as follows

$$E_s = \frac{496\,\mathrm{mol/kg}}{3.6\,\mathrm{MJ/kWh}} \frac{U_{\mathrm{cell}} i_{\mathrm{cell}} A_{\mathrm{cell}}}{f_{\mathrm{H_2}}}. \tag{4}$$

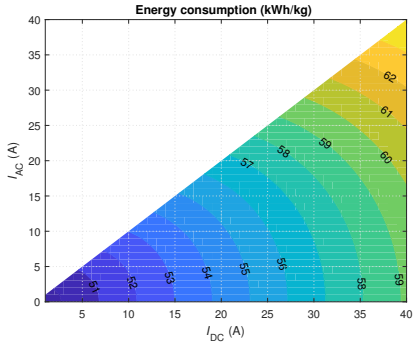

Fig. 4: Specific energy consumption of the small-scale alkaline electrolyzer as a function of DC current and AC ripple (100 Hz) amplitude.

It can be seen that the minimum energy consumption is achieved with pure DC at low current values. Naturally, the DC current value is dominating over the AC ripple in the energy consumption. However, the AC ripple increases the specific energy consumption up to 8%, when Faraday efficiency is assumed as unity, which then represents the ideal case for hydrogen production rate.

Experimental

The performance of the studied water electrolyzer is first analyzed as a function of DC current when powered by a DC power supply. The stack specific energy consumption with the DC power supply is then used as a reference level for the default hydrogen production system configuration.

Water electrolyzer operation with DC power supply

The integrated power supply is disconnected to bypass the embedded control of the default power supply. The measured performance of the Baby McPhy is presented in Table I.

Table I: Measured stack temperature, stack DC current, stack DC voltage, hydrogen gas mass flow, hydrogen content in oxygen outlet, and calculated stack specific energy consumption and higher-heating-value-based stack efficiency as a function of DC current. The water electrolyzer is operated at a balanced pressure of 1 bar. Dew point of the hydrogen gas stayed below −63 °C after the gas drying unit.

Current setpoint (A)	T_{stack} (°C)	I_{DC} (A)	U_{DC} (V)	$f_{\mathrm{H_2}}$ (g/h)	H_2 in O_2 (vol-%)	E_s (kWh/kg)	$\eta_{\mathrm{stack,\,HHV}}$ (%)
35	55.79	35.01	68.06	36.2	0.78	65.9	59.8
30	55.52	30.01	66.45	30.6	0.81	65.1	60.5
25	54.58	25.02	65.05	25.1	0.86	64.9	60.7
20	55.19	20.02	63.11	19.5	0.94	64.6	60.9
15	55.90	15.01	61.12	13.9	1.12	65.8	59.8
10	54.51	10.01	58.96	8.7	1.34	68.1	57.8
5	55.25	5.00	55.24	3.2	1.66	85.5	46.1

The thermal conductivity detector did not register high amounts of hydrogen gas exiting mixed with oxygen. Therefore, the results indicate the low Faraday efficiencies would be due to stray stack currents.

The resulting voltage and Faraday efficiencies of the small-scale alkaline water electrolyzer, based on measurements presented in Table I, are presented in Fig. 5. The voltage efficiency is the ratio of thermoneutral voltage level—in bipolar cell stacks, the number of cells multiplied by 1.48 V—to the real stack voltage level.

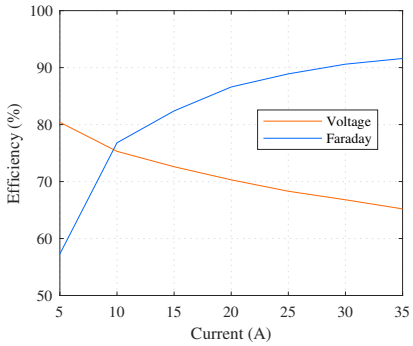

Fig. 5: Measured voltage and Faraday efficiency of the small-scale alkaline water electrolyzer as a function of DC current.

Power supply comparison

The specific energy consumption of the Baby McPhy alkaline water electrolyzer is compared in two different power supply configurations: 1) the integrated power supply unit illustrated in Fig. 1, and 2) a commercial DC power supply. The resulting stack specific energy consumptions are then compared.

Operating the studied commercial alkaline water electrolyzer in its default configuration—in terms of operating temperature and DC current control—is problematic due to the limited cooling capacity of the integrated fans of the electrolyzer enclosure, and the temperature and pressure-based control of the triac in the primary of the transformer. In other words, the commercial electolyzer is not designed for long-term operation in stable conditions; the higher the stack pressure and the stack temperature, the lower the stack DC current level will be. Consequently, the lower the stack DC current, the lower the heat losses, which will result in poorly controlled stack temperature with on/off-controlled enclosure fans. In order to maintain constant temperature conditions, a water cooling system had to be applied. In the new cooling system, the gas separator tanks (one for oxygen gas, one for hydrogen gas) are partially enveloped in copper plating with integrated water circulation. A radiator with a PWM-controlled fan then transfers heat to the surrounding ventilated laboratory space.

To achieve stable stack pressures throughout the tests, a purge valve for the hydrogen gas storage was kept open. Therefore, increased storage pressure would not affect the operating pressure at the stack and cause further changes in water electrolyzer operation. As a drawback of keeping the hydrogen storage purge valve open, the hydrogen production rate could not be verified from the change in storage pressure over time. Nominal operation, where the hydrogen production rate would be 36 g/h, could not be achieved due to the temperature and pressure-based control of the water electrolyzer, when powered by its integrated power supply unit. Stack pressure levels were controlled to 0.3 bar and to 0.1 bar using a back-pressure valve to achieve stable stack DC currents of 10 A and 13 A, respectively, at a stack temperature of 56 °C. The operating conditions were then replicated, when the water electrolyzer was powered by the separate DC power supply. The results from the specific energy consumption tests are presented in Table II. The stack DC current and voltage waveforms created by the integrated power supply solution are presented in Fig. 6.

The stack specific energy consumption is 20.3% higher at 10 A DC current level, and 23.6% higher at 13 A DC current with the integrated power supply unit when compared to the DC power supply. In all cases presented in Table II, the Faraday efficiency η_F stays below 85%, which increases the specific

Table II: Stack specific energy consumption comparison, when powered by the integrated power supply of the Baby McPhy and a separate DC power supply. Measurement results are mean values from a 10 s time period. Dew point of the hydrogen gas stayed below −57 °C after the gas drying unit.

	T_{stack} (°C)	p_{stack} (bar)	I_{DC} (A)	U_{DC} (V)	f_{H_2} (g/h)	E_s (kWh/kg)	η_F (%)
Integrated power supply	56.5	0.31	9.74	51.71	8.9	79.6	81.4
Integrated power supply	56.4	0.11	12.96	53.79	12.2	77.7	83.7
DC power supply	56.1	0.32	10.10	58.29	8.9	66.1	77.9
DC power supply	56.1	0.11	13.14	59.86	12.5	62.8	84.4

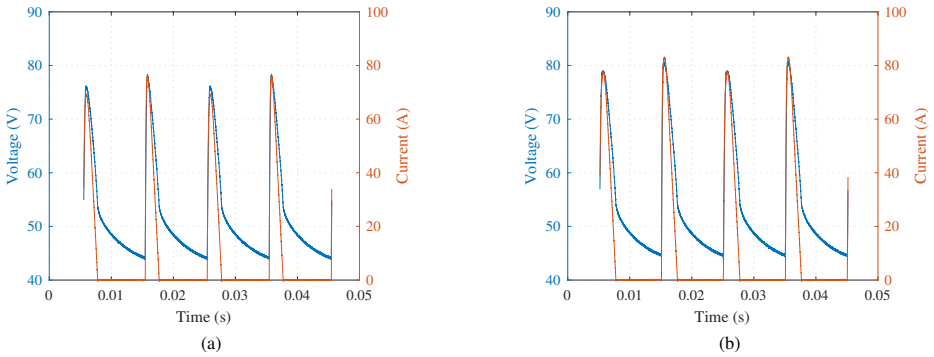

Fig. 6: Voltage and current waveforms of the Baby McPhy integrated power supply at certain DC current levels. (a) 10 A and (b) 13 A.

energy consumptions. No hydrogen gas leaks were detected during the measurements.

Conclusions

The effect of power quality on the specific energy consumption of alkaline water electrolyzers is analyzed via simulation and laboratory measurements. The energy efficiency of a commercial 2.8 kW alkaline water electrolyzer is measured in two different power supply configurations: 1) the default, integrated power supply of the electrolyzer and 2) a commercial DC power supply.

The measurement results show that the DC power supply can offer up to 24% lower stack specific energy consumption when compared to the integrated power supply of the studied water electrolyzer. With the DC power supply, the Faraday efficiency of the small-scale electrolyzer is 57%–92% when the stack DC current is increased, respectively, from 5 A to the nominal 35 A. Further investigations are required to determine the impact of power quality on the Faraday efficiency in comparable conditions. The effect of power quality in industrial-scale electrolyzers and the improvement potential for specific energy consumption and lifetime with more modern power converters should also be studied.

References

[1] P. Schmidt, W. Zittel, W. Weindorf, and T. Raksha, "Renewables in Transport 2050 Empowering a sustainable mobility future with zero Final Report," FVV, Tech. Rep., 2016. [Online]. Available: http://www.lbst.de/news/2016_docs/FVV_H1086_Renewables-in-Transport-2050-Kraftstoffstudie_II.pdf

[2] M. Fasihi, D. Bogdanov, and C. Breyer, "Techno-economic assessment of Power-to-Liquids (PtL) fuels production and global trading based on hybrid PV-wind power plants," in *Proc. 10th Int. Renewable Energy Storage Conf. (IRES '16)*, Düsseldorf, Germany, Mar. 2016.

[3] G. Pleßmann, M. Erdmann, M. Hlusiak, and C. Breyer, "Global energy storage demand for a 100% renewable electricity supply," *Energy Procedia*, vol. 46, pp. 22–31, 2014.

[4] J. Koponen, A. Kosonen, K. Huoman, J. Ahola, T. Ahonen, and V. Ruuskanen, "Specific energy consumption of PEM water electrolysers in atmospheric and pressurised conditions," in *Proc. 18th European Conf. on Power Electron. and Applicat. (EPE '16–ECCE Europe)*, Karlsruhe, Germany, Sep. 2016.
[5] A. Kosonen, J. Koponen, K. Huoman, J. Ahola, V. Ruuskanen, T. Ahonen, and T. Graf, "Optimization strategies of PEM electrolyser as part of solar PV system," in *Proc. 18th European Conf. on Power Electron. and Applicat. (EPE '16–ECCE Europe)*, Karlsruhe, Germany, Sep. 2016.
[6] J. Koponen, A. Kosonen, V. Ruuskanen, K. Huoman, M. Niemelä, and J. Ahola, "Control and energy efficiency of PEM water electrolyzers in renewable energy systems," *Int. J. of Hydrogen Energy*, vol. 42, no. 50, pp. 29 648–29 660, 2017.
[7] Erdgas. [Accessed: 21-Dec-2017]. [Online]. Available: https://www.di-verlag.de/media/content/gwf-GE/gwf_Gas_9_13/gwf-GE_09_2013_fb_Rieke.pdf?xaf26a=7607be2af411325a0ddff83247813f87.
[8] A. Ursúa, P. Sanchis, and L. Marroyo, "Chapter 14 - electric conditioning and efficiency of hydrogen production systems and their integration with renewable energies," in *Renewable Hydrogen Technologies*, L. Gandía, G. Arzamendi, and P. Diéguez, Eds. Amsterdam: Elsevier, 2013, pp. 333–360.
[9] A. Ursúa, L. Marroyo, E. Gubía, L. M. Gandía, P. M. Diéguez, and P. Sanchis, "Influence of the power supply on the energy efficiency of an alkaline water electrolyser," *Int. J. Hydrogen Energy*, vol. 34, no. 8, pp. 3221–3233, May. 2009.
[10] A. Ursúa, I. S. Martín, and P. Sanchis, "Design of a programmable power supply to study the performance of an alkaline electrolyser under different operating conditions," in *2nd IEEE Int. Energy Conf. and Exhibition (ENERGYCON '12)*, Florence, Italy, Sep. 2012, pp. 259–264.
[11] N. Chiesa, M. Korpås, O. E. Kongstein, and A. Ødegård, "Dynamic control of electrolyser for voltage quality enhancement," in *Proc. Int. Conf. on Power System Transients (IPST '11)*, Delft, The Netherlands, Jun. 2011, pp. 1–7.
[12] M. Kiaee, A. Cruden, D. Infield, and P. Chladek, "Utilisation of alkaline electrolysers to improve power system frequency stability with a high penetration of wind power," *IET Ren. Power Gen.*, vol. 8, no. 5, pp. 529–536, Jul. 2014.
[13] C. Mansilla, S. Dautremont, B. S. Tehrani, G. Cotin, S. Avril, and E. Burkhalter, "Reducing the hydrogen production cost by operating alkaline electrolysis as a discontinuous process in the french market context," *Int. J. Hydrogen Energy*, vol. 36, no. 11, pp. 6407–6413, Jun. 2011.
[14] V. Ruuskanen, J. Koponen, T. Sillanpää, A. Kosonen, M. Niemelä, and J. Ahola, "Considering the power quality in the power-hardware-in-loop simulation of the water electrolyzers," in *Proc. 19th European Conf. on Power Electron. and Applicat. (EPE '17–ECCE Europe)*, Warsaw, Poland, Sep. 2017, pp. 1–10.
[15] Ø. Ulleberg, "Modeling of advanced alkaline electrolyzers: a system simulation approach," *Int. J. Hydrogen Energy*, vol. 28, no. 1, pp. 21–33, Jan. 2003.
[16] J. van der Merwe, K. Uren, G. van Schoor, and D. Bessarabov, "A study of the loss characteristics of a single cell PEM electrolyser for pure hydrogen production," in *Proc. IEEE Int. Conf. Ind. Technol. (ICIT '13)*, Feb. 2013, pp. 668–672.
[17] F. da Costa Lopes and E. H. Watanabe, "Experimental and theoretical development of a PEM electrolyzer model applied to energy storage systems," in *Proc. Brazilian Power Electron. Conf. (COBEP '09)*, Sep. 2009, pp. 775–782.
[18] A. Ursúa and P. Sanchis, "Static–dynamic modelling of the electrical behaviour of a commercial advanced alkaline water electrolyser," *Int. J. Hydrogen Energy*, vol. 37, no. 24, pp. 18 598–18 614, 2012. [Online]. Available: http://www.sciencedirect.com/science/article/pii/S036031991202191X

Publication III

Koponen, J., Kosonen, A., Ruuskanen, V., Huoman, K., Niemelä, M., and Ahola, J.

Control and energy efficiency of PEM water electrolyzers in renewable energy systems

International Journal of Hydrogen Energy,
vol. 42, no. 50, Dec. 2017.

INTERNATIONAL JOURNAL OF HYDROGEN ENERGY 42 (2017) 29648–29660

Available online at www.sciencedirect.com

ScienceDirect

journal homepage: www.elsevier.com/locate/he

Control and energy efficiency of PEM water electrolyzers in renewable energy systems

Joonas Koponen [a,*], *Antti Kosonen* [a], *Vesa Ruuskanen* [a], *Kimmo Huoman* [b], *Markku Niemelä* [a], *Jero Ahola* [a]

[a] *Lappeenranta University of Technology, P.O. Box 20, FI-53851, Lappeenranta, Finland*
[b] *GreenEnergy Finland Oy, Laserkatu 6, FI-53850, Lappeenranta, Finland*

ARTICLE INFO

Article history:
Received 15 August 2017
Received in revised form
2 October 2017
Accepted 10 October 2017
Available online 31 October 2017

Keywords:
PEM electrolyzer
Photovoltaic system
Energy storage
Efficiency
Optimization

ABSTRACT

The practical dynamic properties and operational limitations of a commercial differential pressure 1 Nm^3h^{-1} proton exchange membrane (PEM) water electrolyzer are studied from the viewpoint of renewable power production. Measured values from a 5 kW_p solar photovoltaic (PV) power plant and PEM electrolyzer are analyzed to study factors affecting the control of PEM water electrolyzers operating as a part of renewable power production systems. Specific energy consumption of the PEM stack as a function of stack hydrogen outlet pressure is estimated based on measured values from two different measurement systems. Electrical energy consumption of the stack does not show any notable increase as the hydrogen outlet pressure is increased from 2.0 MPa to 4.0 MPa. However, the stack specific energy consumption increases by a maximum of 0.2 kWh/Nm^3 when hydrogen outlet pressure is increased from 2.0 MPa to 4.0 MPa. The increase in specific energy consumption at high differential pressure operation is due to a decrease in Faraday efficiency. Selection and control of the hydrogen outlet pressure can minimize the specific energy consumption and maximize the real hydrogen production in dynamic PEM water electrolyzer operation.

Introduction

In order to reach a net zero-emission society, the whole energy system—including electricity, transportation, and direct industrial fuel use—has to be restructured, re-carbonized by electrifying the whole energy system either directly or indirectly. A change of this nature would require practically CO_2-free power generation and the energy system would thus be based predominantly on wind and solar power [1]. To achieve the carbon emission reduction targets set for 2050, bridges between different energy forms and connections between different areas of energy systems are needed, as are efficient means of energy storage. An emerging concept for indirect electrification of energy use called Power-to-Gas, or more generically Power-to-X, approaches the challenges of the future energy system by creating bidirectional interconnections between existing electricity and gas grids, allowing seasonal storage of renewable energy and enabling the production of renewable fuels, raw materials, and chemicals [2]. Consequently, electricity could be regarded as the main form of energy.

* *Corresponding author.*
E-mail address: joonas.k.koponen@lut.fi (J. Koponen).
https://doi.org/10.1016/j.ijhydene.2017.10.056

A key element in the Power-to-X concept, and the first possible end-product, is hydrogen, which together with carbon dioxide can link the electrical and gas grids, and production of hydrocarbons or other industrial chemicals such as ammonia [3]. Hydrogen is the most common element in existence, but on Earth it mostly exists in compound forms such as water. Therefore, hydrogen must be produced, and water is a necessity for all the main hydrogen production pathways from renewable energy sources [4]. Combination of hydrogen production by water electrolysis and renewable power production is attracting interest due to the sustainability and flexibility of the resulting energy system. It has been initially estimated that for Finland, for example, water electrolyzers would have a remarkable role in such an energy scenario [5]. According to these simulations, water electrolyzers would double electricity consumption, and the electrolyzers would consume about 80 TWh by 2050. In the Power-to-Gas concept electricity goes through power electronics both in the production and consumption sides, and the amount of electricity generated will have to be radically increased. Grid-connected water electrolyzers can also contribute to grid services, such as inertia and frequency control, by executing controlled power consumption [3,6].

PEM water electrolysis has gained interest due to its compact system design, reportedly superior dynamic operation capability [3,7,8], and high voltage efficiency at greater current densities compared to traditional alkaline technology. The high cost of components and typically inferior lifetime have been the main factors limiting the emergence of PEM technology [9], although improved stack power density and high efficiency have moved the technology into the MW-scale [10–12]. The compact character of electrolysis modules and the structural properties of the membrane electrode assemblies (MEA) allow high operating pressures and give PEM electrolyzers the ability to endure pressure differences between the electrode compartments in the order of magnitude of 5×10^6. The structural properties of the PEM stack enables the direct production of pressurized hydrogen gas by electrochemical compression and eliminates the need to handle high-pressure oxygen [13]. Direct production of high-pressure hydrogen can be beneficial, since the volumetric energy density of hydrogen gas is low, and the main synthetization routes for hydrogen and carbon di- or monoxide, such as chemical methanation or the Fischer-Tropsch process, operate at elevated pressures.

A commercial alkaline water electrolyzer with solar and wind power systems has been studied based on measured weather data to analyze the resulting energy balance of the system after integration [14]. This work addressed limitations as regards start-stop-cycles of the alkaline electrolyzer in intermittent and dynamic operation. Small-scale PEM water electrolyzers as a part of renewable power production systems have been studied both experimentally [6,15,16], with 10 min and 2 min sampling time solar power data, and analytically based on modeling tools, for example, in Refs. [17,18]. The integration of PEM water electrolyzers into renewable power production systems has also been discussed in terms of restraining the cell degradation rate under fluctuating power, however, still limited to a smallest time scale of 10 min in power supply fluctuation [19]. The effect of differential pressure operation on the gas crossover, and therefore on Faraday efficiency, in PEM water electrolysis has been studied by simulation tools in Ref. [20] and experimentally in Ref. [21].

In this paper, a 1 Nm^3h^{-1} commercial PEM water electrolyzer is studied as integrated into a complete hydrogen setup. Measurements from an existing solar PV power plant at 1 s sampling time are used to analyze the dynamic operation capabilities and limitations of the studied commercial PEM electrolyzer system. The effect of the hydrogen outlet pressure on the electrical energy consumption, specific energy consumption, and controllability are also studied. Control optimization strategies are researched from renewable power production and PEM water electrolyzer performance point of views. This study aims to improve the understanding on how to minimize the specific energy consumption of PEM water electrolyzers and how the stack operating pressure can be selected to maximize the actual hydrogen gas production operating in a real environment. The findings reported in this paper are based on extension and reanalysis of work initially published in Refs. [22,23]. The specific energy consumption tests presented in Ref. [22], where increased hydrogen outlet pressure resulted in no notable increase in stack specific energy consumption, are repeated with different voltage, current and pressure sensors. The effect of pressure on cell voltage in PEM water electrolysis has been recently studied also in Ref. [24], where differential pressure operation followed ideal isothermal compression behavior, but balanced pressure operation showed only minor influence on the cell voltage. The experimental studies on PEM electrolysis integrated into a solar PV system reported in Ref. [23] are expanded in terms of testing period length and variability in the solar PV power reference.

The rest of this paper is organized as follows. The laboratory setup for hydrogen production and use, as well as the solar PV test plant, are introduced in Section Description of the laboratory test system. The fundamentals of PEM water electrolysis and state-of-the-art specifications of PEM water electrolyzers are presented in Section PEM water electrolysis. Section Specific energy consumption of hydrogen production discusses the specific energy consumption of the studied PEM water electrolyzer as a function of the hydrogen outlet pressure. Specific energy consumption measurements of a commercial small-scale PEM water electrolyzer at different stack hydrogen outlet pressures are presented. Section PEM water electrolyzer as a controllable load presents an analysis of dynamic operation capabilities of the studied PEM water electrolyzer. The dynamic operation capabilities of the studied PEM water electrolyzer are assessed against the variability of solar PV power production in Section PEM water electrolyzer as a part of solar PV system. Section Conclusion concludes the paper.

Description of the laboratory test system

Hydrogen laboratory setup

A hydrogen laboratory system manufactured by IRD Fuel Cells (currently known as EWII Fuel Cells) is a part of the campus environment at Lappeenranta University of Technology (LUT).

The hydrogen laboratory setup is built in a standard shipping container. The hydrogen production process in the laboratory setup is the following: Inlet water, which is tap water from the local water network, to the electrolyzer is first deionized to decrease the conductivity of the water. The commercial PEM water electrolyzer E1050 (IRD), which is illustrated in Fig. 1 and presented according to its technical specifications in Table 1, then decomposes the water into hydrogen and oxygen (see Fig. 2). The water electrolyzer is powered by two PAP3200 DC power supplies (Powerfinn) connected in parallel. The dew point of the outlet hydrogen gas is then decreased in a hydrogen gas drying unit (IRD) to −70 °C to prepare it for outdoor storage in Nordic conditions. The total volume of the pressurized hydrogen gas storage is 0.7 m^3. Both the hydrogen and oxygen gas outlet pressures are controlled by back-pressure valves. The designed pressure levels of the E1050 electrolyzer for hydrogen and oxygen gases are 5.0 MPa and 0.2 MPa, respectively. The produced hydrogen can be converted back to DC power in a separate PEM fuel cell and subsequently to grid AC by a commercial solar PV inverter integrated into the fuel cell enclosure.

Operating temperature, water inlet pressure, water conductivity and flow, hydrogen outlet pressure, stack voltage, stack current and individual cell voltages are measured by the IRD's measurement system. An additional data acquisition system was added to support the existing monitoring system. The PEM stack voltage is measured using a NI 9242 250 V_{RMS} analog input module (National Instruments) and the stack current measured using a DHR 100 C420 current transducer (LEM) and a NI 9203 ± 20 mA analog input module. A CompactDAQ-NI9174 chassis is connected to a measurement PC running LabVIEW to collect data from the two analog input modules and the IRD measurement system. The mass flow of produced hydrogen is estimated by measuring the pressure of the hydrogen storage using a PBMN range 0 MPa–6.0 MPa pressure sensor (Baumer) and storage temperature using a thermoresistance PT100 and K120RTD converter (Seneca), and then using the known volume of the hydrogen storage.

Fig. 1 – Water cooled E1050 differential pressure PEM water electrolyzer used in the experimental work.

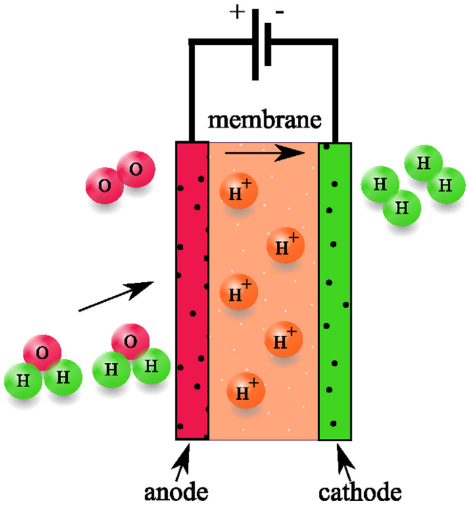

Fig. 2 – Operating principle of a PEM water electrolyzer.

Solar PV power plant

The LUT campus environment includes a 206.5 kW_p solar power plant. Data on the solar PV power is available in real time through a measurement network. Measurements are carried out with a network analyzer, and solar PV data is collected with 1 s sampling time. The hydrogen laboratory setup receives data from the solar PV plant in real time through the measurement network. The hydrogen system is connected to the electricity grid, but it can be virtually operated as an off-grid system. Hence, both on- and off-grid system operation tests can be carried out. For the experimental work in this study, a small section of the solar PV plant is used: the 5 kW_p test plant includes 22 polysilicon panels facing south with a 15° slope angle, a 4.6 kW string inverter, and a network analyzer with Modbus TCP connection [25].

Table 1 – Technical characteristics of the E1050 PEM water electrolyzer.

Hydrogen production rate	0.97 Nm^3h^{-1}
Nominal stack power	4.5 kW
Nominal voltage	64 V
Nominal current	70 A
Operating temperature	70 °C
Number of cells in series	33
Cell cross-sectional area	69 cm^2
Hydrogen pressure	1.50 MPa–5.00 MPa
Oxygen pressure	0.15 MPa–0.25 MPa

PEM water electrolysis

In water electrolysis, electrical and thermal energy are converted into chemical energy, which is stored as hydrogen, and oxygen is produced as a byproduct. According to Faraday's laws of electrolysis, the production of hydrogen is directly proportional to the electric charge transferred at the electrodes. The hydrogen production rate ($mols^{-1}$) of an electrolytic cell can be expressed as

$$f_{H_2} = \eta_F \frac{i_{cell} A_{cell}}{zF}, \quad (1)$$

where z is the number of moles of electrons transferred in the reaction (for hydrogen, z = 2), F the Faraday constant (9.6485×10^4 C mol^{-1}), i_{cell} the current density (A cm^{-2}), A_{cell} the effective cell area (cm^2), and η_F the Faraday efficiency, also known as the current efficiency. The energy required for the reaction to take place is the enthalpy of formation of water, ΔH. Only the free energy of this reaction, i.e. the Gibbs free energy change, ΔG, has to be supplied to the electrodes in the form of electrical energy. This lowest voltage required for the water decomposition to occur is called the reversible voltage U_{rev}. Without auxiliary heat, the minimum voltage required is higher than the reversible voltage, i.e. the thermoneutral voltage level U_{tn} [13,26]. The reversible voltage and thermoneutral voltage at standard ambient conditions are 1.23 V and 1.48 V, respectively, which correspond to $\Delta G = 237.21$ kJ mol^{-1} and $\Delta H = 258.84$ kJ mol^{-1}.

The electrolytic cell voltage is a sum of the reversible voltage and additional overvoltages appearing in the electrolytic cell.

$$U_{cell} = U_{rev} + U_{ohm} + U_{act} + U_{con}, \quad (2)$$

where U_{cell} is the cell voltage, U_{ohm} the overvoltage caused by ohmic losses in the cell elements, U_{act} the activation overvoltage caused by electrode kinetics, and U_{con} the concentration overvoltage due to mass transport processes [13]. In the literature, it has been stated that the concentration overvoltage is only significant at very high current densities, and hence U_{con} would be negligible for commercial PEM water electrolyzers [27].

Commercial PEM electrolyzers typically operate at current densities of 0.6 A cm^{-2}–2.0 A cm^{-2} and at operating temperatures of 50 °C–80 °C [7]. The compact character of electrolysis modules and the structural properties of the MEAs allow high operating pressures and give PEM electrolyzers the ability to endure great pressure differences between the electrode compartments. In the case of the E1050, the cathode compartment pressure is higher by a factor of 25. This differential pressure can then be utilized to optimize the specific energy consumption of PEM electrolyzer systems and their total capital cost: Water network pressure is sufficient for the water inlet on the anode side, while electrochemical compression enables direct production of high pressure hydrogen gas. However, the minimum electrolyzer stack current is limited by the hydrogen gas crossover rate when hydrogen outlet pressure is increased [20].

Hydrogen gas compression

In water electrolysis, the reversible voltage is a thermodynamic state function dependent on the operating temperature and pressure [28]. For PEM water electrolysis, the open circuit voltage can be written using the Nernst equation [29].

$$U_{rev} = U^0_{rev} + \frac{RT}{zF} \ln\left(\frac{p_{H_2} \cdot p_{O_2}^{1/2}}{p_{H_2O}}\right), \quad (3)$$

where U^0_{rev} is the reversible cell voltage, R is the universal gas constant (8.314 J $mol^{-1}K^{-1}$, T is the operating temperature (K), p_{H_2} is the partial pressure of hydrogen (Pa), p_{O_2} is the partial pressure of oxygen (Pa), and p_{H_2O} is the saturated vapor pressure of water (Pa). The reversible cell voltage is defined as a function of temperature as shown in Refs. [30,31].

$$U^0_{rev} = 1.229 - 0.9 \times 10^{-3}(T - 298). \quad (4)$$

The open circuit voltage as a function of the cathode compartment pressure is presented in Fig. 3 for anode compartment pressure of 0.2 MPa. At 70 °C, as the cathode compartment pressure increases from 0.2 MPa to 5.0 MPa, the open circuit voltage increases from 1.302 V to 1.352 V, i.e. by 4%. Assuming that the anode compartment pressure were lowered to 0.1 MPa, the open circuit voltage increase according to Eq. (3) would be 5%, if the cathode compartment pressure is set in the range 0.1 MPa–5.0 MPa.

Ideal isothermal hydrogen compression at 70 °C from 0.1 MPa to 5.0 MPa would require 0.14 kWh/Nm^3 of energy. As a comparison, the higher heating value of hydrogen is 3.54 kWh/Nm^3, which is typically used to calculate the efficiency of a water electrolyzer [13]. A specific energy consumption increase of 0.14 kWh/Nm^3 corresponds to 4% increase compared to the higher heating value of hydrogen.

The amount of hydrogen gas stored under pressure can be estimated using the van der Waals equation [32].

$$p = \frac{nRT}{V - nb} - a\frac{n^2}{V^2} \quad (5)$$

where p is pressure of the hydrogen gas (Pa), n the amount of substance (mol), T the temperature (K), and V the volume of storage (m^3). The constants a and b are called the van der Waals coefficients, which for hydrogen are 2.45×10^{-2} Pa $m^6 mol^{-2}$ and 26.61×10^{-6} $m^3 mol^{-1}$, respectively.

Key performance indicators of PEM water electrolyzers

Efficiency, lifetime, capital and operational costs, and the desired operating conditions are key factors for performance analysis of a water electrolyzer system. The efficiency of a PEM electrolyzer is limited by overvoltages appearing in the individual cells, parasitic currents, and inefficiencies in the stack and system design, such as hydrogen gas crossover into the anode compartment or lost hydrogen in post-electrolysis gas conditioning.

Electrolytic cell degradation is caused by aging of the cell and the resulting increase in resistance. Three main degradation phenomena have been noted [33]: 1) passivation of Ti-

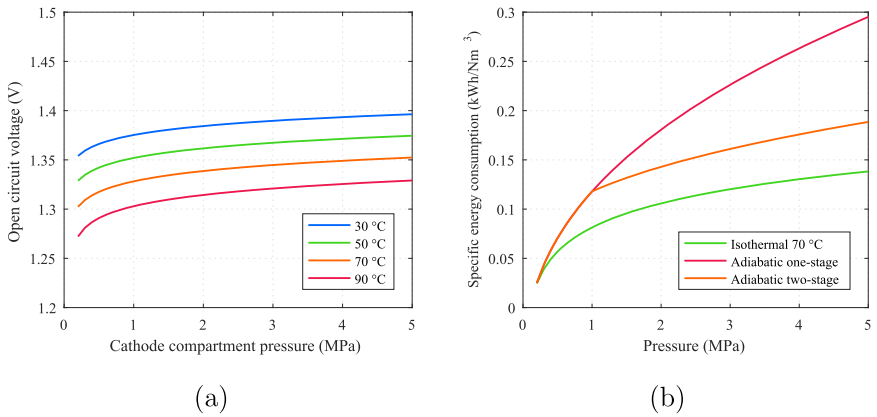

Fig. 3 – Energy consumption in hydrogen compression. (a) Open circuit voltage of a differential pressure PEM water electrolyzer as a function of the cathode compartment pressure according to Eq. (4). The anode compartment pressure is set to 0.2 MPa. (b) Ideal post-electrolysis isothermal, one-stage adiabatic, and two-stage adiabatic with cooling to 30 °C at 1.0 MPa compression.

based components on the anode side, 2) deactivation of electrolyte and electrode performance due to impurities in the electrolyzer inlet water, and 3) structural changes to the catalyst material. The overall aging effects can be referred to as the voltage degradation rate ($\mu V\,h^{-1}$). This voltage increase as a function of time is directly relevant to the lifetime and efficiency of the electrolyzer stack and results in reduced efficiency over the stack lifetime. The MEAs first undergo a break-in period, where the initial voltage degradation is faster, before reaching stable performance under continuous operation [34]. For cells operated continuously for long periods of time, a rapid degradation caused by internal short circuiting through a physically damaged membrane has been observed [35]. State-of-the-art PEM water electrolyzers have been reported to have a voltage degradation rate below 14 $\mu V\,h^{-1}$ [7], but the values for voltage degradation are generally presented for systems under continuous and steady-state operation [8]. Data and studies are limited on how an electrolytic cell and its components age and degrade if the reference operation mode is discontinuous or under variable load. A "surprisingly significant" stack efficiency decrease from 75% to 65% in 941 h of operation directly coupled to a solar PV array was reported in Ref. [6]—no conclusions, however, could be drawn to establish the extent to which the highly dynamic operation affected the degradation rate observed in this particular case. Further research is required to understand the cell degradation mechanisms and the effect of rapid changes in electrolyzer stack power on the stack lifetime.

Table 2 – Key dynamic operation characteristics of typical PEM water electrolyzers [2,7,8].

Operating temperature	50 °C–80 °C
Hydrogen outlet pressure	<20 MPa
Current density	0.6 A cm^{-2}–2.0 A cm^{-2}
Min. load of nominal	5%–10%
Overload of nominal	<200%
Ramp-up from min. load to nominal	10% s^{-1}–100% s^{-1}
Cold start to min. load	5 min–15 min

Typically, PEM water electrolysis technology is characterized by a wider control range, faster response time to changes in input power, greater stack power density and more efficient operation, albeit with inferior stack lifetime compared to alkaline technology [2,3,7,8]. Key characteristics most relevant to the dynamics of PEM water electrolyzers are presented in Table 2. The operating temperature in PEM electrolyzers is typically limited to below 80 °C, when conventional Nafion® membranes are used. Higher temperatures could lead to improvements in energy efficiency according to the thermodynamic state functions of the electrolytic cell open circuit voltage, Eqs. (3) and (4). The compact stack design and high power density due to the lack of liquid electrolyte enables relatively quick cold start capabilities, since the total mass to be heated to the operating temperature is smaller than with alkaline technology.

The minimum stack current has been reported to be even below 5% of nominal value for some commercial PEM water electrolyzer models [36,37]. However, increasing the hydrogen outlet pressure increases the gas crossover of hydrogen into oxygen—a phenomenon more severe at low current densities [20]. Increasing the hydrogen outlet pressure is attractive in order to increase the volumetric energy density of hydrogen gas and the energy storage capabilities of a hydrogen production system without separate post-electrolysis compressors. The flammability limit for hydrogen in air in ambient conditions is 4%–75% volume fraction [38]. The lower flammability limit should thus be the first factor in PEM stack and system design, when partial load operation is considered in renewable energy systems.

Results and discussion

Specific energy consumption of hydrogen production

To study the effect of the hydrogen outlet pressure on the specific energy consumption of a commercial PEM water electrolyzer stack, tests were run at hydrogen outlet pressures of 2.0 MPa, 3.0 MPa, and 4.0 MPa at nominal stack current of 70 A, and current density of 1.01 $A\,cm^{-2}$. The minimum hydrogen outlet pressure 2.0 MPa was selected based on the structure of the PEM stack and the operation of the post-electrolysis hydrogen gas drying unit. The maximum hydrogen outlet pressure 4.0 MPa was selected to ensure uninterrupted safe operation of the PEM electrolysis unit. In the filling tests, the hydrogen storage ($V = 0.7\,m^3$) is filled progressively from 1.0 MPa to 1.8 MPa, then from 2.0 MPa to 2.8 MPa, and finally from 3.0 MPa to 3.8 MPa on consecutive days. To account for uncertainties, a total of five filling test campaigns, which are described in Table 3, were run. The water electrolyzer was shut down between each filling run and operated until nominal operating temperature of 70 °C is reached before starting a filling test. For all the test runs, the electrolyzer water inlet pressure was restricted to 0.2 MPa. The mean stack temperature was controlled to 71 °C for all test runs. The inlet water to the electrolyzer was purified and deionized, which results in mean inlet water conductivities during the filling tests in the range of 1.39 $\mu S\,cm^{-1}$–2.56 $\mu S\,cm^{-1}$. The results of the specific energy consumption tests are presented in Fig. 4.

The open circuit voltage of a PEM water electrolyzer is expected to increase as a function of pressure according to the Nernst equation Eq. (3). The corresponding increase in open circuit voltage for the 33-cell stack would be 0.33 V. The observed mean stack voltages during the filling tests, Fig. 4(a), indicate only a slight increase, if any, in stack voltages for both the cell voltage monitoring system (IRD) and the NI 9242 analog input module (cDAQ). Maximum difference in specific energy consumption $E_{s,el}$ in Table 3, which is calculated using only electrical quantities and assuming Faraday efficiency as unity, is 0.01 kWh/Nm^3 between operating at stack hydrogen outlet pressure of 2.0 MPa and 4.0 MPa. According to Suermann et al. [24] differential pressure operation would correspond to isothermal compression behavior in terms of cell voltage increase. When specific energy consumption increases are compared, ideal isothermal compression at 70 °C of hydrogen gas from 2.0 MPa to 4.0 MPa would require 0.025 kWh/Nm^3 more energy. The observed specific energy consumption increase presented in Table 3 stays below the expected isothermal compression behavior.

When the specific energy consumption calculation is extended to include an estimate for the Faraday efficiency, the difference in specific consumption $E_{s,tot}$ is more notable. $E_{s,tot}$, which is calculated using the change in storage pressure to estimate the real hydrogen production rate, increases by a maximum of 0.2 kWh/Nm^3 when hydrogen outlet pressure is increased from 2.0 MPa to 4.0 MPa. The results in Table 3 indicate that an increase in stack hydrogen outlet pressure does not require notably more electrical energy. However, the specific energy consumption of the water electrolyzer is effectively increased due to inferior Faraday efficiency, since the hydrogen output to the hydrogen tubing is decreased. Higher hydrogen outlet pressure, especially in differential pressure operation, has been accounted to increase the hydrogen gas crossover into the anode compartment [20]. In Fig. 4(d), the Faraday efficiency is at its lowest 95% at cathode compartment pressure of 4.0 MPa. Ito et al. [21] observed Faraday efficiencies approaching 99% at current density of 1.0 $A\,cm^{-2}$, however, using a maximum cathode compartment pressure of only 1.0 MPa. Grigoriev et al. [39] extended the studied cathode compartment pressure up to 13 MPa and observed a similar decreasing trend in Faraday efficiency as illustrated in Fig. 4(d): Measured at 0.5 $A\,cm^{-2}$ current density, the reported Faraday efficiency reached a minimum of 90% at 13 MPa balanced operating pressure.

Due to the observed decrease in Faraday efficiency at higher differential pressures, the hydrogen stack outlet

Table 3 – Schedule of the filling tests and the resulting specific energy consumption E_s measured by the IRD and compact DAQ system. $E_{s,el}$ is calculated based on the electrical quantities, while $E_{s,tot}$ includes the estimation on the Faraday efficiency.

Date	Δp	$E_{s,el}$ (IRD)	$E_{s,tot}$ (IRD)	$E_{s,el}$ (cDAQ)	$E_{s,tot}$ (cDAQ)	$\eta_{HHV,tot}$ (IRD)	$\eta_{HHV,tot}$ (cDAQ)
	MPa	kWh/Nm^3	kWh/Nm^3	kWh/Nm^3	kWh/Nm^3	%	%
25.10.2016	1.0–1.8	4.41	4.45	4.38	4.39	79.6	80.7
26.10.2016	2.0–2.8	4.41	4.53	4.38	4.48	78.1	79.1
27.10.2016	3.0–3.8	4.41	4.65	4.38	4.60	76.1	77.0
01.11.2016	1.0–1.8	4.40	4.43	4.36	4.38	80.0	80.9
02.11.2016	2.0–2.8	4.40	4.46	4.37	4.42	79.3	80.2
03.11.2016	3.0–3.8	4.41	4.58	4.37	4.53	77.3	78.1
05.04.2017	1.0–1.8	4.39	4.40	4.36	4.37	80.4	81.0
06.04.2017	2.0–2.8	4.39	4.42	4.36	4.38	80.1	80.7
07.04.2017	3.0–3.8	4.40	4.41	4.36	4.38	80.2	80.9
10.04.2017	1.0–1.8	4.38	4.37	4.35	4.35	80.9	81.4
11.04.2017	2.0–2.8	4.39	4.42	4.35	4.39	80.1	80.7
12.04.2017	3.0–3.8	4.39	4.43	4.36	4.40	79.9	80.4
19.04.2017	1.0–1.8	4.38	4.34	4.35	4.32	81.5	81.9
20.04.2017	2.0–2.8	4.39	4.37	4.35	4.35	81.0	81.5
21.04.2017	3.0–3.8	4.39	4.49	4.36	4.47	78.8	79.2

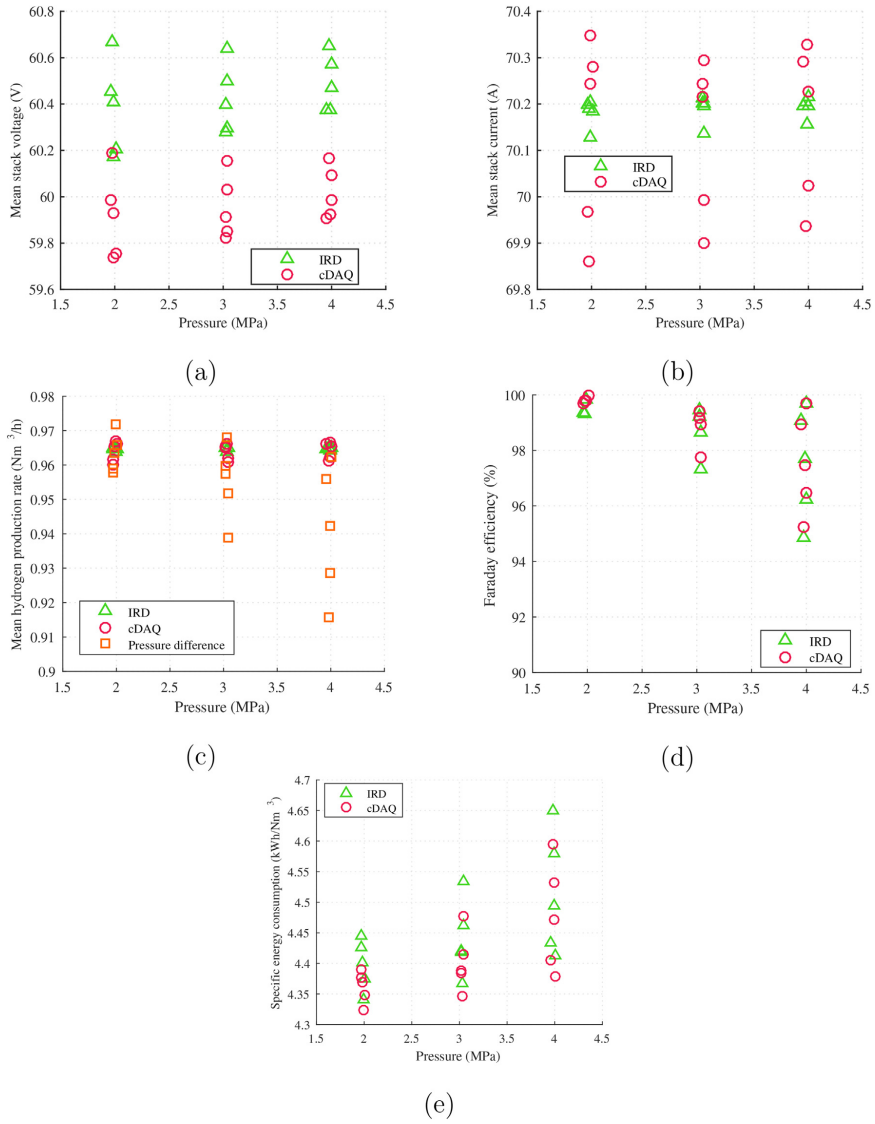

Fig. 4 – Results from the filling tests. (a) Mean stack voltages. (b) Mean stack currents. (c) Calculated hydrogen gas production rates: based on stack current (IRD and cDAQ measurements) and based on the change in storage pressure and temperature. (d) Resulting Faraday efficiencies. (e) Resulting specific energy consumptions when Faraday efficiency is included.

pressure should be controllable in order to minimize the outlet pressure close to the storage pressure. Based on the specific energy consumption tests, minimizing the differential pressure between the anode and cathode compartment to follow the gas storage pressure would optimize the specific energy consumption by maximizing the real hydrogen production rate during a hydrogen gas storage filling process. By contrast, a constant hydrogen stack outlet pressure, which is

selected to cover the highest gas storage pressure in a storage filling process, would continuously lose more hydrogen gas due to hydrogen gas crossover.

PEM water electrolyzer as a controllable load

The lower flammability limit of 4% of hydrogen gas must not be exceeded in order to ensure safe operating conditions, and therefore the minimum water electrolyzer stack current is limited by the adverse gas crossover of hydrogen into the anode compartment. Additionally, the specific energy consumption of an electrolytic hydrogen production process would then be effectively increased as the Faraday efficiency decreases due to hydrogen gas leakage. The E1050 PEM electrolyzer is designed to operate at hydrogen pressure of 5.0 MPa, and during operation the stack current should always target its nominal setpoint: 70 A for an effective cell area of 69 cm^2. At hydrogen outlet pressure of 2.0 MPa, the minimum safe stack current density for this particular stack and system design is 0.25 A cm^{-2}. The controllability of the stack current improves as the hydrogen outlet pressure is decreased.

In addition to the current control range, the performance of a water electrolyzer can also be evaluated based on its capability to perform a cold start. On average, the studied PEM water electrolyzer reaches its nominal stack current in 30 min upon a cold start where the initial stack temperature is 20 °C. In addition, the system start procedure is delayed by the warm-up of the hydrogen drying unit, circulation of deionized inlet water for the stack, performance of a hydrogen flush, and building of oxygen and hydrogen stack pressures. In total, these system preparations take 8–10 min [23]. Thus, the cold start time to the nominal current takes a total 40 min. A typical cold start time, defined as the time to reach the minimum stack load in Table 2, of 15 min can be achieved with the studied PEM electrolyzer. However, the start-up time to the nominal current setpoint would arguably better describe the dynamic capabilities, since the stack should be warmed close to its optimal operating temperature before proceeding to control the stack.

The stack current is limited by the controlling software by two different means: 1) a general parameter for the current slew rate (A s^{-1}); and 2) a maximum allowable cell voltage level of 2 V to reduce corrosion. The ramp-up and ramp-down responses—between the minimum and nominal stack currents at hydrogen pressure of 2.0 MPa— of the E1050 electrolyzer are presented in Fig. 5, where the designated operating temperature has already been reached. The nominal stack current 70 A is reached in 174 s, and during that time, the power increases from 857 W–4234 W. From the nominal stack current, the minimum current setpoint is reached in 44 s, and the stack power change is 4208 W–860 W. The E1050 electrolyzer is then able to increase and decrease its stack power at the rates of 19 Ws^{-1} and −76 Ws^{-1}, respectively, according to the current and voltage measurement data acquired using the analog input modules and compact DAQ system. The capability to change the stack power then stays well below the values typically presented in literature: the ramp-up from minimum load to nominal can be performed at a rate 0.4% s^{-1}, while the typical ramp-up performance of PEM water electrolyzers is 10% s^{-1}–100% s^{-1} as presented in Table 2.

PEM water electrolyzer as a part of solar PV system

When dynamic operation is considered, the power production of a single solar PV plant is especially challenging to follow because of the dynamical behavior of the irradiation, due to natural cloud movement, which can suppress power production in one moment or, vice versa, boost the production rapidly. However, the dynamics of a maximum power point tracking (MPPT) controller are slower than the sudden changes in irradiation caused by clouds. Change in the position of the sun causes only slow and smooth changes to the electricity production, as illustrated in Fig. 6.

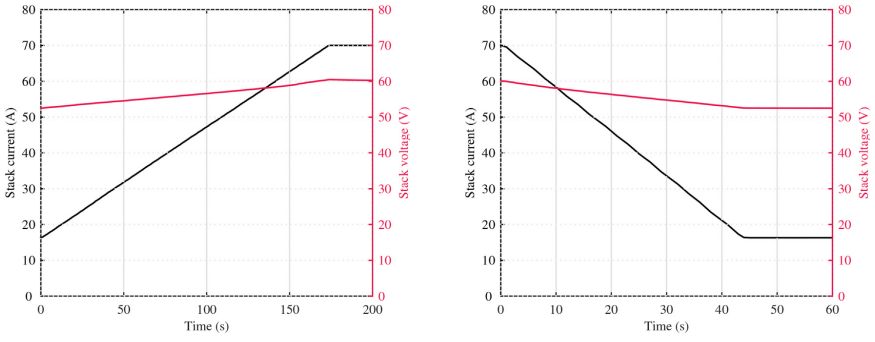

Fig. 5 – Response of the E1050 PEM water electrolyzer as the stack current reference is changed at $t = 0$ s. The stack temperature is at the designed 70 °C and hydrogen outlet pressure is restricted to 2.0 MPa. (a) From minimum to maximum. (b) From nominal to minimum stack current.

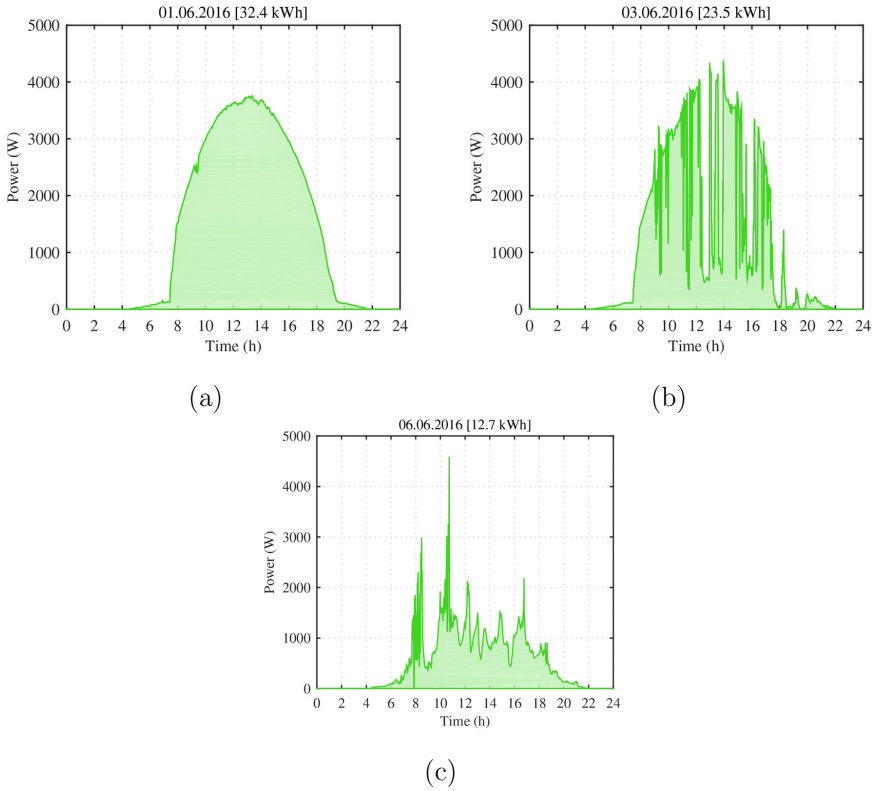

Fig. 6 – Measured solar PV production with the 5 kW_p test system. (a) Clear summer day. (b) Summer day with variable weather conditions. (c) Cloudy summer day.

The power references in Fig. 6 were applied to control the PEM electrolyzer. The electrolyzer was operated with data from the inverter MPPT power and the dynamics of the 5 kW_p system. Ten hours of solar PV data at 1 s sampling time were selected for each test day. The PEM electrolyzer is operated in current control mode where the stack current reference is calculated from the solar power reference and the measured PEM stack voltage. The internal automation system of the electrolyzer causes a constant current reference offset where the actual stack current is higher than the current setpoint [23]. To account for the current reference offset, the solar inverter MPPT power references were upscaled to match the resulting PEM stack power.

The current reference is applied to power the PEM electrolyzer when the electrolyzer can be powered up to its minimum safe load, even momentarily. The dynamic operation started when the hydrogen production system was already operational and the nominal stack temperature of 70 °C had been reached. The water electrolyzer was operated continuously for 10 h for each of the three different reference summer days. The PEM electrolyzer was driven in current control mode, where the current setpoint is calculated according to the solar power reference and the measured stack voltage. For each test run, the hydrogen outlet pressure was restricted to 2.0 MPa, which sets the minimum safe load to 25% of nominal 70 A. A higher hydrogen outlet pressure would only further limit the control range of the water electrolyzer, and hence increase the electricity storage requirement, if off-grid operation is considered.

The required storage size is estimated for each test case as the PEM electrolyzer was operated in on-grid mode, i.e. integrated into the electricity grid. The electricity grid then serves as a virtual battery. The requirement for the power output of the storage can be calculated by subtracting the renewable power production reference from the PEM electrolyzer stack power. Then, the storage energy requirement can be integrated from the instantaneous difference as a function of time. The electric grid balance—in terms of power and energy either supplied to or drawn from the grid—is illustrated as a function of time in Fig. 7.

In Fig. 7, an instantaneous negative power balance corresponds to power supplied to the electricity grid, which then

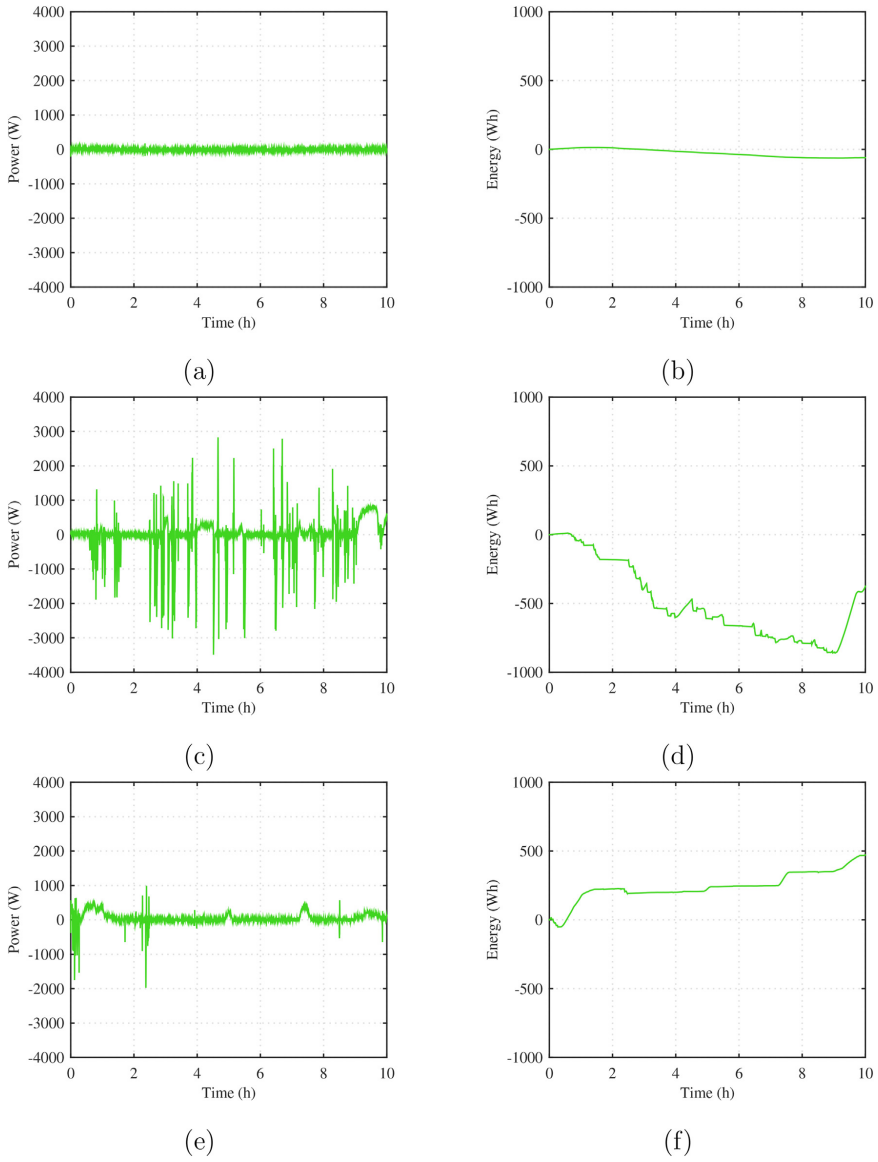

Fig. 7 – Electricity grid power and energy balance in on-grid operation electrolyzer for the three different test days. (a), (b) Clear summer day. (c), (d) Summer day with variable weather conditions. (e), (f) Cloudy summer day.

indicates excess renewable power production. Positive power balance, meanwhile, represents power drawn from the electricity grid. In the clear summer day case, the maximum increase in instantaneous solar PV power is 102 Ws^{-1}, and in turn the maximum decrease in power −116 Ws^{-1}. However, operation during the 10-h test period is the least dynamic overall, and the grid power balance stays within 200 W at any given time.

During the summer day with variable weather, the weather changes abruptly from cloudy to clear and vice versa several times. The maximum power rise speed of the solar PV power reference is 1116 Ws^{-1} and power drop −1055 Ws^{-1}, which

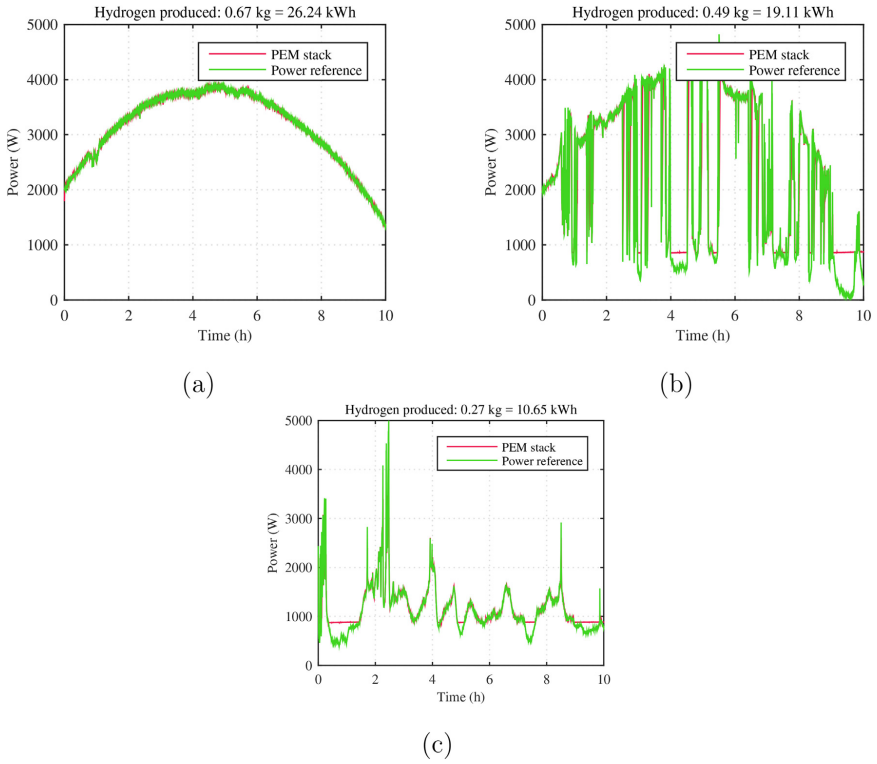

Fig. 8 – PEM electrolyzer stack power and the power reference used in dynamic operation tests. (a) Clear summer day. (b) Summer day with variable weather conditions. (c) Cloudy summer day power reference.

creates the most challenging operation regime for the studied PEM electrolyzer, far exceeding the dynamic capabilities of the electrolyzer stack and system configuration. The maximum instantaneous power supplied to the electric grid is 3492 W, and the maximum power drawn from the grid to power the electrolyzer is 2830 W. The cumulative grid energy balance in Fig. 7(d) stays negative during the 10-h period, which further illustrates the excess renewable power production and its rapid dynamics. The minimum energy balance becomes −860 Wh, which can be limited using modern supercapacitors, in other words, by shaving the short peaks in the power difference between the water electrolyzer and solar PV. At $t = 4$ h and at $t = 9$ h, the grid energy balance starts to increase linearly for a while. This is caused by a situation where the solar PV power reference decreases below the minimum safe load of the PEM electrolyzer and grid electricity is required to maintain continuous and safe operation of the hydrogen production process. Otherwise, the PEM electrolyzer should be shut down, which would be the case in off-grid operation mode. The solar power reference and the measured PEM stack power during the dynamic operation tests are illustrated in Fig. 8.

In the final test case, the cloudy summer day solar PV reference still provides brief bursts of power, but the renewable energy production total is the smallest of the three test days. This power reference, due to its momentary peaks, enables the electrolyzer stack power to increase from the minimum load. For the vast majority of the 10-h period, the grid energy balance stays positive, accumulating to 472 Wh by the end.

Conclusion

In this paper, measurements from a 5 kW_p fixed installation solar power plant at 1s sampling time were used as a power reference for a 1 Nm^3h^{-1} PEM water electrolyzer. The commercial PEM electrolyzer is a part of a complete hydrogen setup and was operated connected to the electricity grid. Study of the dynamic operation capabilities revealed that the rapid response times in load changes typically reported for the PEM technology cannot be achieved with this particular stack and system design and configuration. The studied PEM electrolyzer was able to increase its stack power at the rate of

19 Ws^{-1} and decrease power at 76 Ws^{-1} due to the control limitations set by the manufacturer to prevent the stack from accelerated cell degradation.

The dynamics and controllability of the PEM electrolyzer system were experimentally studied as virtually integrated into a 5 kW_p solar PV power plant in on-grid operation mode. Three reference summer days, with varying level of fluctuations in solar power production, were selected to power the PEM electrolyzer system for 10 h per test day. Only a clear summer day provides power reference variations slow enough for the electrolyzer to follow. Otherwise, for example, a supercapacitor is required to minimize the instantaneous grid power imbalance. If off-grid operation is considered, battery storages are required during electrolyzer start procedures and at times of low to non-existent renewable power production.

Factors affecting the control of the commercial PEM electrolyzer were also studied. As the hydrogen outlet pressure from the water electrolyzer stack was increased from 2.0 MPa to 4.0 MPa, the electrical energy consumption did not show any notable increase. However, the specific energy consumption of the PEM water electrolyzer was increased at higher hydrogen outlet pressures, since the amount of hydrogen effectively produced and supplied to the gas storage was compromised. The Faraday efficiency was decreased, while the requirement for electrical energy stayed practically constant as a function of hydrogen outlet pressure within the range of 2.0 MPa–4.0 MPa. The specific energy consumption was a maximum of 0.2 kWh/Nm^3 higher at 4.0 MPa hydrogen outlet pressure, when compared to operation at 2.0 MPa hydrogen outlet pressure. In a PEM water electrolysis system without separate post-electrolysis compression, the real hydrogen production will therefore be maximized by controlling the stack hydrogen outlet pressure as close to the storage pressure as possible.

Acknowledgements

The authors gratefully acknowledge financial support from Tekes, the Finnish Funding Agency for Innovation, as part of "Neo-Carbon Energy" project (number 40101/14).

REFERENCES

[1] Pleßmann G, Erdmann M, Hlusiak M, Breyer C. Global energy storage demand for a 100% renewable electricity supply. Energy Procedia 2014;46:22–31.
[2] Lehner M, Tichler R, Steinmüller H, Koppe M. Power-to-gas: technology and business models. New York: Springer International Publishing; 2014.
[3] Decourt B, Lajoie B, Debarre R, Soupa O. The hydrogen-based energy conversion fact book. The SBC Energy Institute; 2014.
[4] Gandía L, Arzamendi G, Diéguez P. Chapter 1-renewable hydrogen technologies. In: Gandía L, Arzamendi G, Diéguez P, editors. Renewable hydrogen technologies. Amsterdam: Elsevier; 2013. p. 1–17.
[5] Child M, Haukkala T, Breyer C. The role of solar photovoltaics and energy storage solutions in a 100% renewable energy system for Finland in 2050. In: Proc. 31st Europ. photovoltaic solar energy conf. (EU PVSEC 2015). Hamburg: Germany; 2015. p. 2650–71. https://doi.org/10.4229/EUPVSEC20152015-6DO.7.2.
[6] Clarke R, Giddey S, Ciacchi F, Badwal S, Paul B, Andrews J. Direct coupling of an electrolyser to a solar PV system for generating hydrogen. Int J Hydrogen Energy 2009;34(6):2531–42. https://doi.org/10.1016/j.ijhydene.2009.01.053.
[7] Carmo M, Fritz D, Mergel J, Stolten D. A comprehensive review on PEM water electrolysis. Int J Hydrogen Energy 2013;38(12):4901–34. https://doi.org/10.1016/j.ijhydene.2013.01.151.
[8] Bertuccioli L, Chan A, Hart D, Lehner F, Madden B, Standen E. Study on development of water electrolysis in the EU. Final report in fuel cells and hydrogen joint undertaking. 2014.
[9] Millet P, Grigoriev S. Chapter 2-water electrolysis technologies. In: Gandía L, Arzamendi G, Diéguez P, editors. Renewable hydrogen technologies. Amsterdam: Elsevier; 2013. p. 19–41.
[10] Kopp M, Coleman D, Stiller C, Scheffer K, Aichinger J, Scheppat B. Energiepark mainz: technical and economic analysis of the worldwide largest power-to-gas plant with PEM electrolysis. Int J Hydrogen Energy 2017;42(19):13311–20. https://doi.org/10.1016/j.ijhydene.2016.12.145.
[11] Siemens, kick-off for world's largest electrolysis system in Mainz. 2015. http://www.siemens.com/press/en/feature/2014/corporate/2014-05-energiepark-mainz.php. [Accessed 26 September 2016].
[12] Hydrogenics, E.ON inaugurates energy storage facility using Hydrogenics PEM technology. 2015. http://www.hydrogenics.com/about-the-company/news-updates/2015/10/15/e.on-inaugurates-energy-storage-facility-using-hydrogenics-pem-technology. [Accessed 26 September 2016].
[13] Ursúa A, Gandia LM, Sanchis P. Hydrogen production from water electrolysis: current status and future trends. Proc IEEE 2012;100(2):410–26. https://doi.org/10.1109/JPROC.2011.2156750.
[14] Ursúa A, Barrios EL, Pascual J, Martin IS, Sanchis P. Integration of commercial alkaline water electrolysers with renewable energies: limitations and improvements. Int J Hydrogen Energy 2016;41(30):12852–61. https://doi.org/10.1016/j.ijhydene.2016.06.071.
[15] Clarke R, Giddey S, Badwal S. Stand-alone PEM water electrolysis system for fail safe operation with a renewable energy source. Int J Hydrogen Energy 2010;35(3):928–35. https://doi.org/10.1016/j.ijhydene.2009.11.100.
[16] Miland H, Ulleberg Ø. Testing of a small-scale stand-alone power system based on solar energy and hydrogen. Sol Energy 2012;86(1):666–80. https://doi.org/10.1016/j.solener.2008.04.013.
[17] Laoun B, Khellaf A, Nanceur MW, Kannan AM. Modeling of solar photovoltaic-polymer electrolyte membrane electrolyzer direct coupling for hydrogen generation. Int J Hydrogen Energy 2016;41(24):10120–35. https://doi.org/10.1016/j.ijhydene.2016.05.041.
[18] Ruuskanen V, Koponen J, Huoman K, Kosonen A, Niemelä M, Ahola J. PEM water electrolyzer model for a power-hardware-in-loop simulator. Int J Hydrogen Energy 2017;42(16):10775–84. https://doi.org/10.1016/j.ijhydene.2017.03.046.
[19] Rakousky C, Reimer U, Wippermann K, Kuhri S, Carmo M, Lueke W, et al. Polymer electrolyte membrane water electrolysis: restraining degradation in the presence of fluctuating power. J Power Sources 2017;342:38–47. https://doi.org/10.1016/j.jpowsour.2016.11.118.
[20] Schalenbach M, Carmo M, Fritz D, Mergel J, Stolten D. Pressurized PEM water electrolysis: efficiency and gas crossover. Int J Hydrogen Energy 2013;38(35):14921–33. https://doi.org/10.1016/j.ijhydene.2013.09.013.
[21] Ito H, Miyazaki N, Ishida M, Nakano A. Cross-permeation and consumption of hydrogen during proton exchange membrane electrolysis. Int J Hydrogen Energy

2016;41(45):20439–46. https://doi.org/10.1016/j.ijhydene.2016.08.119.
[22] Koponen J, Kosonen A, Huoman K, Ahola J, Ahonen T, Ruuskanen V. Specific energy consumption of PEM water electrolysers in atmospheric and pressurised conditions. In: Proc. 18th European Conf. on Power Electron. And applicat. (EPE '16–ECCE Europe), Karlsruhe, Germany; 2016. https://doi.org/10.1109/EPE.2016.7695576.
[23] Kosonen A, Koponen J, Huoman K, Ahola J, Ruuskanen V, Ahonen T, et al. Optimization strategies of PEM electrolyser as part of solar PV system. In: 18th European Conf. on Power Electron. And Applicat. (EPE '16–ECCE Europe), Karlsruhe, Germany; 2016. https://doi.org/10.1109/EPE.2016.7695649.
[24] Suermann M, Pätru A, Schmidt TJ, Büchi FN. High pressure polymer electrolyte water electrolyte water electrolysis: test bench development and electrochemical analysis. Int J Hydrogen Energy 2017;42(17):12076–86. https://doi.org/10.1016/j.ijhydene.2017.01.224.
[25] LUT Green Campus. Production figures. 2016. http://www.lut.fi/solar. [Accessed 2 October 2017].
[26] Ulleberg Ø. Modeling of advanced alkaline electrolyzers: a system simulation approach. Int J Hydrogen Energy 2003;28(1):21–33. https://doi.org/10.1016/S0360-3199(02)00033-2.
[27] García-Valverde R, Espinosa N, Urbina A. Simple PEM water electrolyser model and experimental validation. Int J Hydrogen Energy 2012;37(2):1927–38. https://doi.org/10.1016/j.ijhydene.2011.09.027.
[28] LeRoy R, Bowen C, LeRoy D. The thermodynamics of aqueous water electrolysis. J Electrochem Soc 1980;127(9):1954–62. https://doi.org/10.1149/1.2130044.
[29] Awasthi A, Scott K, Basu S. Dynamic modeling and simulation of a proton exchange membrane electrolyzer for hydrogen production. Int J Hydrogen Energy 2011;36(22):14779–86. https://doi.org/10.1016/j.ijhydene.2011.03.045.
[30] Harrison K, Hernández-Pacheco E, Mann M, Salehfar H. Semiempirical model for determining PEM electrolyzer stack characteristics. J Fuel Cell Sci Technol 2005;3(2):220–3. https://doi.org/10.1115/1.2174072.
[31] Biaku C, Dale N, Mann M, Salehfar H, Peters A, Han T. A semiempirical study of the temperature dependence of the anode charge transfer coefficient of a 6 kW PEM electrolyzer. Int J Hydrogen Energy 2008;33(16):4247–54. https://doi.org/10.1016/j.ijhydene.2008.06.006.
[32] Atkins P, de Paula J. Physical chemistry. 9th ed. Oxford University Press; 2010.
[33] Rakousky C, Reimer U, Wippermann K, Carmo M, Lueke W, Stolten D. An analysis of degradation phenomena in polymer electrolyte membrane water electrolysis. J Power Sources 2016;326:120–8. https://doi.org/10.1016/j.jpowsour.2016.06.082.
[34] Barbir F. PEM electrolysis for production of hydrogen from renewable energy sources. Sol Energy 2005;78(5):661–9. https://doi.org/10.1016/j.solener.2004.09.003.
[35] Badwal SPS, Giddey S, Ciacchi FT. Hydrogen and oxygen generation with polymer electrolyte membrane PEM-based electrolytic technology. Ionics 2006;12(1):7–14. https://doi.org/10.1007/s11581-006-0002-x.
[36] Hydrogenics, HyLYZER™ 1 or 2. 2016. http://www.hydrogenics.com/hydrogen-products-solutions/industrial-hydrogen-generators-by-electrolysis/indoor-installation/hylyzer-1-or-2. [Accessed 2 October 2017].
[37] Proton OnSite, S Series: hydrogen generation systems. 2017. http://www.protononsite.com/sites/default/files/2016-09/pd-0600-0061%20revd.pdf. [Accessed 2 October 2017].
[38] Basic considerations for the safety of hydrogen systems. Geneva, CH: Standard, International Organization for Standardization; 2015.
[39] Grigoriev SA, Porembskiy VI, Fateev VN, Auprêtre F, Millet P. High-pressure PEM water electrolysis and corresponding safety issues. Int J Hydrogen Energy 2011;36(3):2721–8. https://doi.org/10.1016/j.ijhydene.2010.03.058.

Publication IV

Vázquez, F.V., Koponen, J., Ruuskanen, V., Bajamundi, C., Kosonen, A., Simell, P., Ahola, J., Frilund, C., Elfving, J., Reinikainen, M., Heikkinen, N., Kauppinen, J., and Piermartini, P.

Power-to-X technology using renewable electricity and carbon dioxide from ambient air: SOLETAIR proof-of-concept and improved process concept

Journal of CO_2 Utilization,
vol. 28, Dec. 2018.

Journal of CO_2 Utilization 28 (2018) 235–246

Contents lists available at ScienceDirect

Journal of CO_2 Utilization

journal homepage: www.elsevier.com/locate/jcou

Power-to-X technology using renewable electricity and carbon dioxide from ambient air: SOLETAIR proof-of-concept and improved process concept

Francisco Vidal Vázquez[a], Joonas Koponen[b,*], Vesa Ruuskanen[b], Cyril Bajamundi[a], Antti Kosonen[b], Pekka Simell[a], Jero Ahola[b], Christian Frilund[a], Jere Elfving[a], Matti Reinikainen[a], Niko Heikkinen[a], Juho Kauppinen[a], Paolo Piermartini[c]

[a] VTT Technical Research Centre of Finland Ltd, PL 1000, 02044 VTT, Finland
[b] Lappeenranta University of Technology, P.O. Box 20, 53851 Lappeenranta, Finland
[c] INERATEC GmbH, Noerdliche Uferstr. 4-6, 76135 Karlsruhe, Germany

ARTICLE INFO

Keywords:
Power-to-X
Carbon capture and utilization
Direct air capture
Water electrolysis
Fischer–Tropsch synthesis

ABSTRACT

This work demonstrates hydrocarbon production directly from water, solar energy, and air—called SOLETAIR. The plant includes direct air capture (DAC) of carbon dioxide, hydrogen production by water electrolysis, and two-step synthesis bench-scale units that operate using grid-connected solar photovoltaic (PV) electricity. In addition, co-feeding of hydrogen and carbon monoxide from gas bundles are utilized to enable scaling between units. This pilot plant achieved a total operating time of approx. 300 h with a combined production of oil and wax of 6.2 kg per day. The mass and energy balances in integration of the units are studied. According to the experiments and studies, potential and bottlenecks to improve the individual units and their integration are found. Finally, a conceptual Power-to-X plant is presented, which can achieve energy and carbon efficiencies of 47% and 94%, respectively, considering liquid and solid hydrocarbons as products.

1. Introduction

According to the Paris UN Climate Change Conference held in December 2015 [1], the CO_2 net emissions of the whole energy sector have to be close to zero by 2050 to limit the global mean temperature rise under 1.5 °C above the preindustrial level. A change of this nature would require practically CO_2-free power generation, and the energy system could thus be based predominantly on wind and solar power [2]. However, there are three main barriers to this transition: the intermittency of solar and wind power, the fuel needs of the transport sector, and the production of chemicals. Firstly, both solar and wind power are intermittent by nature, which generally leads to an imbalance between energy generation and consumption if no storage capacity is available. Secondly, the electrification of the whole transportation sector, such as passenger jets, cargo vessels, and heavy working machines, will present a major challenge. Instead, they can be electrified indirectly by using renewable hydrogen or hydrocarbons as their fuel, for example. Thirdly, the chemical industry sector is a significant consumer of oil and gas that are used as a feedstock for manufacturing e.g. plastics and nitrogen-based fertilizers, which should also be based on the use of renewables.

Fuels produced from CO_2 captured from ambient air can be carbon neutral as the cycle of CO_2 is closed [3,4]. The potential global upper bound for annual CO_2 removal has been estimated to be in the scale of 10 Gt for direct air capture (DAC) with reliable storage [5]. When driven with renewable energy, DAC is a net negative CO_2 emissions technology that can sequester previously emitted carbon dioxide from point and diffuse sources such as transportation [6]. Furthermore, there are already studies related to DAC technology that present select cases where the separation of CO_2 from the air to moderate purities is energetically equivalent to the work requirements using other CO_2 separation techniques from flue gases with high concentration of CO_2 [7,8].

Power-to-Gas, Power-to-Liquids, or more generically, Power-to-X conversion concepts arise as a synergetic solution both for storing energy from intermittent renewable energy sources and producing carbon-neutral fuels from CO_2 emissions [9]. Piloting of the Power-to-X technologies is gaining ground and even reaching an industrial scale, the Audi methanation plant (synthetic natural gas production using alkaline water electrolysis and methanation of raw biogas), the Carbon Recycling International methanol synthesis plant (alkaline electrolysis, geothermal steam emission CO_2, and methanol synthesis), and the

* Corresponding author.
E-mail address: joonas.k.koponen@lut.fi (J. Koponen).

https://doi.org/10.1016/j.jcou.2018.09.026
Received 27 June 2018; Received in revised form 27 August 2018; Accepted 30 September 2018
Available online 15 October 2018
2212-9820/

Sunfire Power-to-Liquids plant (solid oxide electrolysis, DAC, and FT synthesis planned) being examples of this trend [10–12].

Many technologies can be applied for the production of fuels and chemicals from CO_2 and H_2, such as synthetic natural gas, Fischer–Tropsch (FT) products, methanol, or even polymers and specialty chemicals. For the Power-to-X concept, these products are part of the few solutions existing for seasonal storage of energy. The production of kerosene or other heavy fuels from CO_2 emissions and renewable electricity is gaining interest to indirectly electrify aviation and heavy-duty transportation sectors. It has been estimated that the indirect electrification of the transportation sector would increase the electricity consumption in the European Union from 2.8 PWh in 2013 to more than 10 PWh in 2050. Furthermore, the main part of electricity would be used for water electrolysis to produce hydrogen for Power-to-X processes [13–15].

In this paper, a Power-to-X process is experimentally verified with a modular and transportable pilot plant capable to produce renewable liquid and solid hydrocarbons. The mass and energy balances of the complete Power-to-X process are studied for the production of gaseous, liquid, and solid hydrocarbons from solar energy, water and CO_2 captured from ambient air. This is the first Power-to-X pilot plant in which the complete process chain is in the same place. Each of pilot plant's units—DAC, water electrolysis, and two-step synthesis—are experimentally studied. The experimental results, together with literature and process simulations, are then used as a basis for improving the entire system. Based on these improvements, a theoretical Power-to-X concept plant is presented where the developed process concept focuses on the energy and carbon efficiencies of the complete Power-to-X process.

2. Fundamentals of the Power-to-X process

Renewable electricity from a solar PV power plant is used for DAC of CO_2, hydrogen production with water electrolysis, and two-step synthesis process. CO_2 and hydrogen are supplied to FT process to produce gas, liquid and solid hydrocarbons as shown in Fig. 1. Fundamentals of each of the main units of the Power-to-X process are introduced in the following subsections.

2.1. Direct air capture of carbon dioxide

DAC is a technology for collecting CO_2 from ambient air, where the concentration of CO_2 is orders of magnitude lower than that of point sources such as flue gas and other industrial emissions. DAC uses a medium (solid or liquid) that has an affinity to CO_2. The medium is a base which forms covalent bond with the partially acidic C atom of CO_2 [16]. The most common medium for DAC is solid sorbents containing amines. These sorbents capture CO_2 by a chemisorption process forming a carbamate ion or carbamic acid [17].

To collect the chemisorbed CO_2 and regenerate the adsorbent, heat and/or vacuum is applied. When both heat and vacuum is used, the process is called temperature-vacuum swing adsorption (TVSA) process, which allows the operation of the desorption at a lower temperature ($\leq 100\,^{\circ}C$) compared to temperature-swing adsorption. This is an attractive option since low-quality heat can be used.

Research on the improvement of DAC extensively involves the development of adsorbent properties to increase the CO_2 working capacity [18]. Amine bearing polymers such as polyethylenimine (PEI) impregnated to supports have been widely used as the active compound for CO_2 capture applications [19–24]. Aminosilanes which are covalently bonded to supports have also been applied for DAC [25–29]. Metal organic frameworks have also been recently developed with reported capability to maintain working capacity even after exposure to humid air [30].

In addition to sorbent development, the adsorption chamber design and process control can be improved. First, the DAC systems require a significant amount of air to meet the production requirement because of the dilute concentration of CO_2. Secondly, as DAC uses ambient air, the need to control the process based on weather conditions is equally important to optimize the energy consumption of the process.

2.2. PEM water electrolysis

In water electrolysis, electrical and thermal energy are converted into chemical energy, which is stored as hydrogen, and oxygen is produced as a byproduct. According to Faraday's laws of electrolysis, the production of hydrogen is directly proportional to the electric charge transferred at the electrodes. The lowest voltage required for the water decomposition to occur is called the reversible voltage. Without auxiliary heat, the minimum voltage required is higher than the reversible voltage, i.e. the thermoneutral voltage level [31,32]. The reversible voltage and thermoneutral voltage at standard ambient conditions are 1.23 V and 1.48 V, respectively. According to the thermoneutral voltage, the minimum energy required to produce 1 kg of hydrogen is 39.4 kWh, which is equal to the higher heating value (HHV) of hydrogen.

Polymer electrolyte membrane (PEM) water electrolysis has gained interest due to its compact system design, reportedly superior dynamic operation capability [13,33,34], and high voltage efficiency (< 82% HHV) at greater current densities compared to the traditional alkaline technology. The high cost of components and typically inferior lifetime have been the main factors limiting the emergence of PEM technology [35], although improved stack power density and high efficiency have

Fig. 1. The main idea of the SOLETAIR Power-to-X process producing CO_2 neutral hydrocarbons with renewable electricity.

moved the technology into the MW-scale [36,37]. Commercial PEM electrolyzers typically operate at current densities of 0.6–2.0 A cm^{-2} and at operating temperatures of 50–80 °C, while alkaline electrolyzers operate at current densities of 0.2–0.4 A cm^{-2} [33]. The system cost for PEM water electrolyzers has been reported to be almost two times of the cost of traditional alkaline water electrolysis systems [34].

2.3. Two-step synthesis

FT is a well-known technology for production of gas, liquid, and solid hydrocarbons from synthesis gas, also named syngas. Syngas contains a mixture of H_2 and CO, and usually some CO_2. The product consists of a distribution of linear hydrocarbons of different carbon numbers, which obey the Anderson–Schulz–Flory (ASF) distribution [38]. The ASF distribution can be described using one parameter, the chain-growth probability (α). The product distribution depends on the operating conditions and the catalyst composition. FT is a highly exothermic reaction operated at high pressures (20–30 bar) and relatively low temperatures (180–250 °C). FT catalysts perform with low activity (Fe-based catalysts) or complete inactivity (Co-based catalysts) towards CO_2. Thus, CO-rich syngas is required as a feedstock of the FT. For that reason, using CO_2 as a carbon source requires a two-step process combining production of CO from CO_2 by reverse Water-Gas Shift (rWGS) reaction and subsequent FT [39].

The rWGS is an endothermic reaction favorable at high temperatures (over 600 °C). The chemical equilibrium of rWGS is independent on pressure, and product formation increases with increasing temperature. However, operating rWGS at a high pressure has its advantages and disadvantages. High pressure increases methane formation by methanation reactions, and even carbon formation by the Boudouard reaction or other carbon formation reactions. On the other hand, operating at a high pressure reduces the reactor size by increasing the residence time of the reactants in the reactor and provides an option of removing compression between the rWGS and the FT if both steps are operated at the same pressure [40,41].

3. Description of the SOLETAIR pilot plant

The pilot plant was located at the premises of Lappeenranta University of Technology (LUT) in the summer of 2017. The pilot plant consisted of four parts; a 206.5 kW_p solar PV power plant [42], a DAC unit, a hydrogen production unit [43], and a two-step synthesis unit. However, the production capacities for H_2 and DAC were lower than the feed requirement of the synthesis unit. For that reason, a gas container was used for co-feeding of CO and H_2. Furthermore, electricity from the grid was used to run the electrolysis in the night-time as no electric battery unit was integrated into the system—the carbon intensity of grid electricity in Finland is 0.2 kg kWh^{-1} [44]. Technical specifications of the pilot plant are presented in Table 1. The key sea-container-installation units of the pilot plant (DAC, hydrogen production, and mobile synthesis) are illustrated in Fig. 2.

3.1. Direct air capture unit

Key specifications of the DAC unit used in this study are listed in Table 1. Characterization and equilibrium performance of the adsorbent are presented in [45,46]. The DAC unit (developed and supplied by Hydrocell Oy) was instrumented for data collection, visualization, and analysis.

The operating principle of the DAC is shown in Fig. 3. Immersed in the bed of adsorbent is a brush type heat exchanger, which is used to heat the bed during the desorption step. Two beds are operated in parallel, and they are subject to the same stage of operation simultaneously. There are four stages of the TVSA operation. The first stage of operation is the adsorption process (Fig. 3a) that lasts for ca. 20 h. In this stage, air is led through the column via a flow distribution plate to maximize mass transfer. In the second stage (Fig. 3 b), the remaining air (mainly O_2 and N_2) is removed using a two-stage vacuum pump. The purging step is essential to achieve high-purity CO_2 gas required for the synthesis. Purging lasts for 15 min. The next stage in the operation is the heating stage, and it lasts for 30 min (Fig. 3c). Warm glycol-water mixture (20% ethylene glycol) from a 3 kW boiler is pumped to the intra-bed heat exchanger to preheat the bed and desorb some gases in preparation for the next step, shown in Fig. 3d. Finally, after the preheating stage, CO_2 is collected from the bed through the product gas line. The hot gases from the beds pass through an ambient-air-cooled heat exchanger and a water trap (right water trap) before being sucked by the product vacuum pump. Then, the product gas, which is mainly CO_2 at this point, passes again through the ambient-air-cooled heat exchanger and another water trap (left water trap) for further cooling and drying before being compressed. The product gas is stored in a gas bundle (12 × 50 L) and a 50 L buffer tank.

3.2. Hydrogen production unit

A hydrogen laboratory system manufactured by IRD Fuel Cells (currently known as EWII Fuel Cells) is built in a standard shipping container. The hydrogen production process in the laboratory setup is the following: Inlet water to the electrolyzer is first deionized to decrease the conductivity of the supplied water. The commercial PEM water electrolyzer E1050 (IRD) system, which is illustrated in Fig. 4 and presented according to its technical specifications in Table 1, then decomposes the water into hydrogen and oxygen. The water electrolyzer is powered by two PAP3200 DC power supplies (Powerfinn) connected in parallel. The dew point of the outlet hydrogen gas is then decreased in a hydrogen gas drying unit (IRD) to −70 °C to prepare it for outdoor storage in Nordic conditions. The total volume of the pressurized hydrogen gas storage is 700 L. Both the hydrogen and oxygen gas outlet pressures are controlled by back-pressure valves. The designed pressure levels of the E1050 electrolyzer for hydrogen and oxygen gases are 50 bar and 2 bar, respectively.

Operating temperature, water inlet pressure, water conductivity and flow, hydrogen outlet pressure, stack voltage, stack current and

Table 1
Technical specifications of the DAC unit, electrolysis unit, and the two-step synthesis unit with the most relevant values.

DAC unit		Water electrolysis unit		Two-step synthesis unit	
Rated CO_2 production	3800 g d^{-1}	Hydrogen production rate	90 g h^{-1}	Preheater rWGS temp.	max. 450 °C
Max. air flow	1500 m^3 h^{-1}	Nominal stack power	4.5 kW	rWGS temp.	850 °C
Air temp. for blowers	−40–80 °C	Nominal voltage	64 V	rWGS pressure	1–5 bar
Vacuum (desorption, min)	5 mbar	Nominal current	70 A	Condenser rWGS temp.	0–5 °C
Max. water temp.	100 °C	Operating temp.	70 °C	Compression ratio	5–10
Cartridge content	Amine-funct. polymer resin	Number of cells in series	33	Preheater FT	200 °C
Number of cartridge/bed	8	Cell cross-sectional area	69 cm^2	FT temp.	200–250 °C
Mass of adsorbent/cartrigde	30 kg	Hydrogen purity	> 99.995%	FT pressure	20–30 bar
Temp. of operation	ambient to 90 °C	Hydrogen pressure	15–50 bar	Hot trap temp.	165–170 °C
Pressure (adsorption)	1.005 bar	Oxygen pressure	1.5–2.5 bar	Cold trap temp.	5–10 °C

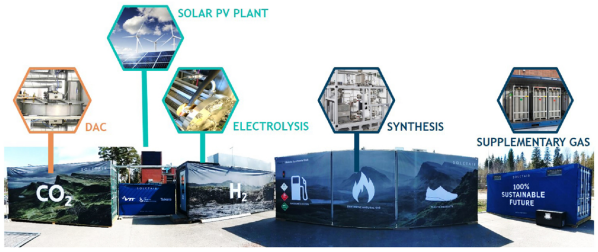

Fig. 2. SOLETAIR pilot site.

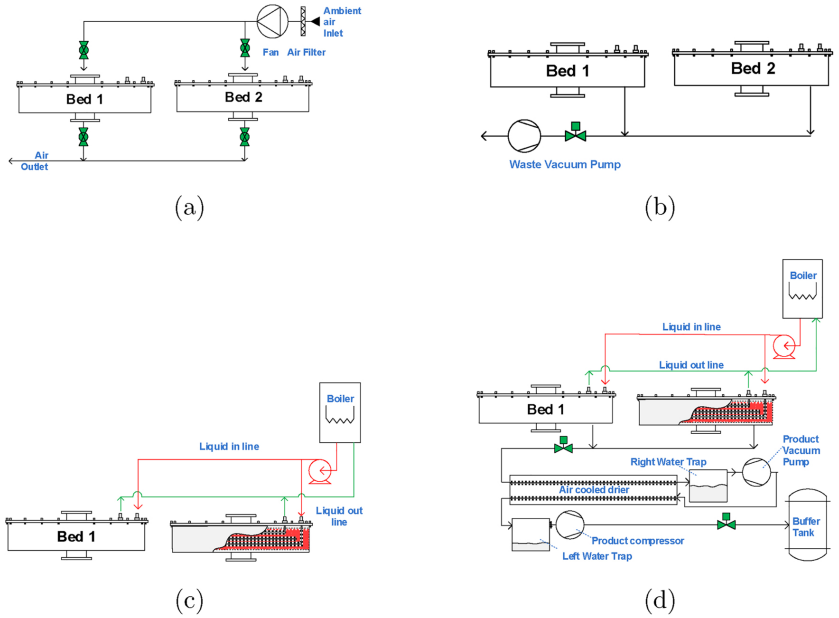

Fig. 3. Stages of TVSA operation of the DAC unit. (a) Adsorption. (b) Purging. (c) Heating. (d) Desorption.

individual cell voltages are measured by the IRD's measurement system. An additional data acquisition system (National Instruments) was added to support the existing monitoring system.

3.3. Mobile synthesis unit for the two-step process

The mobile synthesis unit is a multi-purpose container-size demonstration unit. The two-step process, illustrated in Fig. 5 , consists of a rWGS module (VTT) and a FT micro-structured heat exchanger reactor (INERATEC). A summary of the specifications of this setup are presented in Table 1.

The rWGS reaction is performed in a fire-proof steel tubular reactor filled with metallic monoliths of 20 mm in diameter coated with precious metal catalyst. The reactor is dimensioned for CO_2 inlet flow rate of 2 N L min^{-1} based on the maximum CO_2 production capacity of the DAC unit. The tubular reactor is heated externally by an electric oven. The gas mixture is externally electrically preheated to temperatures up to 450 °C before entering the reactor. Two thermocouples are placed at the top and bottom of the catalyst bed. The reactor could be operated at a maximum of 850 °C and 10 bar due to the limitations of the construction material of the reactor. The reactor operating conditions are kept constant during the test campaigns at 850 °C at the outlet of the catalyst bed, and 4 bar pressure. The feed gas for the rWGS is 0.6–0.8 L min^{-1} of CO_2, 1.2–1.6 L min^{-1} of H_2 and 0.11–0.15 L min^{-1} of N_2. Nitrogen is added for gas analysis purposes. The feed gas composition for the rWGS is adjusted to produce an outlet gas composition of the rWGS with a H_2/CO ratio ≈ 2.1 matching the requirements of the FT process. The gas feedstock for rWGS was kept constant during the test campaign as long as possible. An air-driven piston compressor compresses the syngas produced by the rWGS from 4 bar to over 20 bar (operating pressure of the FT reactor).

The FT is performed using an industrial cobalt-based catalyst in a plate-type microstructured heat exchanger reactor cooled by high-pressure boiling water. The reactor is dimensioned for inlet flow rates up to 2 N m^3 h^{-1} of CO and 4 N m^3 h^{-1} of H_2. However, FT module employs only 1 N m^3 h^{-1} of CO and 2 N m^3 h^{-1} of H_2 for the test

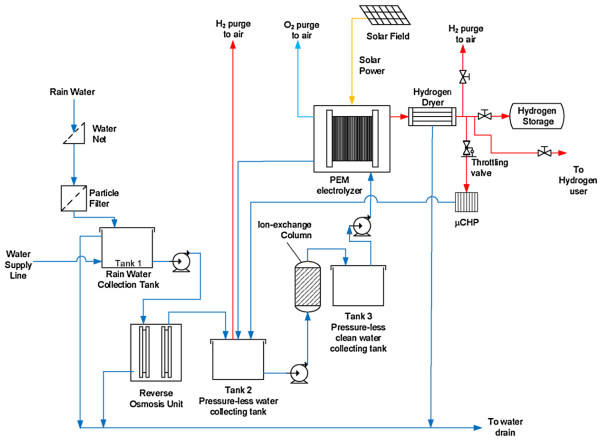

Fig. 4. Simplified process flow diagram of the H_2 production system.

campaigns of this work. Owing to the limitations of the CO_2 production from the DAC unit and H_2 production from the PEM electrolysis unit, the FT module requires co-feeding of stored bundles of both CO and H_2 to match the continuous feed requirements ($1\,N\,m^3\,h_{CO}^{-1}$ and $2\,N\,m^3\,h_{H_2}^{-1}$). These bundle gases of CO and H_2 (AGA) have a gas quality of 99.8% and 99.95%, respectively. The FT reactor is operated at 230–240 °C and ca. 20 bar. After the FT reactor, the products are separated by condensation at different temperatures (Fig. 5). First, the "solid" product is condensed in a hot trap at a temperature around 165–170 °C. Then, the liquid product is condensed in a cold trap at a temperature of 5–10 °C. This liquid product is formed by an aqueous phase and an oil phase. The rest of FT products and unreacted gases are vented into the atmosphere during the tests. Part of this gas is used for online analysis purposes. The conversion of the reactants and the FT gas product composition are calculated using an online gas chromatograph. The composition of the solid and liquid products are analyzed a posteriori by gas chromatography. The liquid product is analyzed as such while the solid product is dissolved in cyclohexane.

4. Results and discussion

4.1. Experimental results

The test campaigns of this study were performed in summer during weeks 24, 26, 28, and 32 of 2017. The FT process was set to emphasize wax production for demonstration purposes. The units were operated simultaneously during these four test campaigns. The exact duration of the test campaigns varied as explained in the following subsections. The main objective of these test campaigns was proving the concept and gaining operational experience by running the system continuously during the test week. Further, the overall operation and energy balance of the bench-scale plant are analyzed.

4.1.1. CO_2 capture from air

Adsorption began immediately after the desorption period of the previous cycle, which is illustrated in Fig. 6. Introducing ambient air (400 ppm with very minor variations in concentration) to the hot bed increases the CO_2 concentration, temperature and humidity of the air leaving the beds. After about 1 h, the CO_2 concentration at the inlet and

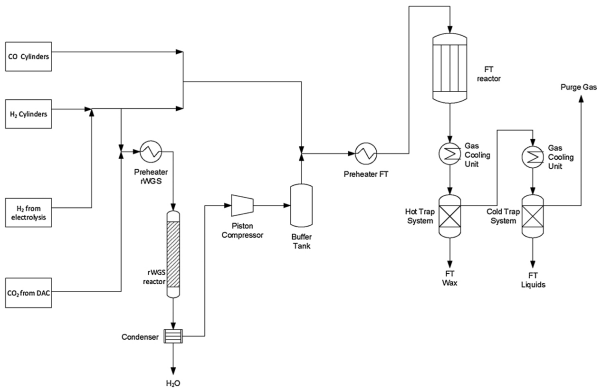

Fig. 5. Simplified process flow diagram of the mobile synthesis unit.

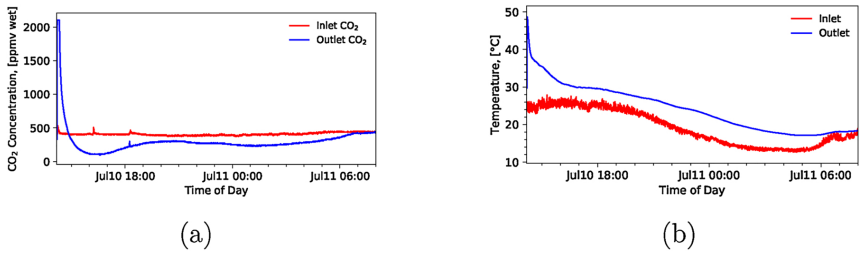

Fig. 6. CO_2 and temperature at the inlet and outlet of beds 3 and 4. (a) CO_2 concentration. (b) Temperature.

outlet were equal, which signified the actual start of CO_2 adsorption. During the first 3 h of the adsorption, the CO_2 concentration of the exiting air could decrease as low as 100 ppm for all the beds. As the adsorption continued, the CO_2 concentration at the exit started to increase and approached the inlet concentration indicating saturation of the bed. During the adsorption process, the pressure drop across the bed is 400 mbar. At the start of the heating process, warm liquid entered the intra-bed heat exchanger at around 80 °C and left at 55 °C. The bed was at ambient temperature. At the start of the desorption period, the bed and the liquid leaving the bed were almost at the same temperature and were rising at a rate of 0.25 °C min^{-1} until the inlet temperature reached about 90 °C. The 90 °C limit was set to protect the adsorbents from excessive heating, which may degrade the material. Thirty minutes before the desorption ended, the temperature of the bed and the liquid inlet/outlet point dropped abruptly as a result of heating the next bed pairs. The desorbing beds are in parallel with the beds being heated. The heating power of the boiler is shared between the two bed sets. At the end of the desorption, the bed temperature rapidly cooled down as a result of blowing cooler ambient air directly to the bed.

Fig. 7 also shows the waste and product vacuum line pressure in the production phase. During the purging step, the bed was closed and waste gases were removed by vacuuming down to 50 mbar(abs). The bed vacuum pressure is presented as the product vacuum line. The purging step was performed isothermally and thus, only pressure was changed. As reported elsewhere, the effect of pressure in the desorption of CO_2 is much less significant than the effect of temperature [45]. For this reason, the loss of CO_2 during the purging step was considered insignificant. Over the desorption period, the vacuum pressure was between 100 mbar(abs) and 200 mbar(abs). The current setup could not maintain an isobaric condition during the vacuum operation because of problems in the product gas compressor operation. As a result, there was significant variation in the amount of CO_2 and water produced (see Table 2). From the production data, the mean molar ratio was 4.6. The quality of DAC produced water is compared to the deionized water supplied to the PEM water electrolyzer in Table 3.

Table 2
Daily production data, energy usage, and product gas quality of the DAC during the SOLETAIR campaign periods. Some test days were excluded from the analysis due to missing data when the logging system was not running.

Stat. (–)	CO_2 prod. (g)	H_2O prod. (g)	E_{used} (kWh)	$E_{specific}$ (kWh $kg^{-1}_{CO_2}$)	CO_2 (vol-%)	H_2O (vol-%)	O_2 (vol-%)
min	729	1493	27.5	15.0	93.85	0.12	0
max	2749	4770	41.8	49.0	100	1.17	1.59
mean, μ	1564	2954	36.9	26.4	98.55	0.58	0.3
std. dev., σ	549	939	4.4	10.5	0.70	0.23	0.23
σ/μ	0.35	0.32	0.12	0.40	0.007	0.40	0.74

Table 3
Quality of the water from the DAC and the water fed to the electrolyzer.

Sample	Total carbon (mg L^{-1})	Total nitrogen (mg L^{-1})	NH_4 (mg L^{-1})	pH (–)	Conductivity (µS cm^{-1})
DAC water	119	101	113.7	7.59	679.5
Electrolysis water	6	0	< 0.05	5.27	2.222

The CO_2 gas quality during the test campaign is given in Table 2. The medians of CO_2 concentrations were all above 97 vol-% in all test campaigns. The equilibrium working capacity of the adsorbent (moles of CO_2 per kilogram of adsorbent) is reported elsewhere [45]. Due to the large variation in CO_2 production in this device, it is difficult to provide a meaningful comparison between the equilibrium working

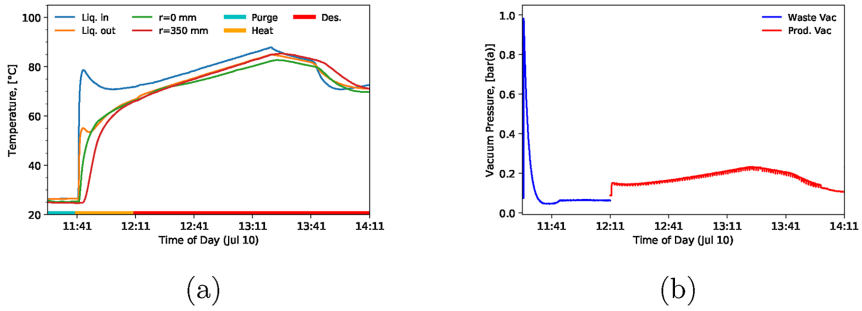

Fig. 7. Key temperature and vacuum pressure measured for Bed 4 during the production phase. *r* is the radial distance from the center of the bed. The radius of a bed is 500 mm. (a) Temperature. (b) Vacuum pressure.

capacity reported in [45]. In a test campaign, the collected CO_2 gas was fed straight to the rWGS reactor of the two-step synthesis process without further purification.

The power consumption of the DAC had two distinct regions. The low power usage region, which lasted for ca. 15 h with a power usage of 0.6 kW, occurred when the fans were the only power-consuming devices during the adsorption period. Then, the high power usage region, which lasted for approx. 9 h with an average power usage of 4 kW, occurred for the desorption period when the boiler was running and was consuming most of the power.

The total energy used per cycle is calculated from power data. Unlike the CO_2 production, the energy used per cycle does not vary significantly (see Table 2) because the operation schedule is almost constant for all the test runs. There were instances during the production operation when the boiler temperature had reached 90 °C and caused the boiler to turn off for about 30 min; this caused the variability in total energy consumption of the cycle.

The electrical requirement is for driving the fans, vacuuming, product compression, data logging setup, and heating the liquid pump. On average, 57.8% of the specific energy requirement is for the thermal requirement, the rest is for the electrical requirement. The average total energy consumption is 26.4 kWh $kg^{-1}_{CO_2}$, which is an order of magnitude higher compared to the energy requirements of Climeworks DAC unit. Climeworks state an energy requirement of 1.8–2.45 kWh $kg^{-1}_{CO_2}$ (data obtained by request through Climeworks webpage [47]). However, if the amount of CO_2 reaches the designed production capacity of 3.8 kg/cycle by improving the mechanical components of the DAC, the specific energy requirement can be lowered to 9.7 kWh kg^{-1} (based on the mean energy used in Table 2). The production levels of this DAC compared to Climeworks are orders of magnitude different. The high energy requirements of the experimental results was attributed to the losses generated by the relatively small system of the DAC unit where heat losses and compression and vacuum power become very significant.

4.1.2. Hydrogen production

The PEM water electrolysis system presented in Section 3 is smaller in hydrogen production capacity than the FT synthesis in terms of hydrogen consumption. Therefore, the PEM water electrolyser was set to operate at its nominal production capacity of 1 N $m^3 h^{-1}$ (90 g h^{-1}) throughout the test campaigns. Partial load operation was not considered, since hydrogen production had to be maximized. The hydrogen stack outlet pressure was controlled down to 40 bar, while the pressure level in the synthesis process was controlled to 20 bar. The designed hydrogen stack outlet pressure of 50 bar was not selected to ensure continuous operation. The higher pressure from the water electrolyser ensured that the hydrogen production could operate continuously even if the synthesis process would stop for an extended period of time, as the PEM water electrolyzer is set to automatically shut down if the storage pressure meets the hydrogen stack outlet pressure. The oxygen stack outlet pressure was controlled to the nominal 2 bar. The water electrolyser stack was water cooled to 71 °C.

The continuous run times and key mean measurement results from the PEM water electrolysis system are presented in Table 4. The mean stack voltage increases from 60.26 V to 60.63 V over the test campaign weeks. The stack voltage increase can be explained by the increasing trend of the inlet water conductivity. The average stack specific energy consumption was 49 kWh $kg^{-1}_{H_2}$ assuming unity Faraday efficiency. However, if Faraday efficiency is considered, the stack specific energy consumption increases further. The Faraday efficiency of the studied PEM water electrolyzer at 40 bar has been identified as ≥95% in nominal operation in [43]. With an assumed Faraday efficiency of 95%, the stack specific energy consumption increases from 49 kWh $kg^{-1}_{H_2}$ to 51 kWh $kg^{-1}_{H_2}$. Additional losses in the hydrogen production system are caused by the hydrogen gas drying unit (average 2.1 kWh $kg^{-1}_{H_2}$ in nominal operation) and the small-scale DC power supplies of the PEM water electrolyzer.

The energy needed for the water electrolysis is mainly consumed by the PEM stack converting around 80% of the supplied electrical energy into the chemical energy of the hydrogen gas. In the studied system, the efficiency of the DC power source supplying the electrolyzer stack is only around 90%, but the rectifiers used on the industrial scale may reach an efficiency higher than 97%.

4.1.3. Two-step synthesis

The performance of the rWGS reactor was checked every test campaign. The temperature at the bottom of the catalyst bed and pressure of the reactor remained constant during operation with values of 808 °C and 4 bar. The CO_2 and H_2 conversions also remained unchanged throughout steady operation with values of 63% and 34%, respectively. The products were mainly CO and H_2O, but some methane was formed as a side product. The yields of CO and CH_4 were 61.7% and 1.3%, respectively.

The performance of the FT reactor was continuously measured during each of the test campaigns. Fig. 8 a shows the CO conversion over time of each of the campaigns from the start of the campaign. The H_2 conversion was always slightly lower compared to CO conversion due to the slightly over stoichiometric composition of the gas feedstock of the FT reactor with H_2/CO ratio of ca. 2.1. This over stoichiometric composition was chosen in order to avoid carbon formation in the FT reactor. For instance, H_2 conversion was 58.5% when CO conversion was 60.3%. These conversion values were quite representative of the FT process performance [48]. Using these values, the overall CO_2 and H_2 conversions after the rWGS and FT steps were 38% and 72.6%, respectively. Nevertheless, Fig. 8a shows a decline in the catalytic activity of the FT catalyst, which seemed to stabilize after long periods of operation. This initial loss of activity was attributed to the increasing mass transfer limitations on the catalyst surface resulting from the formation and accumulation of the heavier fraction of the FT products in the reactor.

The rate of product formation also decreased over time for all the products as a consequence of the decrease in the CO conversion. However, the ratio between wax and oil formation rate increased over time. This indicated an increase in the average molecular weight of the products from the FT reactor, and thus, an increase in the average alpha value of the product distribution. This effect could be due to the accumulation of waxes in the reactor at the beginning of operation that stabilizes over time.

Table 4
Continuous system runtime and mean values of stack voltage, stack current, and stack inlet water conductivity as well as the produced hydrogen, stack energy consumption, and stack specific energy consumption from the hydrogen production system for each test campaign week. H_2 outlet pressure was controlled to 40 bar, O_2 outlet pressure to 2 bar, and stack temperature to 71 °C in all test campaigns.

Week (–)	t (h)	U_{stack} (V)	I_{stack} (A)	σ (μS cm^{-1})	H_2 prod. (kg)	E_{stack} (kWh)	$E_{s,stack}$ (kWh $kg^{-1}_{H_2}$)
24	72.72	60.26	70.20	1.98	6.31	307.6	48.8
26	95.13	60.39	70.23	2.04	8.25	403.5	48.9
28	100.72	60.53	70.21	2.37	8.74	428.0	49
32	94.00	60.63	70.23	3.12	8.16	400.4	49.1

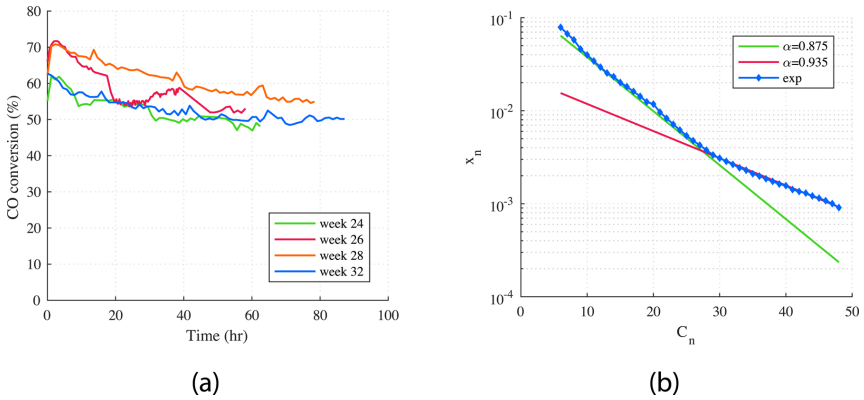

Fig. 8. Measurements of FT synthesis. (a) CO conversion over time for each test campaign. (b) Molar fraction of the components contained in the sum of oil and wax products, and ASF distributions.

Fig. 8b shows the molar fraction of each component taking into account its amount in the oil and wax product. This chart also shows the slopes of the ASF distributions for alpha values of 0.875 and 0.935. The slope of the FT product with a lower carbon number ($< C_{27}$) resembles to the ASF distribution where alpha is 0.875. However, the slope of the distribution switches at values C_{27}–C_{30}. The C_{30+} distribution resembles to an ASF distribution with an alpha value equal to 0.935. This kind of deviation of a product distribution combining two different alpha values has also been observed in the literature [38,49]. The oil product contained hydrocarbons ranging mainly from C_4 to C_{14} (91.1 mass-%). However, it also contained a small amount of propane (1.5 mass-%) and quite a significant amount of C_{15+} (7.4 mass-%). This analysis clearly showed that the oil phase easily dissolved propane and butane, which otherwise should be gas in ambient conditions. The oil product contained mainly paraffinic hydrocarbons but also small quantities of α-olefins and alcohols. The wax product contained an even wider range of hydrocarbons from C_{11} to C_{38} (84.8 mass-%). It also contained $< C_{11}$ (2.5 mass-%) and a significant amount of C_{39+} (12.7 mass-%). The wax product was also mainly formed of paraffinic hydrocarbons with traces of olefins. Further, the aqueous phase produced in the FT reactor contained significant amounts of linear alcohols with a chain length up to octanol. Thus, this aqueous phase would require purification before reuse in the system or to be released into the environment.

4.1.4. Overall results

Fig. 9 shows the simplified diagram of the SOLETAIR pilot plant with the most relevant energy and material input and output streams for each unit during the first day of production on week 32. In the case of the two-step synthesis unit, the value of the electric power input was estimated based on the heat duty of the feed gas heaters and the rWGS reactor, and the duty of the compressor (Fig. 5). The duty of the piston compressor was calculated using an isentropic efficiency of 0.85 [50]. The two heat outputs correspond to the heat of the reaction from the FT reactor, and the rest of heat sources, which are the condenser and the gas cooling units. All the heat duties and the compressor duty were calculated by simulation in Aspen Plus.

In the SOLETAIR pilot plant, only 30.8% of the hydrogen is bound into the end products (including FT gas). Most of the hydrogen forms water together with oxygen in the rWGS and the FT. Moreover, a significant part of the hydrogen travels non-reacting through the synthesis process owing to the conversion limitation of each step of the two-step process. This also affects the energy efficiency of the process as hydrogen is the main energy carrier. 59.5% of the carbon ends up in the FT products. This carbon conversion number reduces to 38% when only the carbon contained in the CO_2 from the DAC is considered. The carbon efficiency is equal to the overall CO_2 conversion of the two-step synthesis by rWGS and FT. This is also due to the conversion limitation of the two-step process. A significant loss in the process is the chemical energy contained in the vented gases containing unreacted H_2 and CO, and FT gases. Therefore, recirculation of unreacted gases into the

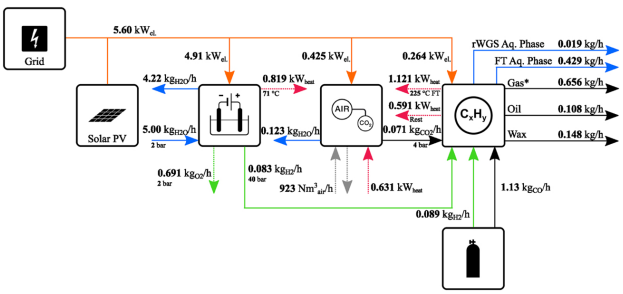

Fig. 9. Simplified diagram of the SOLETAIR pilot plant including mass and energy flow streams based on production during the first day of operation on week 32. *Gas containing both the FT gas product and unreacted H_2, CO, and CO_2.

process is essential in increasing the overall carbon utilization.

4.2. Theoretical Power-to-X plant

The pilot plant described in Section 3 was far from optimal for several reasons. First, the process inside each unit was not optimized, and there was room for improvement in all units. The overall efficiency of the process could also be improved by integrating energy and mass flows between the units. Second, there was a clear mismatch of production capacities between the units because they were not sized only for the purposes of this study. Finally, these container-sized units constituted a relatively small-scale system. Therefore, the heat losses and peripheral equipment generated significant energy loss compared with the overall energy balance. For these reasons, a study of an improved Power-to-X plant was required to get a clear picture of its potential and limitations. The process concept development addressed the issues of the Power-to-X pilot plant and aimed at maximizing the carbon and energy efficiency of each unit and the overall Power-to-X process during continuous operation.

4.2.1. System improvement

Several improvements have been made to this theoretical configuration over the SOLETAIR Power-to-X pilot plant. The improvements for DAC and water electrolysis are based both on experimental results and literature. In the case of the two-step synthesis, the improvements are also supported with simulations of an enhanced two-step synthesis process using the Aspen Plus software.

The limitations in CO_2 and CO conversions can be overcome by recirculation of unreacted gases back to the first step of the two-step synthesis process. However, the gas effluent from product condensation after the FT reactor contains a significant amount of light hydrocarbons that have to be decomposed to form H_2 and CO again, as well as unreacted CO_2, CO, and H_2. Furthermore, these light hydrocarbons are more prone to form carbon at high temperatures than CO_2 and CO. This carbon can cause problems of fouling and clogging in the reactor. One solution for this problem is the catalytic partial oxidation (CPO) by addition of oxygen to the mixture of recirculated gas and "fresh" H_2 and CO_2 feed. The addition of oxygen together with the make-up gas and recirculation gas will help in decomposing the light hydrocarbons and avoiding carbon formation by increasing the O/C ratio in the feedstock of the first step of the process. Now, this first step is called the rWGS/CPO step because it includes both the rWGS reaction and CPO reactions of light hydrocarbons. However, pure O_2 has to be used in order to avoid dilution of the gas mixture with inert components such as the N_2 contained in the air. Thus, the O_2 effluent from water electrolysis is a potential source of pure O_2 for the new two-step process. However, most of the generated electrolytic oxygen would be unused and vented to the atmosphere or used for other external processes.

Another limitation of the two-step synthesis process is the compression between the two steps of the process. Hydrogen can be generated at a high pressure by the PEM electrolyzer (up to 50 bar). In the experimental setup, the pressure of the hydrogen was reduced to 4 bar in the rWGS step. Then, the syngas mixture after the rWGS reactor was compressed to the FT operating pressure (20 bar). Thus, operating the rWGS/CPO reactor at the same pressure as the FT reactor can save the energy used for compression of the syngas between the two steps. Temperature of the rWGS/CPO reactor also has to be increased in order to minimize the formation of methane, which is thermodynamically unfavorable at high temperatures.

Furthermore, the DAC uses the excess heat of the synthesis unit and the water electrolysis. The DAC uses all of the heat from the synthesis unit that is above 80 °C, and part of the heat generated by the PEM stack to cover the heat requirement of the DAC process. However, 79% of the PEM stack excess heat remains unused, and it could be used for other processes that require low temperature heat. On the other hand, the electrolyzer excess heat could also be used for DAC if the higher temperature heat from the synthesis can be used in external processes. This exchange of thermal energy provides versatility depending on the location of the Power-to-X plant.

The water consumption of the electrolyzer could be further reduced by utilizing the water collected in the DAC and the FT, albeit with some limitations. The water collected after the rWGS/CPO step is used to co-feed the electrolyzer to reduce its water consumption. Therefore, 10% of the water requirement for the hydrogen production unit is covered by water recirculation. The amount of water captured by the DAC is heavily dependent on the ambient conditions of humidity. However, the water captured by DAC should be further analyzed to understand the required water purification steps before PEM water electrolysis. Direct use of the DAC water is not reasonable due to the impurities as presented in Table 3. The FT aqueous phase includes significant amount of alcohols in its composition that range from methanol to octanol. These alcohols could accelerate the degradation of the PEM electrolyzer cells, and thus, these should be cleaned out.

4.2.2. Results

The theoretical Power-to-X plant is sized for a PEM electrolyzer stack of 1 MW. This process concept maximizes the overall carbon and energy efficiencies of the system. Special attention is paid to the use of excess heat and water supply between the units. The energy consumption of peripheral equipment (including civil and industrial areas) of the plant such as control systems or other instrumentation is neglected in the calculations.

Fig. 10 shows a simplified diagram of the theoretical Power-to-X plant sized for a PEM electrolyzer stack of 1 MW. This diagram shows the connections of the energy and material streams between units. A summary of the main technical specifications for each unit of the

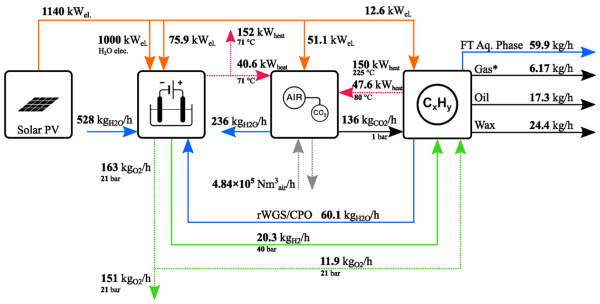

Fig. 10. Simplified diagram of the theoretical Power-to-X plant including mass and energy flow streams. *Purged gas containing unreacted H_2, CO, and CO_2.

Table 5
Technical specification of each unit in the theoretical Power-to-X plant.

DAC unit		Water electrolysis unit		Synthesis unit	
CO_2 production	136 kg h^{-1}	H_2 production	20.3 kg h^{-1}	rWGS/CPO temp.	980–1000 °C
Air flow	4.85 × 10^5 N m^3 h^{-1}	O_2 production	163 kg h^{-1}	rWGS/CPO pressure	20 bar
Blower el. power	51 kW	Water consumption	589 kg h^{-1}	Oxygen requirement	12 kg h^{-1}
Heat power requirement	238 kW	Nominal stack power	1 MW	FT temp.	230–240 °C
Type of adsorbent	Amine-based ads. into monoliths	Heat power prod.	193 kW	FT pressure	20 bar
Operating temp.	Ambient to 100 °C	Operating temp.	71 °C	Total heat power prod.	235 kW
Water prod.	236 kg h^{-1}	H_2 & O_2 pressure	20 bar	Hot trap temp.	170 °C
				Cold trap temp.	5 °C
				Purged gas	6.2 kg h^{-1}
				FT oil production	17 kg h^{-1}
				FT wax production	24 kg h^{-1}
				FT aq. phase	60 kg h^{-1}
				rWGS/CPOx water prod.	60 kg h^{-1}
				Recycle compressor	0.32 kW

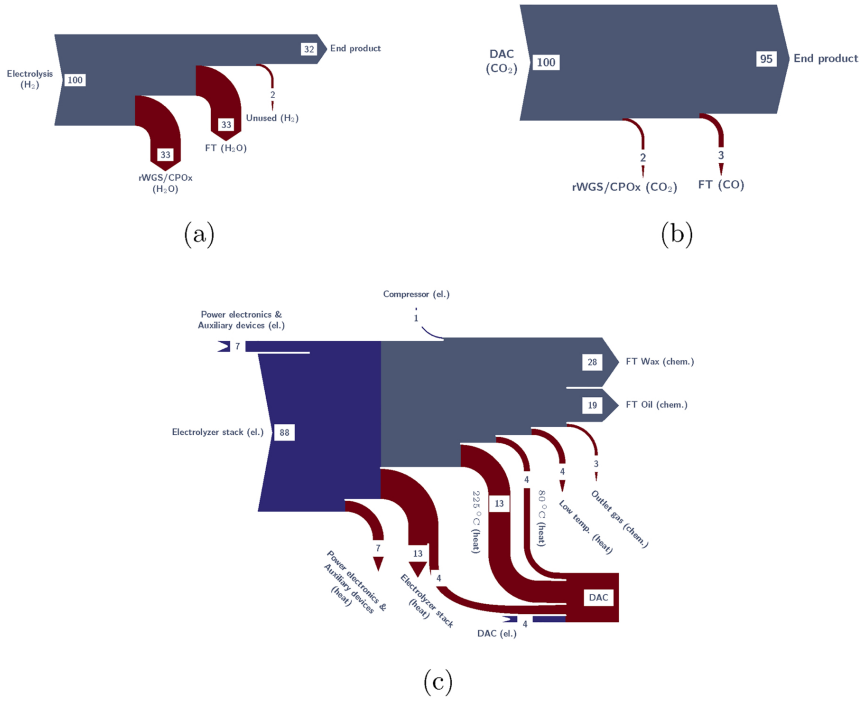

Fig. 11. Sankey diagrams for the overall mass and energy balances of the theoretical Power-to-X plant with 1 MW electrolyzer stack input power. (a) Hydrogen mass balance (% of 20.3 kg h^{-1}). (b) Carbon mass balance (% of 37.1 kg h^{-1}). (c) Energy balance (% of 1140 kW).

theoretical Power-to-X plant are presented in Table 5.

Fig. 11 presents the Sankey diagrams for the energy and mass balances of the theoretical Power-to-X plant. As can be seen in Fig. 11b, 95% of the carbon supplied by the DAC ends up as FT products including gases. The carbon efficiency is calculated from

$$\eta_C = \frac{m_{C,in} - m_{C\,in\,CO_2,out} - m_{C\,in\,CO,out}}{m_{C,in}} \quad (1)$$

where $m_{C,in}$ is the mass of total carbon supplied, $m_{CinCO_2,out}$ the mass of carbon in unused CO_2, and $m_{CinCO,out}$ the mass of carbon in unused CO in the process. The carbon efficiency is 94% considering liquid and wax hydrocarbons as the final products. Only 32% of the H_2 produced by electrolysis is "stored" in the FT products (Fig. 11a). The rest of H_2 is contained in the water formed in the rWGS/CPO and FT steps. Each molecule of CO_2 requires two molecules of H_2 to get rid of the oxygen atoms. Thus, the maximum percentage of H_2 that could be "stored" in the product would be 33.3%. The hydrogen losses are due to the extra oxygen added for the CPO reactions and the H_2 purged with the rest of purged gases. For that reason, approximately two-thirds of the H_2 actually end up forming water. However, the overall energy efficiency of the Power-to-X plant is 50% considering all the FT products, and thus, over half of the electrical energy harvested by the PV power plant

would end up in the FT products. The energy loss due to CPO reactions is approx. 5% of the total energy input. The overall energy efficiency reduces to 47% when only FT oil and wax are considered as final products. The overall energy efficiency of the PtX plant is calculated from

$$\eta_E = \frac{E_{FToil} + E_{FTwax}}{E_{electrolyzer} + E_{DAC} + E_{synthesis}} \quad (2)$$

where E_{FToil} is the chemical energy in the FT oil products, E_{FTwax} the chemical energy in the FT wax products, $E_{electrolyzer}$ the electrical energy consumption of the PEM electrolyzer system, E_{DAC} the electrical energy consumption of the DAC, and $E_{synthesis}$ the electrical energy consumption of the two-step synthesis.

The total average electrical power consumption of the theoretical Power-to-X plant is about 1.14 MW. This electric power is mainly used for electrolysis (1 MW) but also for power electronics (losses) and other auxiliary devices of the H_2 production unit (76 kW), for the air blowers of the DAC unit (51 kW), and for the compressors of the synthesis unit (12.6 kW). Thus, the power for running the air blowers for the DAC represents less than the 3% of the total energy consumption of the plant. The synthesis unit also includes a two-stage compressor to increase the pressure of the CO_2 from the DAC from atmospheric to 20 bar. Considering all these power consumptions, the annual energy consumption of the plant is 9 GWh. The annual solar PV plant production exceeds 2000 kWh/kW_p in the locations in the world where the annual solar radiation is at highest [51]. Under this assumption and assuming that this plant would be powered only by solar energy, the estimated solar PV panel area needed for this theoretical plant would be 2.6 ha. If the plant is driven solely on solar power, a battery energy storage is needed to compensate for variation in daily radiation. If the plant is constantly consuming the nominal power, the battery energy storage capacity should be in the range of 13 MWh. However, by optimizing the plant for variable energy production by adding a hydrogen intermediate storage, overrating the water electrolyzer, and applying an intelligent plant control, the energy storage capacity could be significantly decreased. Further dynamic operation studies and process optimization are required to optimally dimension the battery and intermediate gas storages.

5. Conclusion

The production of carbon neutral fuels based on renewable energy was demonstrated in the SOLETAIR pilot in Finland in 2017. Electricity from a solar PV power plant and the local electricity grid was used for hydrogen production with water electrolysis, direct air capture of CO_2, and two-step synthesis. Fischer–Tropsch synthesis was applied to produce gas, liquid, and solid (wax) hydrocarbons including co-feeding of H_2 and CO from a gas container. Overall, the system achieved a production of 6.2 kg per day of combined FT oil and wax. The system was operated for about 300 h in four test campaigns. The total CO_2 and CO conversions were about 38% and 60.3%, respectively, owing to the conversion limitations from the rWGS and FT reactors. Recirculation of unreacted gases into the process would be required to significantly increase the overall carbon utilization. The energy requirement of the DAC was estimated as 26.4 $kWh\,kg_{CO_2}^{-1}$, 57.8% of which was the required thermal energy.

A theoretical Power-to-X plant is presented. This plant uses only solar PV electricity, water, and CO_2 from ambient air as the feedstock. All the heat requirement of the DAC unit is supplied by the synthesis and water electrolysis units. The water requirement of the electrolyzer is partly covered by the water condensed after the first step of the synthesis. The carbon efficiency of the plant is 94% considering liquid and wax hydrocarbons as final products. The rest of carbon is lost as a consequence of the purging of the effluent gases in the recirculation loop of the synthesis unit. Although two-thirds of the hydrogen ends up forming water again, half of the energy carried by the hydrogen ends up in the FT products. The overall energy efficiency of the theoretical Power-to-X plant is 47% considering liquid and wax hydrocarbons as final products.

Future studies include measurement and weather forecast based DAC process control and system integration of Power-to-X systems into office buildings. Intelligent control of Power-to-X systems requires studying the dynamic behavior of the Power-to-X system units and the required energy and gas storages allowing off-grid operation.

Acknowledgements

TEKES is acknowledged for the main financial support of the SOLETAIR project (soletair.fi). The project partners are also thanked for their financial and in-kind contributions. The SOLETAIR project concept was developed from the work carried out in the Neo-Carbon Energy project (neocarbonenergy.fi).

All the experimental work was performed on the premises of Lappeenranta University of Technology partly thanks to the work of its personnel and resources. Harri Nieminen (LUT) and Tamer Alhalabi (VTT) are thanked for their work during the preparation and operation of the pilot plant. Other project personnel are also thanked for their work in other tasks related to the pilot plant, special thanks being reserved for Johanna Kihlmann (VTT) and Dr. Pasi Vainikka (VTT).

References

[1] S. Fuss, J.G. Canadell, G.P. Peters, M. Tavoni, R.M. Andrew, P. Ciais, R.B. Jackson, C.D. Jones, F. Kraxner, N. Nakicenovic, C. Le Quéré, M.R. Raupach, A. Sharifi, P. Smith, Y. Yamagata, Betting on negative emissions, Nat. Climate Change 4 (10) (2014) 850–853, https://doi.org/10.1038/nclimate2392.
[2] G. Plessmann, M. Erdmann, M. Hlusiak, C. Breyer, Global Energy Storage, (2014), pp. 22–31, https://doi.org/10.1016/j.egypro.2014.01.154.
[3] A. Serdoner, K. Whiriskey, Bellona Europa Reality Check: The 'Power to Liquids' Trap, (2017) (accessed 11.06.18), http://network.bellona.org/content/uploads/sites/3/2017/04/Power-to-Liquids_BellonaEuropa-1.pdf.
[4] D.W. Keith, G. Holmes, D.S. Angelo, K. Heidel, A process for capturing CO_2 from the atmosphere, Joule (Early access) (2018) 1–22, https://doi.org/10.1016/j.joule.2018.05.006.
[5] J.C. Minx, W.F. Lamb, M.W. Callaghan, S. Fuss, J. Hilaire, F. Creutzig, T. Amann, T. Beringer, W. de Oliveira Garcia, J. Hartmann, T. Khanna, D. Lenzi, G. Luderer, G.F. Nemet, J. Rogelj, P. Smith, J.L.V. Vicente, J. Wilcox, M. del Mar Zamora Dominguez, Negative emissions – Part 1: Research landscape and synthesis, Environ. Res. Lett. 13 (6) (2018) 063001.
[6] EEA, Analysis of Key Trends and Drivers in Greenhouse Gas Emissions in the EU between 1990 and 2014, (2016).
[7] J. Wilcox, P.C. Psarras, S. Liguori, Assessment of reasonable opportunities for direct air capture, Environ. Res. Lett. 12 (6) (2017) 065001, https://doi.org/10.1088/1748-9326/aa6de5.
[8] J. Wilcox, Carbon Capture, Springer, 2012, https://doi.org/10.1007/978-1-4614-2215-0 https://www.springer.com/gp/book/9781461422143.
[9] M. Lehner, R. Tichler, H. Steinmüller, M. Koppe, Power-to-Gas: Technology and Business Models, Springer International Publishing, New York, 2014.
[10] Audi MediaCenter, https://www.audi-mediacenter.com/de/brennstoffzelle-audi-h-tron-242 (accessed 11.06.18).
[11] CRI, World's Largest CO_2 Methanol Plant, (2018) (accessed 18.06.18), http://carbonrecycling.is/george-olah/.
[12] Sunfire, First Commercial Plant for the Production of Blue Crude Planned in Norway, (2017) (accessed 18.06.18), https://www.sunfire.de/en/company/press/detail/first-commercial-plant-for-the-production-of-blue-crude-planned-in-norway.
[13] B. Decourt, B. Lajoie, R. Debarre, O. Soupa, The Hydrogen-based Energy Conversion FactBook, The SBC Energy Institute, 2014.
[14] R.E. Clarke, S. Giddey, F.T. Ciacchi, S.P.S. Badwal, B. Paul, J. Andrews, Direct coupling of an electrolyser to a solar PV system for generating hydrogen, Int. J. Hydrogen Energy 34 (6) (2009) 2531–2542, https://doi.org/10.1016/j.ijhydene.2009.01.053.
[15] P. Schmidt, W. Zittel, W. Weindorf, T. Raksha, Renewables in Transport 2050 – empowering a sustainable mobility future with zero emission fuels from renewable electricity, Final Report 1086, FVV (2016), https://doi.org/10.1007/978-3-658-13255-2.
[16] L.J. Murphy, K.N. Robertson, R.A. Kemp, H.M. Tuononen, J.A.C. Clyburne, Structurally simple complexes of CO_2, Chem. Commun. 51 (2015) 3942–3956, https://doi.org/10.1039/C4CC08510H.
[17] J. Yu, S.S.C. Chuang, The role of water in CO_2 capture by amine, Ind. Eng. Chem. Res. 56 (21) (2017) 6337–6347, https://doi.org/10.1021/acs.iecr.7b00715.
[18] H.A. Patel, J. Byun, C.T. Yavuz, Carbon dioxide capture adsorbents: chemistry and methods, ChemSusChem 10 (7) (2017) 1303–1317, https://doi.org/10.1002/cssc.201601545.
[19] L. Zhang, X. Wang, M. Fujii, L. Yang, C. Song, CO_2 capture over molecular basket

sorbents: effects of SiO_2 supports and PEG additive, J. Energy Chem. 26 (5) (2017) 1030–1038, https://doi.org/10.1016/j.jechem.2017.09.002.
[20] S. Choi, J.H. Drese, P.M. Eisenberger, C.W. Jones, Application of amine-tethered solid sorbents for direct CO_2 capture from the ambient air, Environ. Sci. Technol. 45 (6) (2011) 2420–2427, https://doi.org/10.1021/es102797w.
[21] Y. Kuwahara, D.-Y. Kang, J.R. Copeland, P. Bollini, C. Sievers, T. Kamegawa, H. Yamashita, C.W. Jones, Enhanced CO_2 adsorption over polymeric amines supported on heteroatom-incorporated SBA-15 silica: Impact of heteroatom type and loading on sorbent structure and adsorption performance, Chem.-Eur. J. 18 (52) (2012) 16649–16664, https://doi.org/10.1002/chem.201203144.
[22] W. Chaikittisilp, H.J. Kim, C.W. Jones, Mesoporous alumina-supported amines as potential steam-stable adsorbents for capturing CO_2 from simulated flue gas and ambient air, Energy Fuels 25 (11) (2011) 5528–5537, https://doi.org/10.1021/ef201224v.
[23] A. Goeppert, S. Meth, G.K.S. Prakash, G.A. Olah, Nanostructured silica as a support for regenerable high-capacity organoamine-based CO_2 sorbents, Energy Environ. Sci. 3 (2010) 1949–1960, https://doi.org/10.1039/C0EE00136H.
[24] X. Wang, X. Ma, V. Schwartz, J.C. Clark, S.H. Overbury, S. Zhao, X. Xu, C. Song, A solid molecular basket sorbent for CO_2 capture from gas streams with low CO_2 concentration under ambient conditions, Phys. Chem. Chem. Phys. 14 (2012) 1485–1492, https://doi.org/10.1039/C1CP23366A.
[25] M.E. Potter, K.M. Cho, J.J. Lee, C.W. Jones, Role of alumina basicity in CO_2 uptake in 3-aminopropylsilyl-grafted alumina adsorbents, ChemSusChem 10 (10) (2017) 2192–2201, https://doi.org/10.1002/cssc.201700115.
[26] A. Wagner, B. Steen, G. Johansson, E. Zanghellini, P. Jacobsson, P. Johansson, Carbon dioxide capture from ambient air using amine-grafted mesoporous adsorbents, Int. J. Spectrosc. 2013 (2013) 1–8, https://doi.org/10.1155/2013/690186.
[27] L. He, M. Fan, B. Dutcher, S. Cui, X. dong Shen, Y. Kong, A.G. Russell, P. McCurdy, Dynamic separation of ultradilute CO_2 with a nanoporous amine-based sorbent, Chem. Eng. J. 189-190 (2012) 13–23, https://doi.org/10.1016/j.cej.2012.02.013.
[28] D.M. Pacheco, J.R. Johnson, W.J. Koros, Aminosilane-functionalized cellulosic polymer for increased carbon dioxide sorption, Ind. Eng. Chem. Res. 51 (1) (2012) 503–514, https://doi.org/10.1021/ie2020685.
[29] C. Gebald, J.A. Wurzbacher, P. Tingaut, T. Zimmermann, A. Steinfeld, Amine-based nanofibrillated cellulose as adsorbent for CO_2 capture from air, Environ. Sci. Technol. 45 (20) (2011) 9101–9108, https://doi.org/10.1021/es202223p.
[30] W.R. Lee, S.Y. Hwang, D.W. Ryu, K.S. Lim, S.S. Han, D. Moon, J. Choi, C.S. Hong, Diamine-functionalized metal-organic framework: exceptionally high CO_2 capacities from ambient air and flue gas, ultrafast CO_2 uptake rate, and adsorption mechanism, Energy Environ. Sci. 7 (2014) 744–751, https://doi.org/10.1039/C3EE42328J.
[31] A. Ursúa, P. Sanchis, Static-dynamic modelling of the electrical behaviour of a commercial advanced alkaline water electrolyser, Int. J. Hydrogen Energy 37 (24) (2012) 18598–18614, https://doi.org/10.1016/j.ijhydene.2012.09.125.
[32] Ø. Ulleberg, Modeling of advanced alkaline electrolyzers: A system simulation approach, Int. J. Hydrogen Energy 28 (1) (2003) 21–33, https://doi.org/10.1016/S0360-3199(02)00033-2.
[33] M. Carmo, D. Fritz, J. Mergel, D. Stolten, A comprehensive review on PEM water electrolysis, Int. J. Hydrogen Energy 38 (12) (2013) 4901–4934, https://doi.org/10.1016/j.ijhydene.2013.01.151.
[34] L. Bertuccioli, A. Chan, D. Hart, F. Lehner, B. Madden, E. Standen, Study on development of water electrolysis in the EU, Final report in fuel cells and hydrogen joint undertaking, (2014).
[35] P. Millet, S. Grigoriev, Chapter 2 – Water electrolysis technologies, in: L. Gandía, G. Arzamendi, P. Diéguez (Eds.), Renewable Hydrogen Technologies, Elsevier, Amsterdam, 2013, pp. 19–41, , https://doi.org/10.1016/B978-0-444-56352-1.00002-7 http://www.sciencedirect.com/science/article/pii/B9780444563521000027.
[36] A.G. Siemens, Kick-off for World's Largest Electrolysis System in Mainz, (2015) (accessed 20.06.18), http://www.siemens.com/press/en/feature/2014/corporate/2014-05-energiepark-mainz.php.
[37] Hydrogenics Corporation, E.ON Inaugurates Energy Storage Facility using Hydrogenics PEM Technology, (2015) (accessed 11.06.18), https://globenewswire.com/news-release/2015/10/15/776393/10152542/en/E-ON-Inaugurates-Energy-Storage-Facility-Using-Hydrogenics-PEM-Technology.html.
[38] M. Hillestad, Modeling the Fischer-Tropsch product distribution and model implementation, Chem. Prod. Process Model. 10 (3) (2015) 147–159, https://doi.org/10.1515/cppm-2014-0031.
[39] P. Kaiser, R.B. Unde, C. Kern, A. Jess, Production of liquid hydrocarbons with CO_2 as carbon source based on reverse water-gas shift and Fischer-Tropsch synthesis, Chemie Ingenieur Technik 85 (4) (2013) 489–499, https://doi.org/10.1002/cite.201200179.
[40] F. Vidal Vázquez, P. Pfeifer, J. Lehtonen, P. Piermartini, P. Simell, V. Alopaeus, Catalyst screening and kinetic modeling for CO production by high pressure and temperature reverse water gas shift for Fischer–Tropsch applications, Ind. Eng. Chem. Res. 56 (45) (2017) 13262–13272, https://doi.org/10.1021/acs.iecr.7b01606.
[41] J. Xu, G.F. Froment, Methane steam reforming, methanation and water-gas shift: I. Intrinsic kinetics, AIChE J. 35 (1) (1989) 88–96, https://doi.org/10.1002/aic.690350109.
[42] A. Kosonen, J. Ahola, C. Breyer, A. Albó, Large scale solar power plant in Nordic conditions, 2014 16th European Conference on Power Electronics and Applications (2014) 1–10, https://doi.org/10.1109/EPE.2014.6911030.
[43] J. Koponen, A. Kosonen, V. Ruuskanen, K. Huoman, M. Niemelä, J. Ahola, Control and energy efficiency of PEM water electrolyzers in renewable energy systems, Int. J. Hydrogen Energy 42 (50) (2017) 29648–29660.
[44] A. Moro, L. Lonza, Electricity carbon intensity in European member states: Impacts on GHG emissions of electric vehicles, Transp. Res. D: Transp. Environ. (2017), https://doi.org/10.1016/j.trd.2017.07.012.
[45] J. Elfving, C. Bajamundi, J. Kauppinen, T. Sainio, Modelling of equilibrium working capacity of PSA, TSA and TVSA processes for CO_2 adsorption under direct air capture conditions, J. CO_2 Util. 22 (2017) 270–277, https://doi.org/10.1016/j.jcou.2017.10.010.
[46] J. Elfving, C. Bajamundi, J. Kauppinen, Characterization and performance of direct air capture sorbent, Energy Proc. 114 (2017) 6087–6101, https://doi.org/10.1016/j.egypro.2017.03.1746 13th International Conference on Greenhouse Gas Control Technologies, GHGT-13, 14–18 November 2016, Lausanne, Switzerland.
[47] Climeworks, Capturing CO_2 from Air, (2018) (accessed 12.06.18), http://www.climeworks.com.
[48] B.H. Davis, Fischer-Tropsch synthesis: overview of reactor development and future potentialities, Top. Catal. 32 (3–4) (2005) 143–168, https://doi.org/10.1007/s11244-005-2886-5.
[49] M. Ostadi, E. Rytter, M. Hillestad, Evaluation of kinetic models for Fischer–Tropsch cobalt catalysts in a plug flow reactor, Chem. Eng. Res. Des. 114 (3) (2016) 236–246, https://doi.org/10.1016/j.cherd.2016.08.026.
[50] J.R. Couper, W.R. Penney, J.R. Fair, S.M. Walas, Chemical Process Equipment: Selection and Design, 2nd ed., Elsevier Inc., 2010, https://www.sciencedirect.com/science/book/9780123969590#book-info.
[51] TWB Group, Global Solar Atlas, (2018) (accessed 18.06.18), http://www.globalsolaratlas.info/.

Publication V

Ruuskanen, V., Koponen, J., Huoman, K., Kosonen. A, Niemelä, M., and Ahola, J.

PEM water electrolyzer model for a power-hardware-in-loop simulator

International Journal of Hydrogen Energy,
vol. 42, no. 16, Apr. 2017.

INTERNATIONAL JOURNAL OF HYDROGEN ENERGY 42 (2017) 10775–10784

Available online at www.sciencedirect.com

ScienceDirect

journal homepage: www.elsevier.com/locate/he

PEM water electrolyzer model for a power-hardware-in-loop simulator

Vesa Ruuskanen *, *Joonas Koponen*, *Kimmo Huoman*, *Antti Kosonen*, *Markku Niemelä*, *Jero Ahola* **

LUT School of Energy Systems, Lappeenranta University of Technology, Lappeenranta, Finland

ARTICLE INFO

Article history:
Received 3 January 2017
Received in revised form
28 February 2017
Accepted 8 March 2017
Available online 25 April 2017

Keywords:
PEM electrolysis modeling
PEM electrolyzer
Power-hardware-in-loop
Power electronics
Renewable hydrogen

ABSTRACT

Power-electronics-based power-hardware-in-loop (PHIL) simulator for water electrolyzer emulation with a nominal current of 405 A is developed to study the electrolyzer as part of a smart grid and to analyze the characteristics of various electrolyzer power supply electronics. A simplified model of a proton exchange membrane (PEM) electrolyzer is implemented into the PHIL simulator to describe the voltage and current characteristics of the electrolyzer stack. The model is verified comparing the current and the estimated hydrogen production of the PHIL simulator with the measured values of the commercial PEM electrolyzer following the measured solar photovoltaic (PV) system output power.

Introduction

In 2050, the main proportion of the electricity produced in the EU area may be used for water electrolysis to produce hydrogen, which is used as a raw material of the synthesis to produce both net CO_2 free chemicals and fuels for transportation and seasonal energy storages [1]. The main idea of the net CO_2 free Power-to-X concept based on renewable energy sources is shown in Fig. 1 [2,3].

Hydrogen produced by water electrolysis and consumed by fuel cells is suggested to be used as an energy storage in the electric grid for example in Ref. [4], although the round-trip efficiency is reported to be inversely proportional to the power density and the capex effectiveness in Ref. [5]. As the distributed production of wind and solar power provides a sustainable and cost-effective solution for electricity generation [6,7], grid-connected water electrolyzers can also contribute to electric grid services, such as inertia and frequency control, by executing controlled power consumption [8–10].

As an example of the DC voltage and current levels in MW-scale electrolyzers, the Power-to-Gas plant by ETOGAS in Werlte, Germany, applies three 2 MW alkaline water electrolyzers, whose nominal input voltage is 250 V and current 9000 A [11]. Owing to the requirement for high DC currents, the rectifiers in conventional industrial water electrolyzers are typically based on thyristors and diodes [12]. The use of passive filters, especially on the MW scale, can be unfavorable because of the high-amplitude and low-frequency harmonics

* *Corresponding author.*
** *Corresponding author.*
E-mail addresses: vesa.ruuskanen@lut.fi (V. Ruuskanen), jero.ahola@lut.fi (J. Ahola).
http://dx.doi.org/10.1016/j.ijhydene.2017.03.046

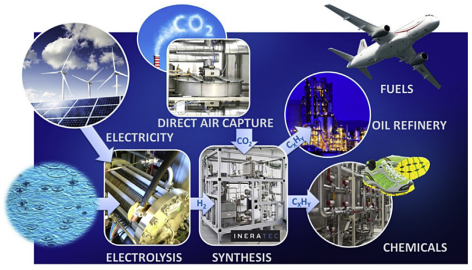

Fig. 1 – Net CO_2 free Power-to-X system is solely based on renewable energy sources.

introduced by the rectification. Application of more modern power electronic converters may be beneficial, but would require modular conversion structures to share the supplied currents to suitable levels for semiconductors using forced commutation, such as an insulated-gate bipolar transistor. Thorough investigation of the effect of electric conditioning on water electrolysis systems is yet to be conducted.

Power-hardware-in-loop (PHIL) simulation enables testing of power devices under actual load conditions. PHIL simulation applications vary from testing of large electrical motors to renewable energy systems including smart grid [13–15]. PHIL simulation of electrolyzer systems provides an economically feasible, safe, and flexible method to examine various power electronic converters supplying the water electrolyzer on an industrial scale. The losses of the converter can be measured under actual load conditions, but the emulation of hydrogen production eliminates the hydrogen safety aspects from the experimental tests, since only electrical energy is transferred through the PHIL simulator; no hydrogen is produced, handled, or stored. PHIL simulation enables emulating of distinct electrolyzer technologies and sizes without costly hardware changes. Further, the output voltage and current waveforms of the converter can be measured to study the effect of the converter selection on the specific energy consumption of the electrolyzer stack, varying as a function of DC current quality.

The output voltage of the water electrolyzer power supply can be set to a constant value or the voltage can be adjusted in real time based on the power reference from the upper-level grid control. The power control can, for example, limit the power to support the grid stability control or maximize the hydrogen production of the renewable power sources. The power supply can be diode, thyristor, or transistor based with their distinct output voltage waveforms. The water electrolysis PHIL simulator adapts the current to the voltage value of the electrolyzer interface and gives information of the electrolysis process according to the electrolyzer model. Among the most relevant information are the electric power consumed and the hydrogen, oxygen, and waste heat produced.

Hydrogen production emulation concepts have previously been proposed on a smaller scale to assess operation with renewable energy sources, for example in Refs. [16–18], but no electrolyzer emulators on the power scale of tens of kilowatts have been reported in the literature so far. Most of the PHIL systems found in the literature are based on DC/DC converters or DC power sources with powers not more than 1 kW [19,20], but the aim is towards higher power levels [21].

In Ref. [22] the 405 A power-hardware-in-loop simulator, further studied in this paper, is introduced, and the dynamics of the simulator is found out to be adequate to emulate electrolytic hydrogen production with any of the main water electrolysis technologies. In this paper, an electrochemical stack model of a proton exchange membrane (PEM) electrolyzer is introduced and implemented into the PHIL simulator. The main advantages of the proposed PHIL simulator over the previous work are: 1. The power of the electrolyzer PHIL simulator is significantly higher than reported in the literature. 2. The dynamics and efficiency of the industrial-scale electrolyzer supply electronics can be studied in actual load conditions. 3. The commercial converters make the proposed PHIL simulator a robust and cost-effective solution for electrolyzer emulation. 4. The PHIL simulator allows emulation of any water electrolyzer type or any other DC load without hardware changes.

This paper is organized as follows. The fundamentals of water electrolysis and the operation principle of PEM water electrolysis is introduced in Section PEM water electrolysis. The PEM water electrolyzer and a PHIL simulator used for experimental tests are presented in Section Experimental test setup. An electrochemical model for a PEM stack is introduced and discussed in Section PEM electrolyzer modeling. Section Experimental verification includes the experimental results of emulating the operation of a PEM electrolyzer with the PHIL simulator. The PHIL simulator is supplied with the measured voltage waveform of a commercial PEM electrolyzer following the measured solar photovoltaic (PV) output power. The simulated current consumption and hydrogen production results are compared with the measured values. Finally, Section Conclusions concludes the paper.

PEM water electrolysis

There are three main water electrolysis technologies available; 1) alkaline, 2) PEM, and 3) solid oxide electrolyte (SOE) water electrolysis. Alkaline water electrolysis is the conventional and the most mature technology of the three and accounts for the majority of installed water electrolysis capacity worldwide [23]. The PEM technology has been gaining interest owing to its compact system design, reportedly superior dynamic operation capability, high hydrogen purity, and high efficiency at higher current densities compared with alkaline electrolysis [24,25]. PEM water electrolyzers have been associated with inferior system durability and a higher system price compared with the conventional alkaline technology [24], but recently, also the PEM technology has reached the MW scale [26,27]. The SOE technology is still in the R&D stage, and it is actually a steam electrolyzer [28].

The principle of water electrolysis is to pass a direct current between two electrodes in order to decompose water into hydrogen and oxygen. According to the Faraday's laws of electrolysis, the production of hydrogen is directly proportional to the electric charge transferred at the electrodes, in other words, the mean value of the current flowing through

the electrolyzer stack. The hydrogen production rate (mol s^{-1}) of a single electrolytic cell can be expressed as

$$f_{H_2} = \eta_F \frac{i_{cell} A_{cell}}{zF}, \quad (1)$$

where z (for hydrogen, z = 2) is the number of moles of electrons transferred in the reaction, F is the Faraday constant (9.6485×10^4 C mol^{-1}), i_{cell} is the current density (A cm^{-2}), A_{cell} is the effective cell area (cm^2), and η_F is the Faraday efficiency, also known as the current efficiency. The energy required for the reaction to take place is the enthalpy of formation of water ΔH. Only the free energy of this reaction, the Gibbs free energy change ΔG, has to be supplied to the electrodes in the form of electrical energy. *The lowest voltage* required for the water decomposition to occur is called the reversible voltage U_{rev}. Without auxiliary heat, the minimum voltage required is higher than the reversible voltage. A designation "thermoneutral voltage" U_{tn} is often used in the literature for this higher voltage level [29,28]. The reversible voltage and the thermoneutral voltage in standard ambient conditions are 1.23 V and 1.48 V, respectively ($\Delta H = 258.84$ kJ mol^{-1}, $\Delta G = 237.21$ kJ mol^{-1}). The electrolytic cell voltage is a sum of the reversible and additional overvoltages in the electrolytic cell

$$U_{cell} = U_{rev} + U_{ohm} + U_{act} + U_{con}, \quad (2)$$

where U_{cell} is the cell voltage, U_{ohm} is the overvoltage caused by ohmic losses in the cell elements, U_{act} is the activation overvoltage caused by electrode kinetics, and U_{con} is the concentration overvoltage caused by mass transport processes [28]. In the literature, it has been stated that the concentration overvoltage would only be significant at current densities significantly higher than in present commercial PEM water electrolyzers, and hence, it has been neglected in the model [30]. The commercial PEM electrolyzers typically operate at current densities of 0.6 A cm^{-2}–2.0 A cm^{-2} and at operating temperatures of 50 °C–80 °C. In PEM water electrolyzers, a thin 50 μm–250 μm proton conducting membrane is applied as a solid polymer electrolyte rather than the liquid electrolyte solutions typically used in alkaline water electrolyzers. The absence of liquid electrolyte then minimizes the need for additional equipment for the circulation of electrolytes and separation of gases. The operating principle of PEM electrolysis is presented in Fig. 2. Deionized water is supplied to the anode side, where the oxygen evolution reaction occurs. H^+ protons from the decomposed water molecules pass through the polymer electrolyte membrane and combine with electrons to form diatomic hydrogen gas at the cathode. The chemical reactions taking place in the PEM electrolysis at the anode and the cathode are as follows

$$H_2O \rightarrow \frac{1}{2}O_2 + 2H^+ + 2e^-, \quad (3)$$

$$2H^+ + 2e^- \rightarrow H_2. \quad (4)$$

For the state-of-the-art PEM electrolyzers, voltage efficiencies, specified for example in Ref. [31], have been reported to be up to 82%, which corresponds to a cell voltage level of 1.8 V. This level of voltage efficiency has also been achieved by the alkaline technology, albeit at lower current densities limited below 0.4 A cm^{-2} [24]. The compact character of

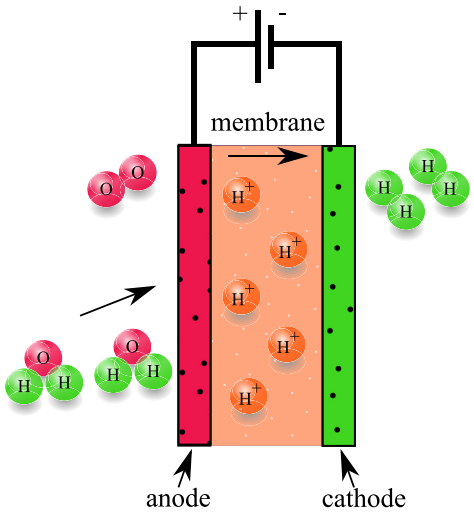

Fig. 2 – Operating principle of a PEM water electrolyzer.

electrolysis modules and the structural properties of the membrane electrode assemblies allow high operating pressures and give PEM electrolyzers the ability to endure great pressure differences between the electrode compartments. This enables the direct production of pressurized hydrogen gas and eliminates the need to handle pressurized oxygen [28]. For example, the commercial PEM electrolyzer, studied in this paper and introduced in the next section, has a designed hydrogen gas outlet pressure of 5000 kPa, while the oxygen outlet pressure is maintained at 200 kPa [32].

Experimental test setup

A power-hardware-in-loop simulator is introduced for water electrolysis emulation. A commercially available PEM water electrolyzer is used for parameter fitting of the PEM stack model and experimental verification of the results.

PEM electrolyzer

A commercially available 4.5 kW PEM electrolyzer shown in Fig. 3 is used for the verification of the electrochemical PEM stack model. Further, the PEM electrolyzer is used to verify the PHIL simulator operation under the operating cycle defined by the solar PV electricity production.

The main parameters of the PEM water electrolyzer are collected in Table 1.

Power-hardware-in-loop simulator

The PHIL simulator is capable of handling continuous current up to 405 A and more than 600 V of voltage, producing a power of 250 kW. The operating principle of the PHIL

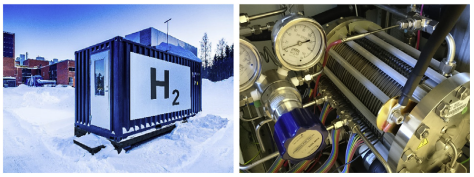

(a) Container (b) PEM stack

Fig. 3 – IRD E1050 differential pressure PEM water electrolyzer built in a 6 m shipping container.

Table 1 – Main parameters of the IRD E1050 PEM water electrolyzer.

Hydrogen production rate	0.97 Nm^3/h
Nominal stack power	4.5 kW
Nominal voltage	64 V
Nominal current	70 A
Number of cells in series	33
Cell cross-sectional area	69 cm^2
Hydrogen pressure	1500 kPa–5000 kPa
Oxygen pressure	150 kPa–250 kPa

simulator with the converter reference signals is illustrated in Fig. 4. The nominal values of the converters are collected into Table 2, and the hardware of the PHIL simulator is shown in Figs. 5 and 6.

The PHIL simulator is modular and can be divided into three operational parts as shown in Fig. 4. The power supply module will be the actual device under test (DuT) supplying DC voltage to the electrolyzer. At the moment, the power supply consists of a grid-connected rectifier with an internal DC link capacitor and a buck converter reducing the voltage level to be suitable for the electrolyzer.

The electrolyzer emulator acts as a variable impedance to control the emulator interface current to match the measured electrolyzer interface voltage based on a predefined current surface. The emulator has a boost converter and an additional LCL filter between the boost converter and the power supply unit.

Table 2 – Nominal values of the Power Boost DC/DC converter and the Power Master inverter both manufactured by Visedo Oy.

	Power Boost	Power Master
Nominal power	250 kW	250 kW
Nominal DC link voltage	750 V	750 V
DC link voltage	0 V–800 V	0 V–800 V
Nominal output DC voltage	617 V	–
Output AC voltage	–	0 V–560 V
Nominal current	405 A_{DC}	300 A_{RMS}

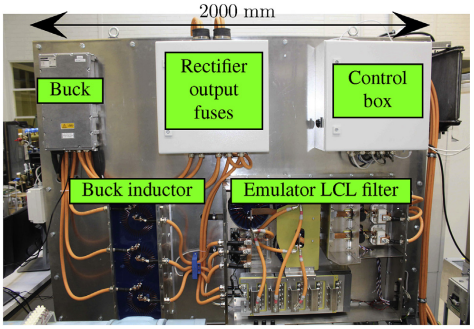

Fig. 5 – Power supply side of the PHIL simulator. Rectified voltage is supplied to the buck DC/DC converter with an external inductor. An LCL filter is located between the buck and boost converters to enable independent current control of the converters. The current and voltage of the electrolyzer emulator are measured between the buck inductor and the emulator LCL filter.

The grid interface returns the electric energy, stored in the DC link capacitor, safely to the grid through the transformer providing the galvanic isolation between the input and the output of the system. An additional grid LCL filter is used to improve the power quality. The grid inverter is controlled with a DC link voltage reference.

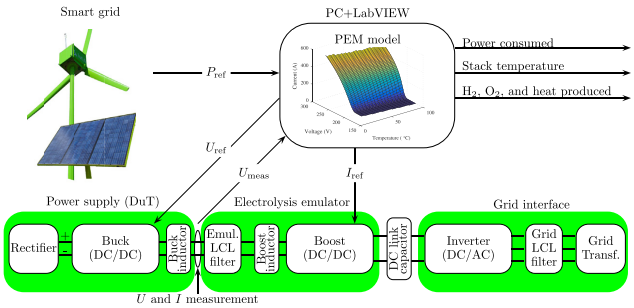

Fig. 4 – Block diagram of the PHIL simulator. Both the buck converter and the boost converter are Power Boost DC/DC converters with external inductors, and the grid inverter is a Power Master inverter.

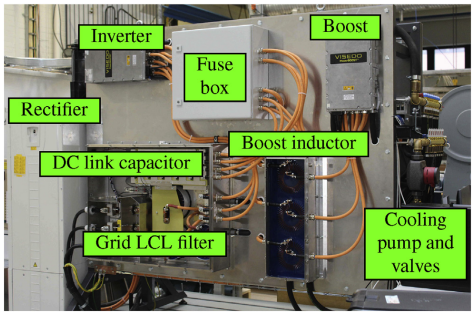

Fig. 6 – Grid interface side of the PHIL simulator. A grid-supplied rectifier is connected to the fuse box and further to the buck DC/DC converter on the power supply side. The boost inductor is connected to the emulator LCL filter on the power supply side. The DC links of the boost converter and the grid inverter are connected to an additional DC link capacitor. The grid inverter is connected to the grid transformer through the grid LCL filter, sharing the casing with the DC link capacitor, to improve the output power quality.

The system is controlled using an NI LabVIEW environment on a PC. A CompactRIO (cRIO) real-time controller is employed for current and voltage measurements of the electrolyzer emulator interface at the 10 kHz sampling frequency. The CANopen protocol is used to communicate with the converters.

The voltage reference for the buck converter is selected based on the electrolyzer power control strategy applied. In this paper, the voltage is controlled to follow the power produced by the solar PV system. The current reference for the boost converter is generated using the predefined electrolyzer current surface (Lookup Table) based on the voltage measurement and the temperature, as described in the next Section, with a 25 ms control period.

PEM electrolyzer modeling

In general, the purpose of electrolyzer stack modeling is to define the stack voltage under certain operating conditions (pressures and temperature) as a function of current. The hydrogen production can be assumed to be linearly proportional to the current as shown in (1), and the stack voltage eventually decides the electrical power consumed by the electrolyzer. Typically, experimental data are required to define the parameters needed to calculate the reversible cell voltage and the cell overvoltages as shown in Refs. [33–35]. However, in the case of PHIL simulation, the stack may not be available for experimental parameter tuning. Therefore, it would be favorable to be able to estimate the electric behavior of the electrolyzer based on the analytical equations and the main parameters of the electrolyzer stack. Further, in the PHIL simulation, the current of the stack has to be defined as a function of operating temperature and the momentary voltage of the stack.

Some PEM electrolyzer models with little or no experimental parameter tuning can be found in the literature. Several PEM stack models are compared with each other in Ref. [24]. A Simulink model for a PEM electrolyzer system including auxiliary devices, such as water pumps and cooling fans, is presented in Ref. [36]. A dynamic model for a PEM stack is introduced and applied to study the effect of temperature and pressure on the performance of the PEM electrolyzer in Ref. [37]. The effect of temperature and pressure on the PEM characteristic curve is examined in Refs. [38,39]. A PEM stack model including a simple thermal model has been experimentally tuned and verified in Ref. [30].

Excluding the effect of significantly slower thermal phenomena, the reported electrochemical time constants for an alkaline electrolyzer, which is shown to have a longer time constant than PEM electrolyzers, vary from 10 ms to 40 ms [40,41] to 10 min [42]. The response time of the commercial alkaline electrolyzer system, fed with solar and wind energy, has been reported to be less than 1 s in Ref. [43]. Typically, the current derivative of the electrolyzer stack is limited by the supply electronics to prevent premature aging of the electrolytic cells as shown in Ref. [44]. However, the PHIL simulator is used to study the electrolyzer as part of the grid inertia control with a response time in the range of tens of seconds. Therefore, a dynamic electrolyzer stack model is not implemented, but a static electrochemical PEM stack model is used.

The PEM electrolyzer stack, used in this study, has a controlled liquid cooling system trying to keep the stack temperature constant by adjusting the flow rate of the coolant. The temperature of the electrolyzer stack was measured to vary not more than 3 °C during the variable load cycle, described in Section 5, as the stack temperature had reached the constant value of 70 °C beforehand. Therefore, the electrolyzer stack is assumed to operate under constant temperature, and the thermal transients are not studied in this paper.

Electrochemical PEM stack model

Based on Dalton's law, the partial pressures of hydrogen and oxygen can be defined by subtracting the partial pressure of water vapor from the total pressures of cathode and anode, which are assumed to be constant, as follows

$$p_{H_2} = p_{cat} - p_{H_2O}, \tag{5}$$

$$p_{O_2} = p_{an} - p_{H_2O}, \tag{6}$$

where p_{cat} is the total pressure at the cathode in (Pa), p_{an} is the total pressure at the anode, and p_{H_2O} is the water vapor saturation pressure defined as a function of electrolyzer temperature T_{el}<283 K by the Antoine equation

$$\log_{10} p_{H_2O} = 5.1962 - \frac{1730.63}{233.426 + T_{el}}. \tag{7}$$

As the partial pressures are known, the open-circuit voltage is defined using the Nernst equation [37].

$$U_{rev} = U^0_{rev} + \frac{RT_{el}}{zF}\ln\left(\frac{p_{H_2}\cdot p^{1/2}_{O_2}}{p_{H_2O}}\right), \quad (8)$$

where U^0_{rev} is the reversible cell voltage, and R is the universal gas constant (8.314 4621 J mol^{-1} K^{-1}). The reversible cell voltage is defined as a function of temperature as shown in Ref. [45].

$$U^0_{rev} = 1.229 - 0.9\times10^{-3}(T_{el} - 298). \quad (9)$$

The activation overpotential is calculated using the Butler–Volmer equation [46].

$$U_{act} = \frac{RT_{el}}{\alpha_{an}F}\operatorname{arcsinh}\left(\frac{i_{cell}}{2i_{o,an}}\right) + \frac{RT_{el}}{\alpha_{cat}F}\operatorname{arcsinh}\left(\frac{i_{cell}}{2i_{o,cat}}\right). \quad (10)$$

The anode charge transfer coefficient α_{an} (0.433 p.u. at 60 °C) is experimentally defined as a function of temperature in Ref. [38]. The cathode charge transfer coefficient α_{cat} is selected to be 0.5, and the anode and cathode exchange current densities $i_{o,an}$ and $i_{o,cat}$ are temperature dependent and experimentally defined as shown for example in Ref. [38].

The ohmic overpotential is mainly caused by the voltage *across the membrane* as the conductivity of electrodes is significantly higher

$$U_{ohm} = \frac{\delta_m i_{cell}}{\sigma_m}, \quad (11)$$

where δ_m is the thickness of the membrane in (cm). The conductivity of the membrane σ_m (S cm^{-1}) is [47].

$$\sigma_m = (0.005139\lambda - 0.00326)\exp\left[1268\left(\frac{1}{303} - \frac{1}{T_{el}}\right)\right], \quad (12)$$

where λ is the *water content* of the membrane, and defined for values near 20 as a function of temperature in Ref. [48].

$$\lambda = ((-2.89556 + 0.016T_{el}) + 1.625)/0.1875. \quad (13)$$

The effect of concentration overpotential in (2) is neglected as the practical current densities in PEM cells are reported to be not high enough to face mass-transport limitations in Ref. [30].

To define the current reference table as a function of temperature and voltage for the PHIL simulator, the stack voltage curve is calculated by (2) as a function of stack current at various temperatures. The PEM stack characteristic curve is verified comparing it with the values measured with a 4.5 kW PEM water electrolyzer described above.

The anode charge transfer coefficient and the anode and cathode exchange current densities are fitted based on the experimentally defined operating points using a nonlinear least squares method by Matlab's curve fitting toolbox. The fitted characteristic curve with measured points at the temperature of 70 °C is shown in Fig. 7. With the hydrogen outlet pressure of 2000 kPa the minimum current allowed is 15 A. The fitted parameters are collected in Table 3.

It can be seen that the shape of the voltage curve deviates from the experimental points even with the fitted parameters. Therefore, a modified version of the activation overpotential Equation (10) is suggested. First, for example in Ref. [30] the cathode overpotential has been stated to be so small that it can be neglected. Secondly, in this case a third-degree polynomial term is added to describe the concentration effects at the anode.

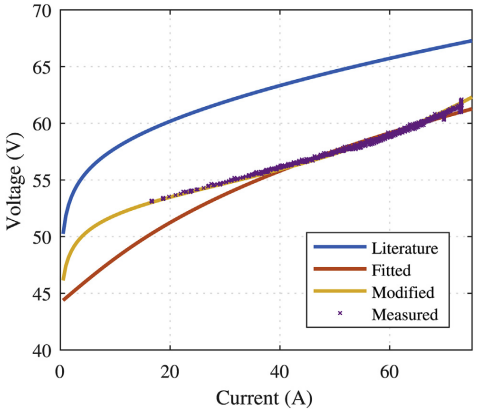

Fig. 7 – Characteristic curves of the PEM stack at the temperature of 70 °C with parameters gathered from the literature, with experimentally fitted parameters, and with the modified activation overpotential equation. The measured operating points during the cycle studied are indicated by purple crosses. (For interpretation of the references to color in this figure legend, the reader is referred to the web version of this article.)

Table 3 – Cell model parameters gathered from the literature [38] and experimentally fitted.

	Literature	Fitted	Modified
α_{an} (p.u.)	0.433	0.186	1.246
$i_{o,an}$ (A cm^{-2})	0.5×10^{-3}	0.111	3.845×10^{-6}
$i_{o,cat}$ (A cm^{-2})	0.391	0.653	–
β_{an} (p.u.)	–	–	4.394

$$U_{act} = \frac{RT_{el}}{\alpha_{an}F}\operatorname{arcsinh}\left(\frac{i_{cell}}{2i_{o,an}}\right) + \frac{RT_{el}}{\alpha_{an}F}\beta_{an}i^3_{cell}, \quad (14)$$

where β_{an} is an experimentally tuned coefficient. With the additional term, the match with the experimental data is significantly better as shown in Fig. 7.

To emulate a 90 kW PEM water electrolyzer with a nominal current of 350 A, the measured PEM stack voltage and current are scaled up. The measured voltage is multiplied by four and the current is multiplied by five to represent four 4.5 kW stacks connected in series and five in parallel. For each temperature under study, the current is solved as a function of voltage. The current surfaces with fitted parameters and a modified model for a 90 kW PEM stack are shown in Fig. 8.

The current surfaces have a slightly different shape as a function of voltage as already seen with constant temperature in Fig. 7 as the fitted model suggests lower voltage compared with measurements at both highest and lowest current values studied. The current surface with modified model is

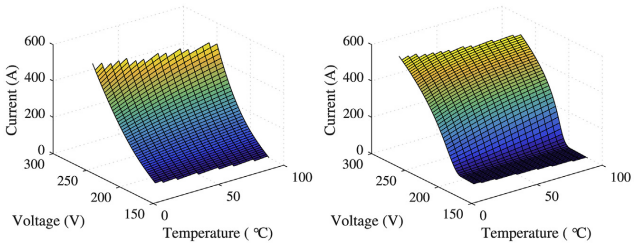

Fig. 8 – PEM stack current as a function of stack voltage and temperature.

implemented in the PHIL simulator and used for the experimental verification in the next section.

Experimental verification

The PEM electrolyzer, shown in Fig. 3, is fed with a current reference defined by the momentary power of the 5 kW_p solar PV of the LUT Solar Power Plant (fixed installation) [49].

The 1000 s reference period with variable cloudiness was selected for analysis. The voltage and current *supplied to the electrolyzer stack*, with a nominal power of 4.5 kW, are measured. The measured solar PV power with the hydrogen production of the PEM electrolyzer is shown in Fig. 9. The hydrogen production is estimated by the measured current value using Faraday's law (1) and verified by the pressure change in the hydrogen tank [44,32].

The hydrogen production of the electrolyzer follows the power reference somewhat behind because of the relatively low-gradient power ramps (20 W s^{-1} increase, 80 W s^{-1} decrease) used to limit the current rise rate to protect the PEM stack from premature aging; thus, a cell voltage degradation rate of 7 μV/h has been obtained for the studied PEM electrolyzer stack design in steady-state operation [44]. The power reference is measured from the solar PV system, but at the moment, the actual power supply of the electrolyzer is from the public grid allowing the momentary electricity consumption of hydrogen production to deviate from the solar PV output power. Moreover, during the highest solar radiation periods, all the power produced by the solar panels cannot be used for the electrolysis because of the 70 A stack current limit.

Voltage and current characteristics

The electrolyzer current and voltage values are measured with 1-s sampling time, and a linear interpolation is used to generate the voltage reference values for the PHIL simulator. The measured electrolyzer voltage and current are scaled up to emulate a 90 kW PEM water electrolyzer with a nominal current of 350 A. The experimental results are shown for the experimentally fitted model and the modified model described above.

The measured voltage waveform of the PHIL simulator is similar for both PEM stack models and shown with the up-scaled PEM stack values in Fig. 10.

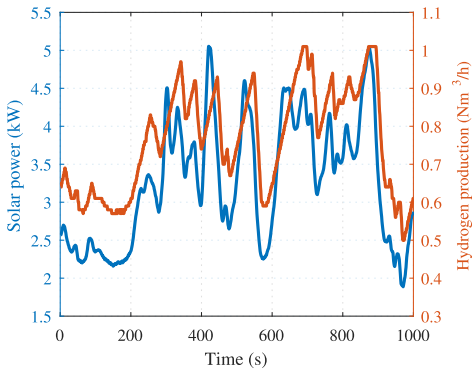

Fig. 9 – Power produced by the solar panels and the hydrogen production of the 4.5 kW PEM electrolyzer.

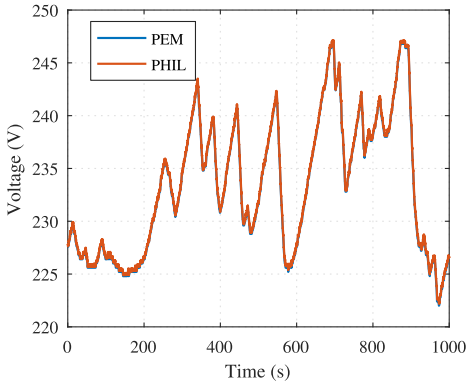

Fig. 10 – Measured voltage of the PEM stack and the PHIL simulator.

The lack of the voltage measurement of the buck converter causes a slight difference between the PEM stack voltage and the simulated voltage. However, the difference in voltages is less than 250 mV over the whole cycle. The difference in voltages produces additional discrepancy while generating the current reference according to the predefined current surface based on the voltage measurement. Even a small difference in voltage may excite a significant discrepancy in currents as the electrolyzer stack voltage changes only slightly as a function of stack current as seen in Fig. 7. The measured PEM stack current, analytically calculated based on the measured voltage with the

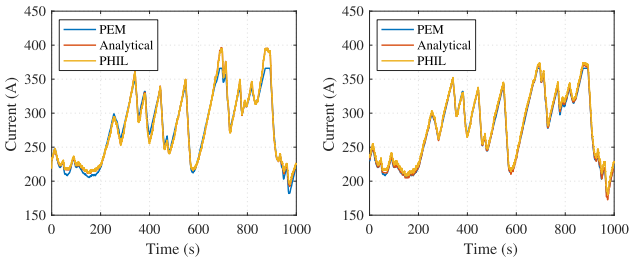

Fig. 11 – Measured current of the PEM stack and the PHIL simulator. The analytical current is estimated using the analytical model based on the measured PEM stack voltage without any hardware.

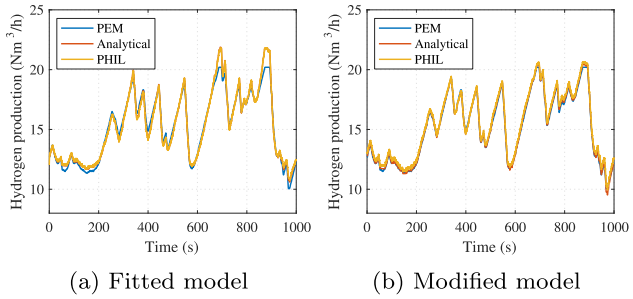

Fig. 12 – Hydrogen production estimated based on the currents.

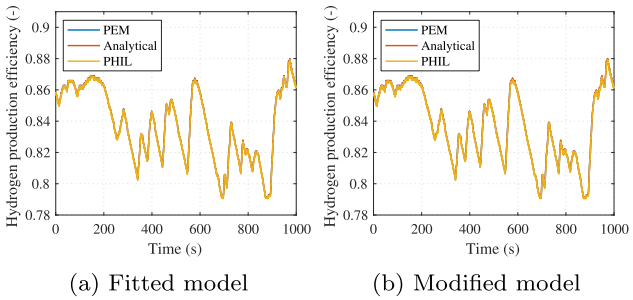

Fig. 13 – Hydrogen production efficiency comparing the higher heating value of the hydrogen produced with the electrical energy consumed by the electrolyzer stack.

model described above, and the measured PHIL simulator current are compared with each other in Fig. 11.

In the case of the fitted model, the error between the model and the experimental results is emphasized at currents close to the nominal operating point as already illustrated in Fig. 7. The difference between the measured and simulated currents with the fitted model is around 30 A at the worst instant. The currents of the modified model visually match the PEM stack currents both analytically and in the PHIL simulation. At the worst instant, the simulated current deviates by 7 A from the measured current and by 3 A from the analytical results. The difference between the analytical results and the measured PHIL simulator current is due to the voltage and current measurement inaccuracies as the same PEM model is used in analytical calculation and PHIL simulation. Thus, the maximum momentary difference between the measured PEM stack current and the PHIL simulator current is less than 2%.

Hydrogen production and efficiency

The hydrogen production rates estimated based on the measured PEM stack current, the analytically calculated current, and the simulated current are compared with each other in Fig. 12.

The difference in currents obviously leads to a respective error in the hydrogen production. However, the difference in the total amount of hydrogen produced during the cycle estimated based on the measured and emulated currents is not more than 1% even in the case of the fitted model and less than 0.5% in the case of the modified model. Finally, the hydrogen production efficiency is defined comparing the higher heating value (3.54 kWh/Nm^3) of the hydrogen produced with the electrical energy consumed by the electrolyzer stack in Fig. 13.

The hydrogen production efficiency has the highest values above 85% at the lowest current densities as the ohmic and activation overpotentials in (2) are minimized. The average stack efficiency over the studied solar PV power defined cycle is approximately 83%. However, it must be taken into account that the energy consumption of the auxiliary devices such as water purification and hydrogen drying, which degrade the total hydrogen production efficiency, is neglected in this study.

Conclusions

A power-hardware-in-loop simulator for water electrolysis emulation was introduced. The parameters for a PEM stack model documented in the literature were defined experimentally. Moreover, the model was modified slightly, and the results were compared with each other. Both models were implemented into a PHIL simulator adapting the electrolyzer emulator current to the predefined current surface based on the measured voltage values. The voltages and currents of the PEM stack and the PHIL simulator were measured, and it was found that the PHIL simulator is able to emulate the electrolyzer behavior well enough to set a realistic load for any electrolyzer stack power supply electronics under test.

Acknowledgement

The LUT authors gratefully acknowledge the public financing of Tekes, the Finnish Funding Agency for Innovation, for the "Neo-Carbon Energy" project under the number 40101/14.

REFERENCES

[1] Renewables in transport 2050. FVV – Research Association for Combustion Engines; 2016. http://www.lbst.de/news/2016_docs/FVV_H1086_Renewables-in-Transport-2050-Kraftstoffstudie_II.pdf.
[2] Neo-Carbon Energy project, [Accessed 20 February 2017]. http://www.neocarbonenergy.fi.
[3] Soletair project, [Accessed 20 February 2017]. http://www.soletair.fi.
[4] Fernandes RA, Philipp HD. Hydrogen cycle peak-shaving on the New York state grid using fuel cells. IEEE Trans Power Appar Syst 1977;96(2):467–77. http://dx.doi.org/10.1109/T-PAS.1977.32356.
[5] Guarnieri M, Alotto P, Moro F. Modeling the performance of hydrogen–oxygen unitized regenerative proton exchange membrane fuel cells for energy storage. J Power Sources 2015;297:23–32. http://dx.doi.org/10.1016/j.jpowsour.2015.07.067. http://www.sciencedirect.com/science/article/pii/S0378775315301142.
[6] Pleßmann G, Erdmann M, Hlusiak M, Breyer C. Global energy storage demand for a 100% renewable electricity supply. Energy Proced 2014;46:22–31.
[7] Fasihi M, Bogdanov D, Breyer C. Techno-economic assessment of Power-to-Liquids (PtL) fuels production and global trading based on hybrid PV-wind power plants. In: Proc. 10th Int. Renewable Energy Storage Conf. (IRES '16), Düsseldorf, Germany; 2016.
[8] Clarke R, Giddey S, Ciacchi F, Badwal S, Paul B, Andrews J. Direct coupling of an electrolyser to a solar PV system for generating hydrogen. Int J Hydrogen Energy 2009;34(6):2531–42.
[9] Valverde L, Bordons C, Rosa F. Integration of fuel cell technologies in renewable-energy-based microgrids optimizing operational costs and durability. IEEE Trans Ind Electron 2016;63(1):167–77.
[10] Garcia-Torres F, Bordons C. Optimal economical schedule of hydrogen-based microgrids with hybrid storage using model predictive control. IEEE Trans Ind Electron 2015;62(8):5195–207.
[11] Erdgas, [Accessed 13 April 2016]. https://www.di-verlag.de/media/content/gwf-GE/gwf_Gas_9_13/gwf-GE_09_2013_fb_Rieke.pdf?xaf26a=7607be2af411325a0ddff8324781 3f87.
[12] Ursúa A, Sanchis P, Marroyo L. Chapter 14-electric conditioning and efficiency of hydrogen production systems and their integration with renewable energies. In: Gandía L, Arzamendi G, Diéguez P, editors. Renewable hydrogen technologies. Amsterdam: Elsevier; 2013. p. 333–60.
[13] Steurer M, Edrington CS, Sloderbeck M, Ren W, Langston J. A megawatt-scale power hardware-in-the-loop simulation setup for motor drives. IEEE Trans Ind Electron 2010;57(4):1254–60.
[14] Huerta F, Tello RL, Prodanovic M. Real-time power hardware-in-the-loop implementation of variable-speed wind turbines. IEEE Trans Ind Electron 2017;64(3):1893–904. http://dx.doi.org/10.1109/TIE.2016.2624259. ISSN: 0278-0046.
[15] Lauss GF, Faruque MO, Schoder K, Dufour C, Viehweider A, Langston J. Characteristics and design of power hardware-in-

the-loop simulations for electrical power systems. IEEE Trans Ind Electron 2016;63(1):406–17.
[16] Zhou T, Francois B, el Hadi Lebbal M, Lecoeuche S. Real-time emulation of a hydrogen-production process for assessment of an active wind-energy conversion system. IEEE Trans Ind Electron 2009;56(3):737–46.
[17] Zhou T. Control and energy management of a hybrid active wind generator including energy storage system with super-capacitors and hydrogen technologies for microgrid application. Ph.D Dissertation. Ecole Centrale de Lille; Jun. 2009. https://tel.archives-ouvertes.fr/tel-00474041.
[18] Zhou M, Liu Y. Theoretical study on direct coupling of a PV array to a PEM electrolyser. In: Proc. Int. Conf. on Materials for Renewable Energy and Environment (ICMREE '13), vol. 1; 2013. p. 52–6.
[19] Koubaa A, Krichen L, Ouali A. Design of fuel cell and electrolyzer emulators for photovoltaic applications. In: Proc. Int. Aegean Conf. on Electric. Machines and Power Electron. and 2011 Electromotion Joint Conf. (ACEMP'11), Istanbul, Turkey; 2011. p. 687–92.
[20] Zhou T, Francois B. Modeling and control design of hydrogen production process for an active hydrogen/wind hybrid power system. Int J Hydrogen Energy 2009;34(1):21–30.
[21] NREL, [Accessed 13 April 2016]. http://www.hydrogen.energy.gov/pdfs/review15/tv031_hovsapian_2015_p.pdf.
[22] Ruuskanen V, Koponen J, Kosonen A, Niemelä M, Ahola J, Tiainen R. Hardware-in-loop emulator for water electrolysers. In: Proc. 42nd Ann. Conf. IEEE Ind. Electron. Society (IECON '16), Firenze, Italy; 2016.
[23] Bertuccioli L, Chan A, Hart D, Lehner F, Madden B, Standen E. Study on development of water electrolysis in the EU, final report in fuel cells and hydrogen joint undertaking. 2014.
[24] Carmo M, Fritz DL, Mergel J, Stolten D. A comprehensive review on PEM water electrolysis. Int J Hydrogen Energy 2013;38(12):4901–34.
[25] Grigoriev S, Porembsky V, Fateev V. Pure hydrogen production by PEM electrolysis for hydrogen energy. Int J Hydrogen Energy 2006;31(2):171–5. http://dx.doi.org/10.1016/j.ijhydene.2005.04.038. http://www.sciencedirect.com/science/article/pii/S036031990500145X.
[26] Hydrogenics, [Accessed 13 April 2016]. http://www.hydrogenics.com/about-the-company/news-updates/2015/10/15/e.on-inaugurates-energy-storage-facility-using-hydrogenics-pem-technology.
[27] Siemens, [Accessed 13 April 2016]. http://www.siemens.com/press/en/feature/2014/corporate/2014-05-energiepark-mainz.php.
[28] Ursúa A, Gandia LM, Sanchis P. Hydrogen production from water electrolysis: current status and future trends. Proc IEEE 2012;100(2):410–26.
[29] Ulleberg Ø. Modeling of advanced alkaline electrolyzers: a system simulation approach. Int J Hydrogen Energy 2003;28(1):21–33.
[30] García-Valverde R, Espinosa N, Urbina A. Simple PEM water electrolyser model and experimental validation. Int J Hydrogen Energy 2012;37(2):1927–38.
[31] Zeng K, Zhang D. Recent progress in alkaline water electrolysis for hydrogen production and applications. Prog Energy Combust Sci 2010;36(3):307–26. http://www.sciencedirect.com/science/article/pii/S0360128509000598.
[32] Koponen J, Kosonen A, Huoman K, Ahola J, Ahonen T, Ruuskanen V. Specific energy consumption of PEM water electrolysers in atmospheric and pressurised conditions. In: Proc. 18th European Conf. on Power Electron. and Applicat. (EPE '16–ECCE Europe), Karlsruhe, Germany; 2016.
[33] van der Merwe J, Uren K, van Schoor G, Bessarabov D. A study of the loss characteristics of a single cell pem electrolyser for pure hydrogen production. In: Proc. IEEE Int. Conf. on Industrial Technology (ICIT '13); 2013. p. 668–72.
[34] da Costa Lopes F, Watanabe EH. Experimental and theoretical development of a PEM electrolyzer model applied to energy storage systems. In: Proc. Brazilian Power Electron. Conf. (COBEP '09); 2009. p. 775–82.
[35] Ursúa A, Martín IS, Sanchis P. Design of a programmable power supply to study the performance of an alkaline electrolyser under different operating conditions. In: 2nd IEEE Int. Energy Conf. and Exhibition (ENERGYCON '12), Florence, Italy; 2012. p. 259–64.
[36] Yigit T, Selamet OF. Mathematical modeling and dynamic simulink simulation of high-pressure PEM electrolyzer system. Int J Hydrogen Energy 2016;41(32):13901–14.
[37] Awasthi A, Scott K, Basu S. Dynamic modeling and simulation of a proton exchange membrane electrolyzer for hydrogen production. Int J Hydrogen Energy 2011;36(22):14779–86.
[38] Biaku C, Dale N, Mann M, Salehfar H, Peters A, Han T. A semiempirical study of the temperature dependence of the anode charge transfer coefficient of a 6 kW PEM electrolyzer. Int J Hydrogen Energy 2008;33(16):4247–54.
[39] Marangio F, Santarelli M, Calí M. Theoretical model and experimental analysis of a high pressure PEM water electrolyser for hydrogen production. Int J Hydrogen Energy 2009;34(3):1143–58.
[40] Chiesa N, Korpås M, Kongstein OE, ødegård A. Dynamic control of electrolyser for voltage quality enhancement. In: Proc. Int. Conf. on Power System Transients (IPST '11), Delft, The Netherlands; 2011. p. 1–7.
[41] Kiaee M, Cruden A, Infield D, Chladek P. Utilisation of alkaline electrolysers to improve power system frequency stability with a high penetration of wind power. IET Renew Power Gen 2014;8(5):529–36.
[42] Mansilla C, Dautremont S, Tehrani BS, Cotin G, Avril S, Burkhalter E. Reducing the hydrogen production cost by operating alkaline electrolysis as a discontinuous process in the French market context. Int J Hydrogen Energy 2011;36(11):6407–13.
[43] Fell H, Chlade P, Wallevik O, Briskeby S. Flexible production of hydrogen from sun and wind: challenges and experiences. In: Proc. 18th World Hydrogen Energy Conf. (WHEC '10), Essen, Germany; 2010. p. 112–8.
[44] Kosonen A, Koponen J, Huoman K, Ahola J, Ruuskanen V, Ahonen T, et al. Optimization strategies of PEM electrolyser as part of solar PV system. In: Proc. 18th European Conf. on Power Electron. and Applicat. (EPE '16–ECCE Europe), Karlsruhe, Germany; 2016.
[45] Harrison K, Hernández-Pacheco E, Mann M, Salehfar H. Semiempirical model for determining PEM electrolyzer stack characteristics. J Fuel Cell Sci Technol 2005;3(2):220–3.
[46] Larminie J, Dicks A. Fuel cell systems explained. England: John Wiley & Sons Ltd.; 2003.
[47] Springer TE, Zawodzinski TA, Gottesfeld S. Polymer electrolyte fuel cell model. J Electrochem Soc 1991;138(8):2334–42. http://dx.doi.org/10.1149/1.2085971. arXiv:http://jes.ecsdl.org/content/138/8/2334.full.pdf+html, http://jes.ecsdl.org/content/138/8/2334.abstract.
[48] Li X, Qu S, Yu H, Hou M, Shao Z, Yi B. Membrane water-flow rate in electrolyzer cells with a solid polymer electrolyte (SPE). J Power Sources 2009;190(2):534–7.
[49] LUT Green Campus, [Accessed 16 June 2016]. http://www.lut.fi/solar.

ACTA UNIVERSITATIS LAPPEENRANTAENSIS

860. SOKOLOV, ALEXANDER. Pulsed corona discharge for wastewater treatment and modification of organic materials. 2019. Diss.

861. DOSHI, BHAIRAVI. Towards a sustainable valorisation of spilled oil by establishing a green chemistry between a surface active moiety of chitosan and oils. 2019. Diss.

862. KHADIJEH, NEKOUEIAN. Modification of carbon-based electrodes using metal nanostructures: Application to voltammetric determination of some pharmaceutical and biological compounds. 2019. Diss.

863. HANSKI, JYRI. Supporting strategic asset management in complex and uncertain decision contexts. 2019. Diss.

864. OTRA-AHO, VILLE. A project management office as a project organization's strategizing tool. 2019. Diss.

865. HILTUNEN, SALLA. Hydrothermal stability of microfibrillated cellulose. 2019. Diss.

866. GURUNG, KHUM. Membrane bioreactor for the removal of emerging contaminants from municipal wastewater and its viability of integrating advanced oxidation processes. 2019. Diss.

867. AWAN, USAMA. Inter-firm relationship leading towards social sustainability in export manufacturing firms. 2019. Diss.

868. SAVCHENKO, DMITRII. Testing microservice applications. 2019. Diss.

869. KARHU, MIIKKA. On weldability of thick section austenitic stainless steel using laser processes. 2019. Diss.

870. KUPARINEN, KATJA. Transforming the chemical pulp industry – From an emitter to a source of negative CO2 emissions. 2019. Diss.

871. HUJALA, ELINA. Quantification of large steam bubble oscillations and chugging using image analysis. 2019. Diss.

872. ZHIDCHENKO, VICTOR. Methods for lifecycle support of hydraulically actuated mobile working machines using IoT and digital twin concepts. 2019. Diss.

873. EGOROV, DMITRY. Ferrite permanent magnet hysteresis loss in rotating electrical machinery. 2019. Diss.

874. PALMER, CAROLIN. Psychological aspects of entrepreneurship – How personality and cognitive abilities influence leadership. 2019. Diss.

875. TALÁSEK, TOMÁS. The linguistic approximation of fuzzy models outputs. 2019. Diss.

876. LAHDENPERÄ, ESKO. Mass transfer modeling in slow-release dissolution and in reactive extraction using experimental verification. 2019. Diss.

877. GRÜNENWALD, STEFAN. High power fiber laser welding of thick section materials - Process performance and weld properties. 2019. Diss.

878. NARAYANAN, ARUN. Renewable-energy-based single and community microgrids integrated with electricity markets. 2019. Diss.

879. JAATINEN, PEKKO. Design and control of a permanent magnet bearingless machine. 2019. Diss.

880. HILTUNEN, JANI. Improving the DC-DC power conversion efficiency in a solid oxide fuel cell system. 2019. Diss.

881. RAHIKAINEN, JARKKO. On the dynamic simulation of coupled multibody and hydraulic systems for real-time applications. 2019. Diss.

882. ALAPERÄ, ILARI. Grid support by battery energy storage system secondary applications. 2019. Diss.

883. TYKKYLÄINEN, SAILA. Growth for the common good? Social enterprises' growth process. 2019. Diss.

884. TUOMISALO, TEEMU. Learning and entrepreneurial opportunity development within a Finnish telecommunication International Venture. 2019. Diss.

885. OYEDEJI, SHOLA. Software sustainability by design. 2019. Diss.

886. HUTTUNEN, MANU. Optimizing the specific energy consumption of vacuum filtration. 2019. Diss.

887. LIIKANEN, MIIA. Identifying the influence of an operational environment on environmental impacts of waste management. 2019. Diss.

888. RANTALA, TERO. Operational level performance measurement in university-industry collaboration. 2019. Diss.

889. LAUKKANEN, MINTTU. Sustainable business models for advancing system-level sustainability. 2019. Diss.

890. LOHRMANN, CHRISTOPH. Heuristic similarity- and distance-based supervised feature selection methods. 2019. Diss.

891. ABDULLAH, UMMI. Novel methods for assessing and improving usability of a remote-operated off-road vehicle interface. 2019. Diss.

892. PÖLLÄNEN, ILKKA. The efficiency and damage control of a recovery boiler. 2019. Diss.

893. HEKMATMANESH, AMIN. Investigation of EEG signal processing for rehabilitation robot control. 2019. Diss.

894. HARMOKIVI-SALORANTA, PAULA. Käyttäjät liikuntapalvelujen kehittäjinä - Käyttäjälähtöisessä palveluinnovaatioprosessissa käyttäjien tuottama tieto tutkimuksen kohteena. 2020. Diss.

895. BERGMAN, JUKKA-PEKKA. Managerial cognitive structures, strategy frames, collective strategy frame and their implications for the firms. 2020. Diss.

896. POLUEKTOV, ANTON. Application of software-defined radio for power-line-communication-based monitoring. 2020. Diss.

897. JÄRVISALO, HEIKKI. Applicability of GaN high electron mobility transistors in a high-speed drive system. 2020. Diss.

ISBN 978-952-335-490-6
ISBN 978-952-335-491-3 (PDF)
ISSN-L 1456-4491
ISSN 1456-4491
Lappeenranta 2020